Dissertation
submitted to the
Combined Faculties for the Natural Sciences and for Mathematics
of the Ruperto-Carola University of Heidelberg, Germany

for the degree of
Doctor of Natural Sciences

presented by
Dipl.-Phys. **Guido Saathoff**
born in Leer

Oral examination: 20th November, 2002

Experimental Test of Relativistic Time Dilation by Laser Spectroscopy of Fast Ions

Referees:
Prof. Dr. Dirk Schwalm
Prof. Dr. H.-Jürgen Kluge

Kurzfassung

Experimenteller Test der relativistischen Zeitdilatation durch Laserspektroskopie an schnellen Ionen

Die vorliegende Arbeit behandelt eine moderne Version des Ives-Stilwell Experiments, das über den transversalen Doppler-Effekt die relativistische Zeitdilatation mißt. Eine Abweichung von der von der Speziellen Relativitätstheorie gegebenen Vorhersage würde eine Verletzung des Relativitätsprinzips bedeuten und damit ein physikalisch ausgezeichnetes Bezugssystem festlegen. Um die Genauigkeit bisheriger Experimente auf diesem Gebiet zu erhöhen, wurde die Systematik zweier Doppler-freier Techniken kollinearer Laserspektroskopie an einem schnellen ($\beta = 0.064$) Ionenstrahl an einem Speicherring untersucht. Die erste Methode, Λ-Spektroskopie an einem geschlossenen Λ-artigen Dreiniveau-System, wurde in einem früheren Experiment durch eine starke, unerklärte Verbreiterung eingeschränkt. Als Ursache dieser Verbreiterung konnten in dieser Arbeit Geschwindigkeitsänderungen, die die Ionen bei einigen bis vielen Umläufen im Speicherring erfahren, identifiziert werden. Darüberhinaus konnte eine Methode entwickelt werden, mit der dieser Verbreiterungsmechanismus unterdrückt werden kann. Die zweite untersuchte Methode ist Sättigungsspektroskopie an einem geschlossenen Zweiniveau-System, die sich als insensitiv auf geschwindigkeitsändernde Effekte erwies. Zusammen mit der Reduzierung systematischer Fehler führte die Anwendung dieser Methode zu einer neuen, im Vergleich zur bisher genauesten Messung um einen Faktor 4 verbesserten oberen Schranke für Abweichungen von der speziell-relativistischen Zeitdilatation.

Abstract

Experimental Test of Relativistic Time Dilation by Laser Spectroscopy of Fast Ions

The present thesis deals with a modern version of the classical Ives-Stilwell experiment, which measures relativistic time dilation via the transverse Doppler effect. A deviation from the prediction given by Special Relativity would disprove the Relativity Principle and, therefore, single out a physically preferred reference frame. In order to enhance the accuracy of previous experiments in this sector, the systematics of two Doppler-free techniques of collinear laser spectroscopy on a fast ($\beta = 0.064$) ion beam in a storage ring have been investigated. The first technique, Λ-spectroscopy on a closed Λ-type three-level system, suffered from a strong, hitherto unaccounted line broadening in a previous test experiment. In this work this line broadening has been shown to be caused by processes changing the velocity of the ions during several to many roundtrips in the storage ring. Additionally, a method has been developed to supress this broadening. The second technique investigated is saturation spectroscopy, which turned out to be insensitive to velocity-changing processes. Together with the reduction of systematic errors the application of saturation spectroscopy has lead to a new upper limit for deviations from special relativistic time dilation, that improves the hitherto best value by a factor of 4.

Contents

Chapter 1

Introduction

In 1962 the physicist Thomas Samuel Kuhn published his seminal work "*The Structure of Scientific Revolutions*" [Kuhn, 1962], in which he stated that science does not evolve gradually toward truth, but instead undergoes periodic revolutions which he calls *paradigm shifts*. The history of science consists of phases of "normal science" that are characterized by paradigms, which define a well-accepted framework of notions and methods. The rise of anomalies that do not fit into the paradigm finally lead to a fundamental change of this framework that underlies science. A paradigm shift constitutes a new fundamental framework, a new paradigm.

One of the most famous examples for such a paradigm shift is without doubt the discovery of the Theory of Special Relativity published by Albert Einstein in 1905 [Einstein, 1905]. The old paradigm of the Newtonian absoluteness of space and time had to be abolished because of several anomalies such as the null-result of the Michelson-Morley experiment. The new theory of space and time entails several non-intuitive kinematical phenomena such as the relativity of simultaneity, length contraction and time dilation. A dynamical consequence of Special Relativity is the mass-energy equivalence. The importance of Special Relativity has generated considerable research in the direction of experimentally confirming Einstein's results and conclusions. However, the null-results of the ether-drift experiments such as the Michelson-Morley experiment and the Trouton-Noble experiment were also consistent with Maxwell-Lorentz electrical theory of matter and until 1938 the only additional support for Special Relativity was the experimental confirmation of the energy-mass equivalence. Ives and Stilwell were the first to observe a direct manifestation of time dilation in 1938. Together with the null-result of the Kennedy-Thorndike experiment first performed in 1932, also length contraction could be confirmed.

Today the propositions of Special Relativity are widely accepted and constitute a paradigm, that is deeply enrooted in all fields of physics. The extended lifetimes

of relativistic cosmic-ray muons are a consequence of Special Relativity. The concept of spin in Quantum Mechanics is deeply connected to Special Relativity. Even in everyday issues relativistic effects play an important role: time dilation and relativistic clock synchronization are routinely accounted for in the US Air Force's NAVSTAR global positioning system [Will, 1986].

Nevertheless, there is much interest in performing more accurate experiments testing local Lorentz invariance in order to base the Lorentz transformation on experimental results rather than on theoretical postulates. Especially through the discovery of the cosmic background radiation [Penzias and Wilson, 1965] one reference frame is singled out cosmologically, namely that in which this radiation appears isotropic. This has renewed the question, whether a preferred reference system - an aether - exists establishing a standard of absolute motion.

In the original Ives-Stilwell experiment time dilation has been measured by observing the Doppler-Shift of light emitted by hydrogen canal rays in forward and backward direction relative to their motion [Ives and Stilwell, 1938]. The wavelength has been analyzed using a spectrometer. In order to further increase the accuracy of this kind of experiment two major ingredients are necessary. First, the accuracy of the wavelength measurement has to be improved and, second, a faster particle beam with improved quality is desirable in order to enhance the sensitivity to time dilation.

The first requirement can be fulfilled by using the meanwhile well-established techniques of high-resolution laser spectroscopy. Because of the extremely narrow bandwidth, single-mode lasers allow for considerably higher spectral resolutions than conventional spectrometers. Furthermore, the high intensities of such lasers have opened up the possibility to develop various techniques of nonlinear specroscopy [Demtröder, 1998], with which it is possible to overcome the limitation set by Doppler broadening due to the thermal velocity distribution of the particle ensemble under study.

The second requirement is achieved by the development of heavy ion storage rings such as the Test Storage Ring (TSR) at Heidelberg, the Experimental Storage Ring (ESR) at Darmstadt, Cryring at Stockholm and ASTRID at Aarhus. These machines allow the storage of fast atomic as well as molecular ion beams with typical storage times of a few seconds to several hours. Originally foreseen for particle physics experiments storage rings showed to be a powerful tool for atomic and molecular physics experiments as well. Accurate measurements concerning electron-ion recombination processes such as dielectronic recombination, laser-induced recombination and, for molecules, dissociative recombination have become feasible. Furthermore, lifetimes of metastable states of a variety of ions have been measured with unprecedented precision [Träbert, 2000] [Rostohar et al., 2001]. Another field of research concerns the test of QED by the

measurement of the $1s$ hyperfine structure transition of highly charged hydrogen-like ions [Klaft et al., 1994] [Seelig et al., 1998].

A major requirement for all these experiments is a high ion beam quality. Especially, high velocity-stability as well as low divergence and momentum spread are indispensable. These required features are achieved by the technique of electron cooling [Beutelspacher, 2000].

In conclusion, the combination of high resolution laser spectroscopy with storage ring techniques allows for a considerable improvement of the historic Ives-Stilwell experiment testing relativistic time dilation. Already soon after start of operation of TSR at the Max-Planck-Institute for Nuclear Physics in Heidelberg precision laser spectroscopy experiments on a fast ($v = 0.064c$) $^7Li^+$ ion beam have begun [Klein, 1991]. This has lead to the hitherto best upper limit for deviations from relativistic time dilation [Grieser et al., 1994b]. The present work continues this experiments and provides a significantly improved understanding and control of the systematics of laser spectroscopy in storage rings. This has now lead to a further improvement of the measurement of time dilation by a factor of 4.

The second chapter introduces the foundations of the TSR experiment. Here, the principle of the experiment is presented with special emphasis to the interpretation in terms of a test theory for Special Relativity. Furthermore, the present status of the test of relativistic time dilation is reviewed.

The third chapter deals with the experimental setup describing first the Heidelberg heavy ion storage ring TSR with special respect to issues like ion beam cooling and ion beam diagnosis, that are important for our experiment. Furthermore, the laser system as well as the alignment of the laser beams with respect to the ion beam are discussed.

Chapter 4 is dedicated to the main systematic errors present in the experiment.

Chapter 5 presents the results of several beamtimes performed during the past three years concerning the systematics of high precision laser spectroscopy in a storage ring. Two approaches of spectroscopy, namely Λ-type optical-optical double resonance as well as saturation spectroscopy have been investigated. The latter has been succesfully applied to perform an improved test of time dilation, which is also presented.

In the last chapter, finally, the main results of the work are concluded and an outlook is given on future steps concerning a further improvement of the upper limit for deviations from time dilation.

Chapter 2

Foundations of the TSR-experiment

2.1 Special Relativity

Newton based the development of mechanics on the notions of absolute space and absolute time. Physical laws are usually stated relative to reference frames provided with coordinates for space and time. The connection between two reference frames moving with uniform velocity with respect to each other is accomplished by the Galilean transformation. The class of all reference frames connected by the Galilean transformation are the inertial frames, in which Newton's laws do apply. However, there is no unique way of locating Newton's absolute space within the infinite class of inertial frames. Only with the rise of Maxwell's electrodynamics it appeared as though the ether could be identified with Newton's absolute space. For the Maxwell equations predicted the propagation of electromagnetic disturbances with a universal velocity c, which turned out to coincide precisely with the vacuum speed of light. The conjectured medium for these electromagnetic waves was considered to be the ether. Since the Maxwell equations are not Galileo-invariant, an ether was needed, to which the validity of the equations was linked. Otherwise Newtonian mechanics and Maxwell's electrodynamics appeared incompatible. This result of Maxwell's theory brought experimental physicists to perform experiments, which searched for direct evidence for the existence of the ether. However, these ether-drift experiments, of which the Michelson-Moreley experiment and the Trouton-Noble experiment are the most famous examples, surprisingly yielded null-results. The conjectured explanation, that the earth completely dragged the ether along with it, was ruled out by observations concerning abberation of starlight. Another attempt to explain the null-results of the experiments was Lorentz's ether theory. It postulated that bodies moving through the ether with velocity v suffer a contraction in the direction of motion by the factor $\gamma = (1 - v^2/c^2)^{-1/2}$. Furthermore, moving clocks were supposed

to go slow by the same factor. These effects can be regarded as an interpretation of the Lorentz transformation, which was found to leave the Maxwell equations unchanged. However, the Lorentz transformation was regarded as a mere mathematical artifice.

In 1905 Albert Einstein came up with an operational approach to the Lorentz transformation. He was able to infer it from two postulates, namely the *special relativity principle* and the *principle of the constancy of the speed of light*. The relativity principle is a generalization of Galilei's relativity principle from mechanics to all physical laws. This postulate means the abolition of absolute space. The physics based on these two postulates is called Special Relativity. It provides a new physical theory of space and time. It can be shown [Rindler, 1977] that the relativity principle is consistent only with the Galilean transformation and the Lorentz transformation. The second postulate, which is confirmed experimentally, rules out the Galilean transformation. However, this postulate can be replaced by any other postulate, which is peculiar to Special Relativity. The Maxwell equations had already shown to be Lorentz-invariant and are therefore consistent with Special Relativity. In contrast, Newton's mechanics was Galileo-invariant but not Lorentz-invariant: it is inconsistent with Special Relativity.

The Lorentz transformation between a reference system S with coordinates (t, x, y, z) and another reference system S' with coordinates (t', x', y', z'), which is moving with a uniform velocity v along x relative to S reads

$$x' = \gamma(x - vt) \tag{2.1}$$
$$y' = y \tag{2.2}$$
$$z' = z \tag{2.3}$$
$$t' = \gamma(t - \frac{vx}{c^2}), \tag{2.4}$$

with $\gamma = 1/\sqrt{1 - v^2/c^2}$. One important consequence of this transformation is time dilation:

> *A clock moving uniformly with velocity v through S goes slow by a factor γ relative to the stationary clocks in S.*

The experiment described in this thesis tests whether time dilation is given by the relation stated by Special Relativity. This is done by measuring the Doppler-shifted transition frequency of a moving ion with help of laser spectroscopy. The Doppler-shift formula derived from the Lorentz transformation

$$\nu_0 = \gamma(1 - \beta \cos\vartheta)\nu \tag{2.5}$$

connects the rest frame frequency ν_0 with the Doppler-shifted laboratory frequency ν. $\beta = v/c$ is the ion velocity and ϑ the angle between the ion motion and

the laser direction, both being measured in the laboratory system S. In contrast to the classical Doppler formula, equation 2.5 contains the time dilation factor γ.

2.2 Test Theories

The theory of Special Relativity is obtained deductively from Einstein's postulates concerning the relativity of motion as well as the constancy of the velocity of light. For an experimental test of the theory these postulates have to be replaced by facts drawn from observations. Special Relativity describes the relationship between inertial reference frames. It is given by the Lorentz transformation, which follows from the postulates. In order to compare the results of different test experiments quantitatively, test theories are developed, which assume a more general transformation between the reference frames. Such theories contain free parameters which reduce to certain values for the case of Special Relativity (SR). Possible deviations from SR would occur, if a preferred reference frame Σ existed in the sense, that it caused physical effects dependent of the velocity relative to this "ether" frame. This would constitute an experimental falsification of the Relativity Principle. The discovery of the cosmic background radiation [Penzias and Wilson, 1965] shows, that cosmologically, a preferred reference frame exists, namely the system in which this radiation appears isotropic.

In a first test theory by Robertson [Robertson, 1949], which is purely kinematical, it was found that three irreducible parameters remain in the generalised transformation between Σ and a reference frame S moving with velocity $\vec{w}$ in Σ, which can be tested by three corresponding experiments. The first experiment is the Michelson-Morley experiment [Michelson and Morley, 1887], the null-result of which is interpreted by Robertson as:

> "The total time required for light to traverse, in free space, a distance l and to return is independent of its *direction*".

The second experiment complementarily tests the

> "independence of the total time required for light to traverse a closed path in S of the *velocity* $\vec{w} \cdot c$ of S relative to Σ".

This test has first been performed by [Kennedy and Thorndike, 1932].

The remaining parameter is tested by the Ives-Stilwell experiment [Ives and Stilwell, 1938]. It measures the rate of a moving clock by observing the transverse Doppler shift. From this experiment it can be concluded, that, within the experimental uncertainty,

> "the frequency of a moving atomic source is altered by the factor $(1-v^2/c^2)^{1/2}$ when observed in the laboratory system, where v is the velocity of the source with respect to the observer".

The TSR-experiment carried out in the course of the present work is a modern version of the Ives-Stilwell experiment.

As we describe the results of our experiment within the modern version of this kinematical test theory developed by Mansouri and Sexl [Mansouri and Sexl, 1977], this theory is briefly introduced in the following.

It starts with some assumptions concerning the propagation of light. First, the velocity of light is considered to be independent of the motion of the light source. Second, a preferred reference system Σ with coordinates (T, X, Y, Z) is supposed to exist and the velocity of light c in Σ is assumed to be isotropic[1]. The transformation between Σ and a reference system S with coordinates (t, x, y, z) moving with a constant velocity $\vec{w} \cdot c$ with respect to Σ is assumed to be linear:

$$\begin{aligned} t &= aT + \epsilon x + \epsilon_2 y + \epsilon_3 z \\ x &= b_1 T + bX + b_2 Y + b_3 Z \\ y &= d_1 T + d_2 X + dY + d_3 Z \\ z &= e_1 T + e_2 X + e_3 Y + eZ. \end{aligned} \tag{2.6}$$

Due to kinematical restrictions (the x and X axes slide along each other, the (x, z) and (X, Z) planes coincide at all times and the origin of S moves along X) as well as due to the restrictions imposed by the assumptions mentioned above the number of parameters is reduced to 6 and the transformation reads:

$$\begin{aligned} t &= a(w)T + \epsilon x + \epsilon_2 y + \epsilon_3 z \\ x &= b(w)(X - wT) \\ y &= d(w)Y \\ z &= d(w)Z. \end{aligned} \tag{2.7}$$

The parameters ϵ, ϵ_2 and ϵ_3 are defined by the synchronization procedure and can not be tested by experiment. For Einstein synchronization these parameters read:

$$\epsilon_{\mathrm{E}} = -\frac{aw/c}{b(1-w^2)}, \qquad \epsilon_{2\mathrm{E}} = \epsilon_{3\mathrm{E}} = 0. \tag{2.8}$$

The velocity-dependent parameters $a(w), b(w)$ and $d(w)$, which describe time dilation and length contraction parallel and perpendicular to w, respectively, have to be determined either by theory or by experiment.

[1]Note: No assumption is made concerning the isotropy of light in any other reference frame.

As we restrict ourselves to the case of Einstein synchronization, which uses the back-and-forth movement of a light signal and is, therefore, insensitive to the one-way speed of light, $a(w), b(w)$ and $d(w)$ can only depend on w^2. In the low-velocity limit it is useful to expand the three parameters in powers of w [Will, 1992]:

$$\begin{aligned} a\,(w) &= 1 + \left(\alpha - \frac{1}{2}\right) w^2 + \left(\alpha_2 - \frac{1}{8}\right) w^4 + \ldots \\ b\,(w) &= 1 + \left(\beta_1 + \frac{1}{2}\right) w^2 + \left(\beta_2 + \frac{3}{8}\right) w^4 + \ldots \\ d\,(w) &= 1 + \delta w^2 + \delta_2 w^4 + \ldots . \end{aligned} \tag{2.9}$$

The parameters α, β_1, δ and $\alpha_2, \beta_2, \delta_2$ are defined such, that they vanish for Special Relativity. In this case we find:

$$\frac{1}{a\,(w)} = b\,(w) = \frac{1}{\sqrt{1-w^2}}, \qquad d\,(w) = 1. \tag{2.10}$$

The velocity of light is in general dependent both on the direction and the absolute value of $\vec{v}$. After [Mansouri and Sexl, 1977] the following relation up to second order in w can be deduced from the generalized Lorentz transformation:

$$\frac{c}{c_\theta} = 1 + (\beta_1 + \delta) w^2 \sin^2\theta + (\alpha - \beta_1) w^2, \tag{2.11}$$

where θ denotes the angle of the light ray with respect to $\vec{w}$. The term proportional to the parameter combination $(\beta + \delta)$ is tested by the Michelson-Morley experiment, while the Kennedy-Thorndike experiment measures $(\alpha - \beta)$. α is tested by the Ives-Stilwell experiment independently.

2.3 Principle of the experiment

In the Ives-Stilwell-type experiment the time dilation factor is measured via the relativistic Doppler shift of optical transitions in moving atoms or ions:

$$\nu_0 = \gamma(1 - \beta\cos\vartheta)\nu, \tag{2.12}$$

where ν_0 and ν denote the transition frequencies in the ions' rest frame and the laboratory frame, respectively. The ions are used as moving clocks and their frequency is measured in the laboratory frame. The comparison of this frequency ν with respect to the rest frame frequency ν_0 tests the validity of the relativistic Doppler formula.

Two different approaches have been realized to test the relativistic time dilation factor. First, the Doppler-shifted frequencies are measured perpendicularly with respect to the motion of the atoms. In this case the kinematic factor $(1-\beta\cos\vartheta)$ in equation 2.12 equals 1 and the clean relativistic part of the Doppler effect stemming solely from time dilation remains. This approach has been realized in Mößbauer rotor experiments, where the frequency shift between a gamma ray source and a resonant absorber attached to opposite tips of a high speed rotor is searched for [Champeney et al., 1963].

The second approach uses optical techniques and goes back to the original Ives-Stilwell experiment [Ives and Stilwell, 1938]. In these experiments the frequency is measured collinearly to the motion of the ions. Hence, the ion velocity β contributes already linearly and has to be known very accurately in order to test γ. As it is difficult to determine the velocity of ions in a beam, in these Doppler-shift experiments the measurement of β is replaced by the measurement of a second Doppler-shifted frequency, which accurately "marks" the ion velocity. That way the original Ives-Stilwell experiment [Ives and Stilwell, 1938] measured the Doppler-shifted Hβ line (486.1 nm) of hydrogen canal rays with and against the motion of the particles. From Special Relativity a shift of the center of gravity of the observed lines is expected, which is solely caused by the relativistic part of the Doppler effect (proportional to β^2). The ion velocity is determined by the Doppler displacement caused by the linear Doppler effect.

In order to improve previous tests of the time dilation factor, frequencies have to be determined with an accuracy of below 1 MHz. This is far below the Doppler-broadening of a few GHz caused by velocity distributions, that are achievable for ion beams in storage rings. For this reason, Doppler-free[2] spectroscopic techniques have to be applied. In this work two different approaches are investigated, saturation spectroscopy on a closed two-level system and Λ-type spectroscopy on a three-level system.

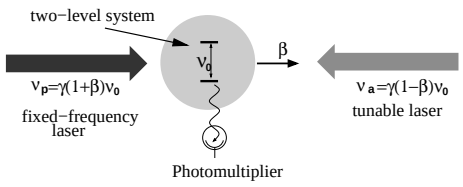

The sketch illustrates the principle of the setup for saturation spectroscopy. The ions moving with a velocity $v = \beta \cdot c$ are overlapped with the two lasers parallel and antiparallel to the direction of propagation. In our experiment we use one fixed-frequency laser and a tunable one. Due to the Doppler effect, resonance with the indicated two-level transition of rest frame frequency ν_0 is achieved, when the laser frequencies equal the respective Doppler-shifted frequencies ν_a and ν_p in the laboratory reference frame. As the number density of ions in the storage ring of about 4000 cm^{-1} is considerably smaller

[2] to first order of the Doppler effect

than in gas cells, the laser-induced fluorescence, rather than absorption, is used as the spectroscopic signal. The fluorescence is detected by a photomultiplier mounted perpendicularly to the ion beam. Due to the large Doppler shifts of the order of tens of nm caused by the high velocity of the ions, straylight from the lasers can easily be eliminated with color glas and interference filters in front of the photomultiplier, which detects the light at the ions' rest frame frequency because the observation angle is roughly perpendicular to the ion motion.

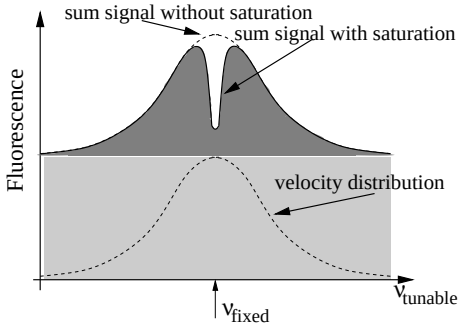

At first the ion velocity is chosen such that the fixed frequency laser is resonant with the ions belonging to the center of the velocity distribution. The tunable laser is scanned across the resonance. During a scan the fluorescence induced by the fixed-frequency laser is constant as indicated by the light grey area, whereas the tunable laser probes the velocity distribution leading to a Gaussian fluorescence signal [3]. For laser intensities far below saturation the total signal is the sum of these two contributions. However, in the case of saturation a Lamb dip occurs at the position, where both lasers are resonant with the same velocity class. Outside this frequency the two fluorescence contributions come from different ions and, therefore, add up.

For the Lamb dip the resonance conditions between the lasers and the ions read, according to the relativistic Doppler-effect,

$$\nu_{\mathrm{p}} = \gamma(1+\beta)\nu_0 \tag{2.13}$$

$$\nu_{\mathrm{a}} = \gamma(1-\beta)\nu_0. \tag{2.14}$$

Multiplying both equations and using the relation $\gamma = \sqrt{1/(1-\beta^2)}$ given by Special Relativity yields

$$\nu_{\mathrm{p}}\nu_{\mathrm{a}} = \nu_0^2. \tag{2.15}$$

Thus, for Special Relativity the square of the ions' rest frame frequency equals the product of the two laser frequencies *independently of the ion velocity* $\beta = v/c$. Essential for this velocity independence are the counterpropagating directions of the two laser beams.

Another approach to perform Doppler-free spectroscopy on $^7Li^+$ at TSR, which has already been employed to test time dilation [Grieser et al., 1994b],

[3] As will be seen later, the lifetime of the ions in the storage ring is of the same order of magnitude as a typical laser scan duration. Therefore, the induced fluorescence decreases significantly during a scan, which has to be taken into consideration in the analysis.

is optical-optical double resonance on a Λ-type three-level system, consisting of two slightly separated ground states and one common excited state, from which the ion decay back into either of the two ground states. The principle of the setup for this kind of spectroscopy is the same as for saturation spectroscopy. However, now each laser is tuned into resonance with either of the legs of the Λ. Ideally, a significant fluorescence signal is only observed, when both lasers are in resonance with the same ion, which leads to a subsequent back-and-forth pumping between the ground states. If only one laser is resonant with an ion, it will be pumped dark into the ground state not belonging to the resonant leg of the Λ. Again, the spectroscopic signal caused by back-and-forth pumping is only obtained when both lasers talk to the same velocity class of ions. Therefore, this method is to first order Doppler-free as well. In the case of Λ-spectroscopy and assuning again the validity of SR, the resonance condition reads, analogous to equation 2.15,

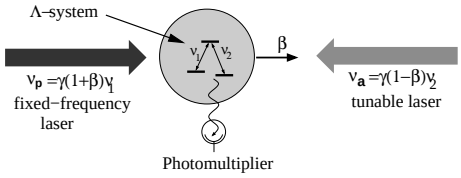

$$\nu_{\mathrm{p}}\nu_{\mathrm{a}} = \nu_1\nu_2, \tag{2.16}$$

where ν_1 and ν_2 denote the rest frequencies of the two legs of the Λ.

2.4 The TSR-experiment in the framework of Mansouri-Sexl

In order to quantify the significance of the TSR experiment as a test of Special Relativity, the interpretation of the experiment will be performed in the framework of the Mansouri-Sexl test theory. The analysis of the experiment in this test theory has been done by [Kretzschmar, 1992] and is outlined here shortly.

As already discussed in the previous section Mansouri and Sexl derive a generalized Lorentz transformation between a hypothetical ether frame Σ with coordinates (T, X, Y, Z) and frame S with coordinates (t, x, y, z) moving with a velocity $\vec{w} \cdot c$ with respect to Σ:

$$\begin{aligned} t &= aT + \vec{\epsilon}\vec{x} \\ \vec{x} &= -bT\vec{w} + b\hat{n}(\hat{n}\cdot\vec{X}) + d(\vec{X} - \hat{n}(\hat{n}\cdot\vec{X})) \end{aligned} \tag{2.17}$$

with $\hat{n} = \vec{w}/w$. This moving frame S is identified with the terrestrial rest frame. Another moving frame S' with coordinates (t', x', y', z') is introduced to represent the rest frame of the ions, which moves with velocity $\vec{w}' \cdot c$ in Σ. The inverse

transformation from S' to Σ is given by:

$$\begin{aligned} T &= \frac{1}{a'}(t' - \vec{\epsilon}'\vec{x}') \\ \vec{X} &= \frac{1}{d'}\vec{x}' + (\frac{1}{b'} - \frac{1}{d'})(\hat{n}' \cdot \vec{x}')\hat{n}' + \frac{1}{a'}(t' - \vec{\epsilon}' \cdot \vec{x}')\vec{w}' \end{aligned} \tag{2.18}$$

with $\hat{n}' = \vec{w}'/w'$. By inserting 2.18 into 2.17 one obtains the linear transformation between the ion rest frame S' and the laboratory frame S. Comparing a clock at rest in S' with clocks that are at rest in S one obtains

$$\Delta t = \Gamma(\vec{w}, \vec{w}')\Delta t' \tag{2.19}$$

with the time dilation factor given by

$$\Gamma(\vec{w}, \vec{w}') = \frac{a}{a'} + \frac{b}{a'}(\vec{\epsilon} \cdot [\hat{n}(\hat{n} \cdot \vec{w}') - \vec{w}]) + \frac{d}{a'}(\vec{\epsilon} \cdot [\vec{w}' - \hat{n}(\hat{n} \cdot \vec{w}')]), \tag{2.20}$$

which reduces, for Special Relativity, to

$$\Gamma_{\mathrm{SR}}(\vec{w}, \vec{w}') = \frac{1 - \vec{w} \cdot \vec{w}'}{\sqrt{(1 - w^2)(1 - w'^2)}} = \frac{1}{\sqrt{1 - \beta_{\mathrm{SR}}^2}}, \tag{2.21}$$

with

$$\beta_{\mathrm{SR}} = \frac{1}{1 - \vec{w} \cdot \vec{w}'}\sqrt{(\vec{w}' - \vec{w})^2 - (\vec{w} \times \vec{w}')^2}. \tag{2.22}$$

Here $\beta_{\mathrm{SR}} \cdot c$ denotes the velocity of S' relative to S in the case Special Relativity holds. Furthermore, the general Doppler shift formula can be derived. An ion at rest in the reference frame S' is considered to absorb light at a frequency ν_0. The lasers are at rest in the laboratory system S and the beams are aligned parallel or antiparallel with respect to the ion beam. In this case the ions see the light at frequency ν_0 if the laser frequency ν obeys the Doppler formula

$$\nu = \nu_0 \frac{\alpha(w'^2)}{\alpha(w^2)} \cdot \frac{1 \pm \beta_{\mathrm{SR}}}{\sqrt{1 - \beta_{\mathrm{SR}}^2}} \tag{2.23}$$

with the + sign for the parallel (p) and the - sign for the antiparallel (a) laser beams. Here, the substitutions $a(w) = \sqrt{1 - w^2} \cdot \alpha(w^2)$ and $a(w') = \sqrt{1 - w'^2} \cdot \alpha(w'^2)$ have been used. It turns out that all terms containing the parameters b', d' and ϵ' cancel. The Mansouri-Sexl test theory yields a Doppler formula, which is only modified by the factor $\alpha(w'^2)/\alpha(w^2)$ compared to Special Relativity. This modification is dependent on the *magnitudes*, but not on the *directions* of the velocities $\vec{w}$ and $\vec{w}'$. It is also not dependent on the clock synchronization procedure. A

deviation of this factor from unity indicates a violation of Special Relativity. The Doppler formula contains the generalized gamma factor

$$\gamma = \frac{\alpha(w'^2)}{\alpha(w^2)} \frac{1}{\sqrt{1-\beta_{\mathrm{SR}}^2}} = \frac{\alpha(w'^2)}{\alpha(w^2)} \gamma_{\mathrm{SR}}. \tag{2.24}$$

Now the test parameters are to be related to the frequencies measured in the storage ring experiment. The resonance conditions for the lasers overlapped parallel and antiparallel with the ion beam are given by the Doppler formula:

$$\nu_{\mathrm{p}} = \frac{\alpha(w'^2)}{\alpha(w^2)} \cdot \frac{1+\beta_{\mathrm{SR}}}{\sqrt{1-\beta_{\mathrm{SR}}^2}} \nu_0 \tag{2.25}$$

$$\nu_{\mathrm{a}} = \frac{\alpha(w'^2)}{\alpha(w^2)} \cdot \frac{1-\beta_{\mathrm{SR}}}{\sqrt{1-\beta_{\mathrm{SR}}^2}} \nu_0. \tag{2.26}$$

Multiplication of these equations yields

$$\nu_{\mathrm{a}} \nu_{\mathrm{p}} = \left[\frac{\alpha(w'^2)}{\alpha(w^2)} \right]^2 \nu_0^2. \tag{2.27}$$

The modification factor can be expanded as

$$\frac{\alpha(w'^2)}{\alpha(w^2)} = \frac{1+\alpha w'^2 + \alpha_2 w'^4 + \ldots}{1+\alpha w^2 + \alpha_2 w^4 + \ldots} \approx 1 + \alpha(w'^2 - w^2) + \ldots. \tag{2.28}$$

To estimate α the velocities w and w' must be known. The velocity w of the laboratory frame S relative to the ether frame Σ amounts to 350 km/s assuming the rest frame of the cosmic background radiation as our Σ. In contrast, the velocity w' of the ions with respect to Σ can not be measured directly. Instead it can be expressed in terms of the velocity $\vec{v} = \vec{\beta} \cdot c$ of the ions relative to the laboratory frame S. To first order approximation the relation between $(w'^2 - w^2)$ and $\vec{\beta}$ can be expressed by its special relativistic limit

$$\begin{aligned} (w'^2 - w^2)_{\mathrm{SR}} &= 1 - w^2 - \frac{(1-w^2)(1-\beta^2)}{(1+\vec{w}\cdot\vec{\beta})^2} \\ &\approx (\beta^2 + 2\vec{w}\cdot\vec{\beta}). \end{aligned} \tag{2.29}$$

Combining equations 2.27, 2.28 and 2.29 we get the final result

$$\frac{\nu_{\mathrm{p}} \nu_{\mathrm{a}}}{\nu_0^2} = 1 + 2\alpha(\beta^2 + 2\vec{w}\cdot\vec{\beta}) + \ldots \tag{2.30}$$

Experiment	Reference	upper limit for α
Ives-Stilwell	[Ives and Stilwell, 1938]	1×10^{-2}
Mößbauer rotor	[Champeney et al., 1963]	1×10^{-5}
Relativistic H^- beam	[MacArthur et al., 1986]	2.0×10^{-4}
Gravity Probe A	[Vessot et al., 1980]	1×10^{-6}
TPA experiment on Neon	[Riis et al., 1988]	$1. \times 10^{-6}$
TSR experiment (Grieser et al.)	[Grieser et al., 1994b]	8×10^{-7}

Table 2.1: *Results of previous measurements of time dilation.*

A deviation of the first order test parameter from its special relativistic value $\alpha = 0$ should therefore result in a constant frequency deviation as well as a diurnal and sidereal variation, which would be caused by the change of $\vec{w} \cdot \vec{\beta}$ through the rotation of the earth and the travel around the sun.

Another way to illustrate the significance of the test parameter α is to interprete it as a modification of the power of the gamma factor:

$$\begin{aligned} \gamma &= (1-\beta_{\mathrm{SR}}^2)^{-1/2-\alpha} = (1-\beta_{\mathrm{SR}}^2)^{-1/2}(1-\beta_{\mathrm{SR}}^2)^{-\alpha} \\ &= \gamma_{\mathrm{SR}}(1+\alpha\beta_{\mathrm{SR}}^2) + \ldots, \end{aligned} \tag{2.31}$$

which essentially gives equation 2.24 with the expansion 2.28.

2.5 Previous Ives-Stilwell-type experiments

Table 2.1 comprises the results of some previous Ives-Stilwell-type experiments expressed in an upper limit for the test parameter α (more precisely of $|\alpha|$) from the Mansouri-Sexl test theory. In some of the references the results are expressed in terms of the first component g_0 of the generalized metric tensor, which corresponds to α via [MacArthur, 1986] $1/g_0\gamma = 1+\alpha\beta^2+\ldots$. Since g_0 is, in contrast to α, dependent on the particle velocity in the experiment, g_0 is not suitable for comparing different experiments. The uncertainties of these test parameters are related via

$$\Delta\alpha = \frac{\Delta g_0}{\gamma\beta^2}. \tag{2.32}$$

Ives-Stilwell experiment

The first experiment measuring the transverse Doppler effect was done by Ives and Stilwell in 1938 [Ives and Stilwell, 1938]. The Doppler-shifted Hβ line of the emission of excited hydrogen canal rays were observed in two directions, with and against the motion of the particles with a spectrometer and compared with the

unshifted line. The effect to be observed was a shift of the center of gravity of these Doppler-shifted lines $\lambda_+ = \lambda\gamma(1+\beta)$ and $\lambda_- = \lambda\gamma(1-\beta)$ with respect to the unshifted line λ, which is predicted by Special Relativity to be caused by time dilation:

$$\overline{\lambda} = \frac{\lambda_+ + \lambda_-}{2} = \gamma\lambda. \tag{2.33}$$

The second order Doppler shift can be expressed as $\Delta'\lambda = \overline{\lambda} - \lambda \approx 1/2\lambda\beta^2$. The particle velocity β can be derived from the displacement $\Delta\lambda$ of λ_+ with respect to λ, which is mainly caused by the first order Doppler effect ($\gamma \approx 1$): $\Delta\lambda \approx \lambda\beta$. By the comparison of the second order Doppler shift with the first order shift time dilation could be confirmed, expressed in terms of the Mansouri-Sexl test parameter, by

$$\alpha < 1 \times 10^{-2}. \tag{2.34}$$

In contrast to the Michelson-Morley experiment and the Kennedy-Thorndike experiment, the Ives-Stilwell experiment manifests a positive effect instead of null-results.

Mößbauer rotor experiments

In this type of experiment a gamma ray source and a resonant absorber are mounted to opposite tips of fast rotor [Champeney et al., 1963]. In this arrangement Special Relativity predicts the emission frequency ν_1 to be equal to the absorber frequency ν. In the framework of the Mansouri-Sexl test theory we obtain [Mansouri and Sexl, 1977]

$$\nu = \nu_1(1 + 4\vec{\beta}\cdot\vec{w}\alpha). \tag{2.35}$$

$\vec{\beta}$ is the velocity of the source with respect to the laboratory frame. $\vec{w}$ denotes the velocity of the laboratory relative to a hypothetical preferred frame, which is identified with the rest frame of the cosmological background radiation. In this case we have $w = 350$ km/s. In the experiment by [Champeney et al., 1963] an upper limit for α of

$$\alpha < 1 \times 10^{-5} \tag{2.36}$$

has been derived from the observed temporal constancy of the absorbing frequency ν. In another experiment of this type a limit of

$$\alpha < \times 10^{-7} \tag{2.37}$$

is claimed. However, the publication of the data has only been announced [Isaak, 1970], but never performed.

Relativistic H beam

In this experiment by [MacArthur et al., 1986] a relativistic beam of atomic hydrogen ($\beta = 0.84$) in its ground state is excited with the 4^{th} harmonic of a Nd:YAG laser ($h\nu = 4.7$ eV). The photon energy in the atomic rest frame is varied by changing the angle between the laser beam and the atomic beam. For several well known $1s$ to np transitions the angle is measured and fit with the generalized Doppler formula $E_n = (E_0/g_0)\gamma(1 + \beta\cos\Theta)$. In this way the factor g_0 is determined and verified to be equal to unity with an accuracy of 2.7×10^{-4}. According to equation 2.32 this leads to an upper limit for α of

$$\alpha < 2.0 \times 10^{-4}. \tag{2.38}$$

Gravity Probe A

In the 1976 Gravity Probe A experiment a Scout-D rocket carrying a hydrogen maser frequency standard was launched to an altitude of 10,000 km. The frequency of this clock was compared to the frequency of another, identical hydrogen maser located on the earth. Originally intended for testing the gravitational redshift the experiment turned out to be sensitive to Special Relativity as well. As discussed in [Will, 1992], the absence of an effect of the angle between the rocket's velocity and the velocity of the earth with respect to the preferred reference frame on the gravitational redshift in the data led to a limit

$$\alpha < 1.0 \times 10^{-6}. \tag{2.39}$$

TPA experiment on neon

A time dilation test experiment similar to that described in this thesis has been performed in Aarhus by means of collinear two-photon absorption spectroscopy (TPA) on a 120 keV atomic neon beam ($\beta = 3.5 \times 10^{-3}$). The atoms were excited from an initial level i to an excited state f via an intermediate level m using counterpropagating laser beams of equal frequency ν_{L}. This laser frequency has to be controlled so that the two photons can accomplish the required two-photon transition, whereas the atomic beam velocity is controlled to make the intermediate transition occur. This is done by servo loops adjusting the two parameters to maintain maximum resonant absorption. In an analysis by [Will, 1992] the experiment has been described in terms of the Mansouri-Sexl test theory:

$$\nu_{\text{L}} = \sqrt{\nu_1\nu_2} \cdot [1 \quad + \quad \alpha\beta^2 + 2\alpha\vec{\beta}\vec{w} + \ldots] \tag{2.40}$$

Here, $\beta \cdot c$ and $w \cdot c$ are the velocities of the atoms relative to the laboratory and that of the laboratory with respect to the preferred frame, respectively. ν_1 and ν_2

are the transition frequencies of the two-photon transition in the rest frame of the ion.

In a first version of the experiment the two-photon resonance was compared to another two-photon resonance on neon in a gas cell at rest. In this way an upper bound for α was found from the term $\alpha\beta^2$: $\alpha < 2.0 \times 10^{-5}$ [Kaivola et al., 1985].

A second measurement observed the constancy of the fast beam resonance as compared to an iodine hyperfine structure line measured at rest over a period of several weeks. In this way, a limit was put on possible diurnal variations caused by the $2\alpha\vec{\beta} \cdot \vec{w}$ term. An upper bound of

$$\alpha < 1.4 \times 10^{-6} \tag{2.41}$$

was found [Riis et al., 1988].

Storage ring experiment by Grieser et al.

The storage ring experiment by [Grieser et al., 1994b] in 1994 at TSR in Heidelberg is the precursor of the experiment described here, the principle has been presented in the preceding sections. Grieser et al. used Λ-type spectroscopy in order to measure the transverse Doppler shift on a fast $^7Li^+$ beam. Following a similar argumentation as in section 2.4 one derives the analogous formula to equation 2.30, namely

$$\frac{\nu_a \nu_p}{\nu_1 \nu_2} = 1 + 2\alpha\beta^2 + \ldots, \tag{2.42}$$

which can be rewritten as

$$\nu_a - \nu_a^{SR} = 2\alpha\beta^2 \nu_a^{SR}, \tag{2.43}$$

where $\nu_a^{SR} = \nu_1\nu_2/\nu_p$ is the resonance frequency of the antiparallel laser beam if SR holds.

The difference of the measured resonance frequency and the value predicted by Special Relativity was

$$\nu_a^{exp} - \nu_a^{SR} = 4.4 \pm 3.2 \text{ MHz}, \tag{2.44}$$

which agrees within 2σ. This leads to the best upper limit for deviations from relativistic time dilation so far:

$$\alpha < 8 \times 10^{-7}. \tag{2.45}$$

2.6 The $^7Li^+$ ion

Experiments like high precision laser spectroscopy or laser cooling at heavy ion storage rings require ions with a strong E1 transition within the optical frequency range. Several requirements such as the accessibility by lasers and the condition, that the transition has to start from the ionic ground state or from a long-lived metastable state, restrict the experiment to the ion species listed in table 2.2.

	$^7Li^+$	$^9Be^+$	$^{24}Mg^+$
lower level	$2s^3S_1(F=5/2)$	$2s^2S_{1/2}(F=2)$	$3s^2S_{1/2}$
upper level	$2p^3P_2(F=7/2)$	$2p^2P_{1/2}(F=1)$	$3p^2P_{1/2}$
transition wavelength	548.5 nm	313 nm	280 nm
lifetime of lower level	50 s	stable	stable
lifetime of upper level	43 ns	8.7 ns	3.7 ns

Table 2.2: *Atomic ions suitable for laser experiments at storage rings*

Laser cooling of an ion beam has first been demonstrated at TSR on $^7Li^+$ [Schröder et al., 1990], but was also investigated on $^9Be^+$ [Eisenbarth, 2001], [Lauer et al., 1998], [Miesner et al., 1996], again at TSR, as well as on $^{24}Mg^+$ [Hangst et al., 1991] at ASTRID in Aarhus.

However, in our experiment the transition frequency of an atomic ion is to be used as a fast moving clock in order to measure the relativistic Doppler shift. To this end, the accurate knowledge of the rest frame frequency is indispensable. Additionally, a narrow linewidth is desirable for high precision spectroscopy. Both requirements restrict the experiment to the heliumlike $^7Li^+$ ion. It has a strong optical transition $2s\ ^3S_1 \rightarrow 2p\ ^3P_2$ at 548.5 nm in the triplet system shown in figure 2.1. The lower level of this transition has a radiative lifetime of 50 seconds [Saghiri, 1999] in vacuum, which is, however, decreased to about 15 seconds by stripping due to collisions with the rest gas ions as well as electron impact ionization in the electron cooler, when stored in the TSR at a typical rest gas pressure of 5×10^{-11} mbar. This metastable ground state lies 59 eV above the singlet ground state. The ionization energy amounts to 75.6 eV. The lifetime of the upper level is 43 ns [Kowalski et al., 1983] corresponding to a natural linewidth of the transition of 3.8 MHz. The saturation intensity for the closed two-level system has been calculated to be 6.7 mW/cm^2 for linearly polarized light [Wanner et al., 1998]. Both Doppler-shifted transition frequencies lie in the optical region, even for extremely high ion velocities accessible at the ESR storage ring at GSI[4] in Darmstadt. The $^7Li^+$ ion has a nuclear spin of 3/2 leading to the hyperfine structure shown in figure 2.1. The splittings between these hfs-components

[4]GSI: Gesellschaft für Schwerionenforschung

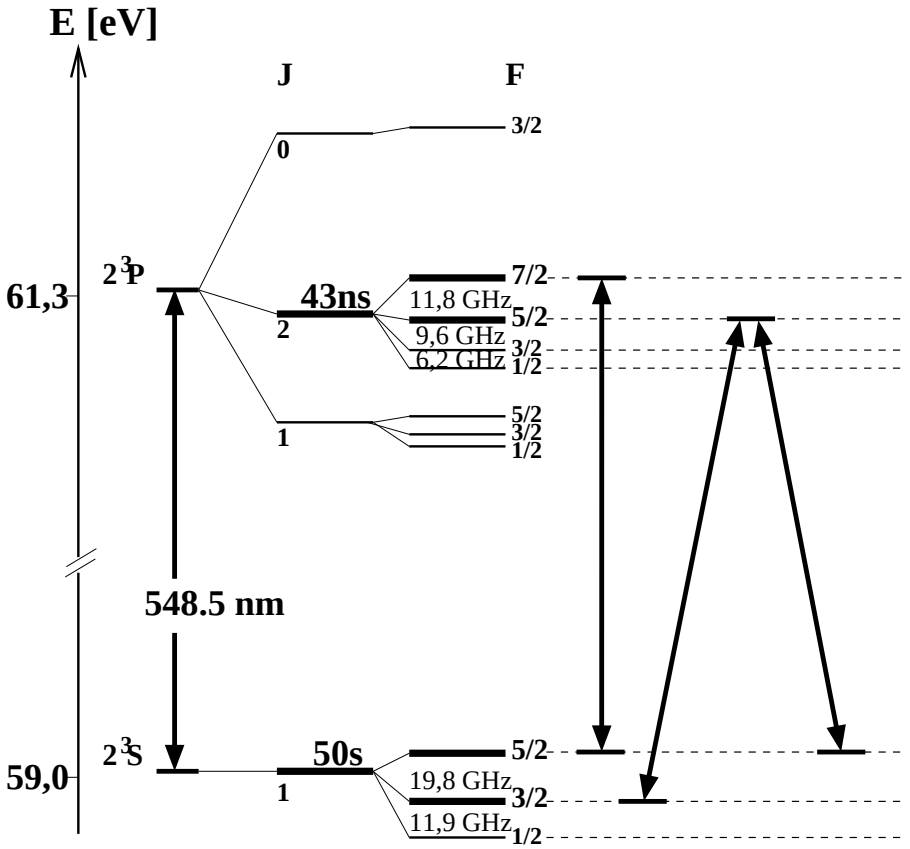

Figure 2.1: *Level-scheme of the triplet system in $^7Li^+$, which is ortho-heliumlike. It contains a closed Λ-system, which is used for Doppler-free Λ-spectroscopy, and a closed two-level system suitable both for ion beam diagnosis experiments using laser-induced fluorescence and Doppler-free saturation spectroscopy.*

are of the order of 10 to 20 GHz in the $^3S_1$ and $^3P_2$ levels, which is larger than the Doppler width caused by the velocity distribution of the ion beam. Therefore, the $2s\ ^3S_1(F = 5/2) \rightarrow 2p\ ^3P_2(F = 7/2)$ transition can be well described by a closed two-level system. The transitions $2s\ ^3S_1(F = 5/2) \rightarrow 2p\ ^3P_2(F = 5/2)$ and $2s\ ^3S_1(F = 3/2) \rightarrow 2p\ ^3P_2(F = 5/2)$ form a closed three-level Λ-system.

For the time dilation test experiment using Lamb dip saturation spectroscopy on this level its rest frame frequency has to be known very accurately. Unfortunately, different experiments reporting strongly disagreeing results especially for the absolute frequency, but also for the fine structure have been published. Table 2.3 summarizes the frequencies relevant for the test experiment.

Table 2.3 shows the results of two independent measurements of the absolute frequency of the $^3S_1(5/2) \rightarrow ^3P_2(7/2)$ transition by [Rong et al., 1998]

Transition		Frequency [MHz]	Reference
electronic transition:			
$^3S_1(5/2) \rightarrow ^3P_2(7/2)$		546 466 916.49(87)	[Rong et al., 1998]
	*	546 466 918.79(40)	[Riis et al., 1994]
fine structure splitting:			
$^3P_1(3/2) \rightarrow ^3P_2(3/2)$		57 962.3(7)	[Rong et al., 1993]
		57 973.29(65)	[Riis et al., 1994]
		57 974.37(33)	[Clarke and van Wijngaarden, 2002]
	Theory$\rightarrow$	57 973.20(23)	[Riis et al., 1994]
relevant hfs splittings:			
$^3S_1(3/2) \rightarrow ^3S_1(5/2)$		19 817.673(13)	[Kowalski et al., 1983]
	$\circ$	19 817.90(24)	[Clarke and van Wijngaarden, 2002]
	Theory$\rightarrow$	19 817.680(25)	[Riis et al., 1994]
$^3P_2(5/2) \rightarrow ^3P_2(7/2)$		11 775.8(2)	[Kowalski et al., 1983]
	$\circ$	11 774.04(31)	[Clarke and van Wijngaarden, 2002]
	Theory$\rightarrow$	11 773.05(18)	[Riis et al., 1994]

Table 2.3: *Transition frequencies relevant for the present test experiment. The electronic transition is used for the Lamb dip spectroscopy. For the present experiment the value indicated with a star (*) is used (see text). The hyperfine splittings indicated with circles ($\circ$) are used to calculate the frequencies of the electronic transitions of the Λ-system for a reanalysis of the previous test experiment by [Grieser et al., 1994b]. All errors correspond to the 1σ level.*

and [Riis et al., 1994] which disagree by almost 2σ. Both groups also published results on the *fine structure* ([Rong et al., 1993], [Riis et al., 1994]). [Rong et al., 1993] determined the three fine structure transitions $^3P_0(3/2) \rightarrow ^3P_1(5/2)$, $^3P_0(3/2) \rightarrow ^3P_2(7/2)$ and $^3P_2(7/2) \rightarrow ^3P_1(5/2)$ with a so-called laser heterodyne method using several iodine lines as frequency markers. With help of the results of [Kowalski et al., 1983] or [Clarke and van Wijngaarden, 2002] for the hyperfine structure splittings all other fine structure transitions can be calculated. In [Riis et al., 1994], three absolute frequencies of the transitions $^3S_1(5/2) \rightarrow ^3P_0(3/2)$, $^3S_1(3/2) \rightarrow ^3P_1(5/2)$ and $^3S_1(5/2) \rightarrow ^3P_2(7/2)$ have been determined, from which, again with the hyperfine structure results from [Kowalski et al., 1983], all fine structure transitions of the ^3P level can be determined. Table 2.3 shows the results of both groups for the $^3P_1(3/2) \rightarrow ^3P_2(3/2)$ fine structure transition. In addition, a theoretical value reported in [Riis et al., 1994] and a recent remeasurement of the transition by [Clarke and van Wijngaarden, 2002] is listed. The two first measure-

ments ([Rong et al., 1993], [Riis et al., 1994]) are claimed to have 1σ errors of below 1 MHz, but show a discrepancy of 11 MHz, which corresponds to 9σ. The Riis result agrees very well with the theoretical prediction. Furthermore, the remeasurement by [Clarke and van Wijngaarden, 2002] confirms the Riis result within slightly more than 1σ so that there is strong indication for the Riis measurement to be the correct one. As mentioned, both groups ([Riis et al., 1994] and [Rong et al., 1998]) measured the absolute frequency of the $^3S_1(5/2) \rightarrow ^3P_2(7/2)$ transition as well. Since the measurements by [Clarke and van Wijngaarden, 2002] concerning the fine structure confirm the results obtained by [Riis et al., 1994] and, additionally, these results agree with theory, we adopt the absolute frequency of the $^3S_1(5/2) \rightarrow ^3P_2(7/2)$ transition from the Riis measurement for the present test experiment discarding the result from the heterodyne laser spectroscopy.

When using Λ-type spectroscopy as in [Grieser et al., 1994b], also the hyperfine structure splittings $^3S_1(3/2 \rightarrow 5/2)$ and $^3P_2(5/2 \rightarrow 7/2)$ are needed to determine the absolute frequencies of the two legs of the Λ from the $^3S_1(5/2) \rightarrow ^3P_2(7/2)$ transition frequency. The *hyperfine structure* splittings of the ^3S as well as for the ^3P states have been measured by [Kowalski et al., 1983][5] and, recently, by [Clarke and van Wijngaarden, 2002] employing different methods. The results of both measurements for the relevant splittings together with the theoretical values from [Riis et al., 1994] are given in table 2.3.

However, for the $^3P_2(5/2 \rightarrow 7/2)$ transition the measurements disagree by 3.6 σ. The new result by [Clarke and van Wijngaarden, 2002] agrees with theory within 2σ, whereas that by [Kowalski et al., 1983] deviates by 7σ. As the old test experiment [Grieser et al., 1994b] used the deviating value of the $^3P_2(5/2 \rightarrow 7/2)$ transition by [Kowalski et al., 1983], we tentatively reanalyzed their result using the new value by [Clarke and van Wijngaarden, 2002]. See chapter 5.

The discrepancy between the two measurements of the $^3S_1(5/2) \rightarrow ^3P_2(7/2)$ electronic transition makes a new measurement desirable, which, however, appears to be difficult. As an alternative, we plan to replace the rest frame frequency by the measurement of the Doppler-shifted frequency at the lowest possible ion velocity at TSR.

[5] [Kowalski et al., 1983] and [Rong et al., 1993] employ the same method

Chapter 3

Experimental Setup

3.1 The Heidelberg Test Storage Ring

The ion beam used in the experiment described here is provided by a Tandem van-de-Graaff accelerator, which starts with negatively charged ions extracted from a metal ionized sputtering source (MISS) close to ground potential. The ions are first accelerated towards the positively charged terminal of the Tandem, which can be biased up to 12 MV. Inside the terminal the ions pass through a nitrogen gas cell, where electrons are stripped off by collisions. The resulting positively charged ions are then further accelerated by the same terminal voltage.

In the present experiment $^7Li^-$ ions were extracted from the sputter source, stripped to $^7Li^+$ in the terminal and accelerated to a final energy of 13.3 MeV corresponding to $\beta = v/c = 0.064$. About 10% are found to be in the triplet state 2^3S_1 (see chapter 5.3).

The storage of an ion beam requires both bending forces to keep the particles on a closed orbit and, as the ions repel each other due to the Coulomb interaction, focussing forces in the two transversal directions. The lattice of the TSR is shown in figure 3.1. Eight 45° dipole magnets, grouped in pairs, form a closed orbit of 55.4 m circumference in a square configuration and twenty quadrupole magnets accomplish the focussing. In order to bend an ion of mass m, charge q and velocity v on a circle with radius ρ, the dipole magnets have to impose a Lorentz force $qBv = mv^2/\rho$ which can be solved for the *magnetic rigidity*

$$B\rho = \frac{mv}{q} \tag{3.1}$$

of the ion beam. The maximum magnetic rigidity attainable at TSR amounts to $(B\rho)_{\max} = 1.4$ Tm.

Due to the transverse focussing the ions perform an oscillatory motion around the central orbit ('sollbahn'). These so-called betatron oscillations are determined

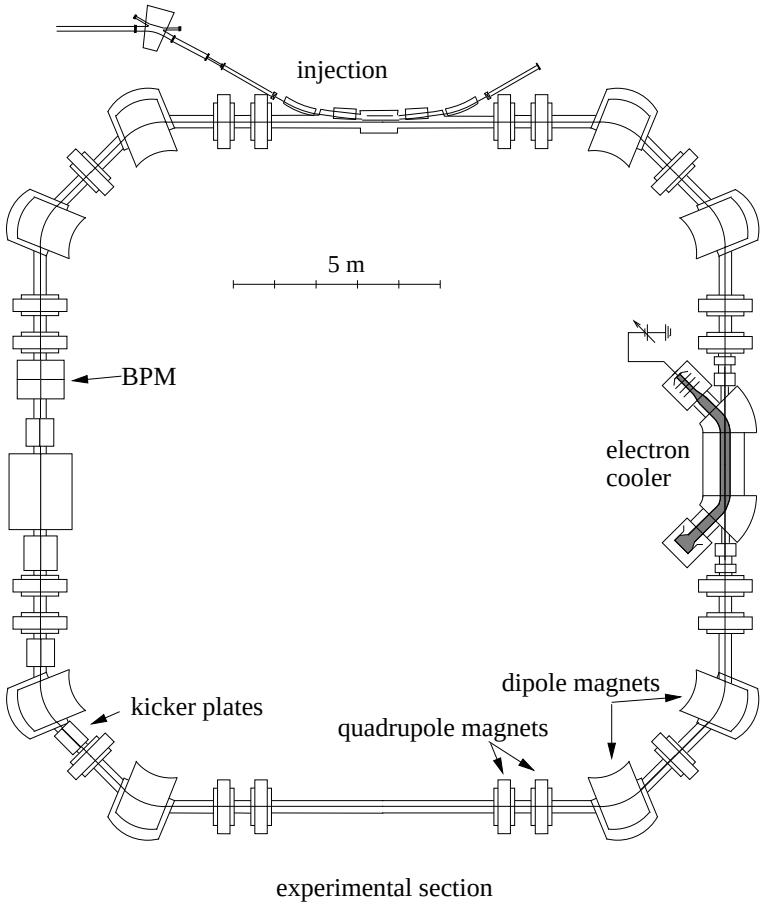

Figure 3.1: *The TSR: Four pairs of two 45 degree dipole magnets bend the ion beam on a closed orbit. Twenty quadrupole magnets focus the beam in order to compensate for the Coulomb repulsion. A cold electron beam is provided by the electron cooler and overlapped with the ion beam over an interaction region of about 1.5 m. Thereby, the ions are phase-space cooled both in the longitudinal and the transverse direction. Furthermore, the exact ion velocity is fixed by the electron velocity. The kicker plates are parallel capacitor plates, to which an rf-signal can be applied in order to bunch the ion beam. In this way, ion velocity fluctuations due to drifts in the acceleration voltage of the electron cooler are prevented.*

by the bending radius ρ in the dipole magnets as well as the focussing strength K of the quadrupole magnets, respectively, and can approximately be described by a Hill's type differential equation:

$$\frac{\mathrm{d}^2 y_{\mathrm{h,v}}(s)}{\mathrm{d}s^2} + K(s) \cdot y_{\mathrm{h,v}}(s) = \frac{1}{\rho}\frac{\Delta p}{p_0}. \tag{3.2}$$

$y_{\mathrm{h,v}}(s)$ is the transverse displacement from the central orbit in the horizontal (h) and vertical (v) direction, s is the longitudinal beam parameter and Δp is the deviation from the design momentum p_0.

A solution of the homogeneous equation ($\Delta p/p_o = 0$) reads, omitting the indices h and v,

$$y(s) = a_{\mathrm{y}} \cdot \sqrt{\beta(s)}\cos(\psi(s) + \delta). \tag{3.3}$$

The ions thus perform pseudoharmonic oscillations around the central orbit with the *s-dependent* amplitude $A_{\mathrm{y}} = a_{\mathrm{y}}\sqrt{\beta(s)}$ and betatron phase $\psi(s) = \int ds/\beta(s)$. δ is an arbitrary phase. $\beta(s)$ is the so-called beta function, which is an intrinsic property of the storage ring lattice. Figure 3.2 shows the horizontal and vertical beta functions for TSR.

The set of points $(y(s), y'(s))$ for all phases $0 \leq \delta \leq 2\pi$ in the phase space forms an ellipse centered at the central orbit. According to Liouville's theorem the area F of this ellipse

$$F = \pi a_{\mathrm{y}}\sqrt{\beta(s)} \cdot \frac{a_{\mathrm{y}}}{\sqrt{\beta(s)}} = \pi a_{\mathrm{y}}^2 \tag{3.4}$$

stays constant, whereas the shape and orientation change along s. The ellipse area contains all ellipses of particles with betatron amplitudes smaller than or equal to a_{y}. It is usually described by the *emittance* ϵ

$$\epsilon = \frac{F}{\pi}. \tag{3.5}$$

Replacing a_{y} by ϵ in equation 3.3 the beam envelope

$$E(s) = y_{\max}(s) = \sqrt{\epsilon\beta(s)} \tag{3.6}$$

and the beam divergence

$$A(s) = y'_{\max}(s) = \sqrt{\epsilon}\sqrt{\frac{1 + (\frac{1}{2}\beta'(s))^2}{\beta(s)}} \tag{3.7}$$

can be calculated once the emittance of the beam and the beta function of the lattice is known. The determination of the emittance is described in chapter 5.

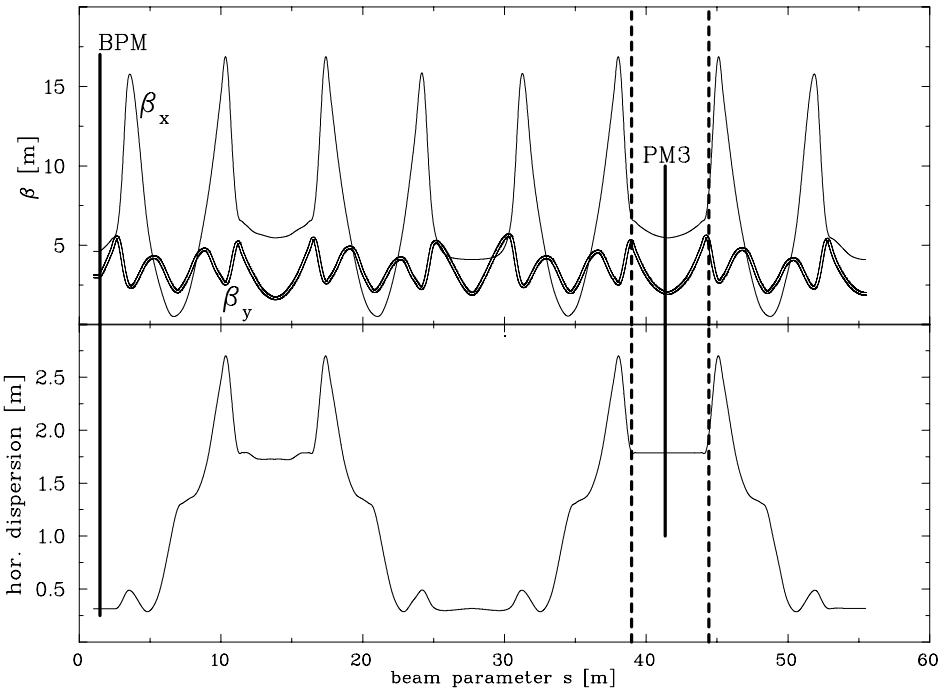

Figure 3.2: *Horizontal and vertical beta function as well as ring dispersion of TSR. The experimental section relevant for the $^7Li^+$ experiment is indicated by the dashed lines.*

Up to now we have only considered particles with design momentum p_0. Ions with a momentum deviation, however, experience a different bending radius in the dipole magnets due to the velocity dependence of the Lorentz force. This leads to a horizontal displacement $\Delta y_\mathrm{h} = \Delta p/p_0 \cdot D(s)$ of the central orbit, around which the ions perform betatron oscillations. The dispersion function $D(s)$, which is an intrinsic property of the storage ring lattice, is shown in fig. 3.2 for TSR. The change of the momentum together with a change of the length of the central orbit involved in the dispersion leads to a corresponding change of the revolution frequency. The relation between momentum deviation and revolution frequency deviation is [Wille, 1996]:

$$\frac{\Delta f}{f} = \eta \frac{\Delta p}{p_0}, \tag{3.8}$$

where the machine-specific so-called *slip factor* for TSR is $\eta = 0.985$. This relation is used to determine $\Delta p/p_0$ by Schottky analysis described below.

The injection of the ion beam provided by the accelerator is accomplished by means of two magnetic septa and one electric septum. To accumulate a large number of particles the transverse acceptance of TSR of 120π mm mrad is designed

much larger than the emittance of the injected beam ($\epsilon = 1.5\pi$ mm mrad). The filling of the transverse phase space is achieved by four bumper magnets, which create a local bump of the closed orbit so as to coincide with the trajectory of the injected ion beam. After start of the injection the field in the bumper magnets and, therefore, also the bump is reduced to zero within 300 μs. In this way, up to 40 orbits are stored side by side. During this so-called multiturn injection process the amplitude of the betatron oscillation around the closed orbit increases making phase space cooling indispensable (see next section).

3.1.1 The Electron Cooler

In order to provide a high ion beam quality, which plays a crucial role in the high precision experiment described here, the technique of electron cooling is indispensable. In the injection process the ion beam is heated up both in the vertical and horizontal degree of freedom. It then has a diameter of the order of $d \approx 18$ mm (FWHM) and a divergence of about 2 mrad in the straight sections (see figure 3.4). The large diameter restricts the control of the parallel alignment of the laser beams with respect to the ions (see section 3.4). This, as well as the large divergence, leads to a significant frequency error in the spectroscopy. Therefore, the ion beam has to be phase-space cooled, especially in the transverse degrees of freedom. In addition, the ion velocity has to be contolled very accurately both to tune the ions into resonance with the fixed-frequency laser and to keep the velocity stable at the desired value. This cannot be accomplished by the accelerator. These demands to the beam quality, accurate control of the ion beam energy as well as (transverse) cooling, are secured by electron cooling. For minimizing AC-Stark shifts (see section 5.4.2) an even further stabilization of the velocity is achieved by ion beam bunching, which is described in the next section.

The principle of electron cooling invented by Budker [Budker, 1967] bases on the Coulomb interaction of an ion beam with a cold co-moving electron beam and was first implemented at the NAP-M proton storage ring at Novosibirsk [Budker et al., 1976]. Figure 3.1 shows a sketch of the electron cooler device installed in the second straight section of TSR. Electrons are released from a heated cathode at negative potential U_c and accelerated towards ring-shaped anodes on ground potential. The cathode is mounted in a strong longitudinal magnetic field ($B_1 \approx 1$T), provided by a solenoid magnet, in order to guide the electrons, which are, thereby, forced onto cyclotron orbits around the magnetic field lines. After acceleration the electrons enter a region, where the guiding field is adiabatically lowered to $B_2 \approx 20 - 70$ mT, expanding the electron beam by the expansion factor $\beta = B_1/B_2$ ($\beta = 9$ in our experiment). In the following toroid the magnetic field is bent by 45 degrees in order to merge the electron beam and the ion beam. After an interaction region of 1.5 m length the beams are separated

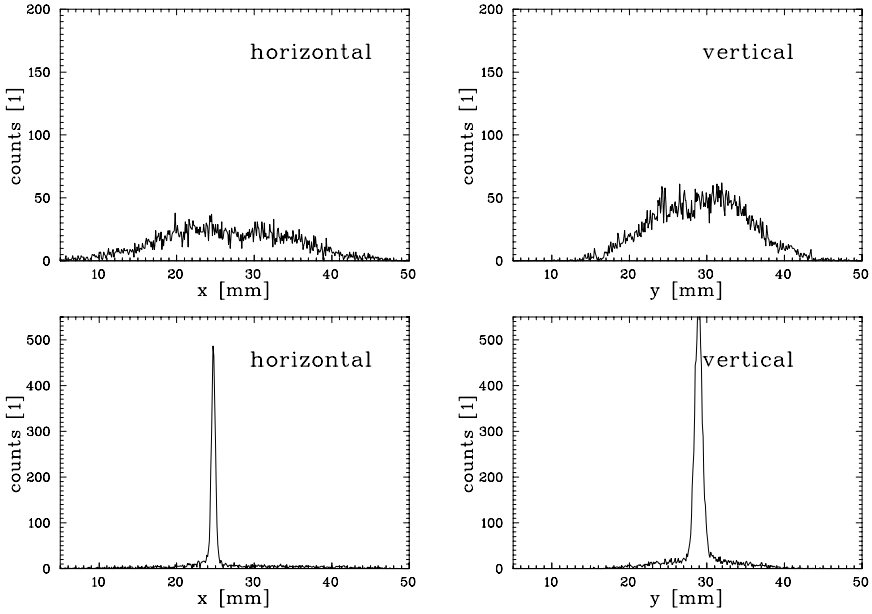

Figure 3.3: *Horizontal and vertical ion beam profile right after injection (above) and after 8 seconds of electron cooling (below) for the experiment with $^7Li^+$. These profiles contain the instrument resolution of the beam profile monitor and additionally depend on the position s in the storage ring.*

again by a second 45 degree toroid magnet. To prevent back-reflection into the interaction region the electrons are collected efficiently by a Faraday cup.

Due to the acceleration and the adiabatic expansion the longitudinal and transverse temperatures of the electrons, which are decoupled by the magnetic field, decrease [Schmitt, 1999] from T_{cathode} (typically 1100 K) to a strong anisotropic velocity distribution with temperatures of typically $T_{\parallel} \approx 0.1$ meV and $T_{\perp} \approx 14$ meV.

The cathode potential U_c is chosen such that the average electron velocity matches the desired ion velocity. Coulomb collisions between the electrons and the ions in the interaction region lead to a friction force damping the movement of those ions, which have a higher velocity than the electrons and accelerating the slower ones. This can be described by a friction force in both the longitudinal and the transverse direction. As a result not only the longitudinal velocity spread is strongly decreased, but also the beam diameter as well as the divergence shrink by a factor of about 40 (see figure 3.4). At equilibrium the ion beam has a σ-width of about 250 μm, a divergence of 50 μrad and a longitudinal momentum spread of $\Delta p/p = 8 \times 10^{-5}$.

The exact velocity of the electrons in the beam is determined by the total

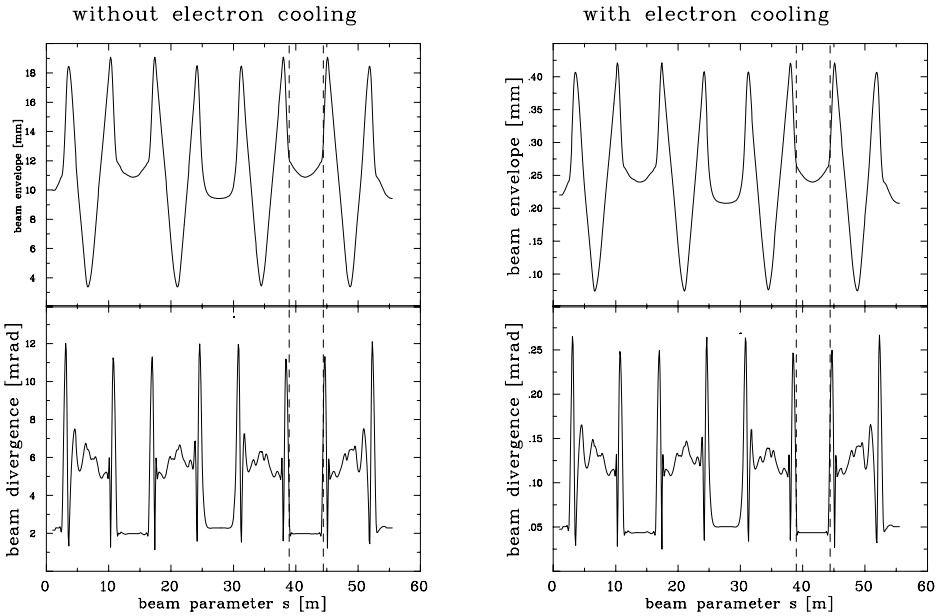

Figure 3.4: *Horizontal beam width (1σ envelope) and divergence as a function of the beam parameter s for an uncooled as well as for an electron-cooled $^7Li^+$ ion beam. The curves are calculated after equations 3.6 and 3.7 using the transverse emittance determined from beam profile measurements (see below).*

potential at its position. As the outer electrons partially screen the potential, it decreases towards the beam axis. The resulting radial dependence of this space charge potential can be calculated ([Grosser, 1983]) as:

$$U_{sp}(r) = \left\{ \begin{array}{ll} \frac{I_e}{4\pi\epsilon_0 v_e}(1 - \frac{r^2}{R_{\rm beam}^2} + 2\ln\frac{R_{\rm tube}}{R_{\rm beam}}) & r \leq R_{\rm beam} \\ & \\ \frac{I_e}{2\pi\epsilon_0 v_e}\ln\frac{R_{\rm tube}}{r} & r \geq R_{\rm beam}. \end{array} \right\} \qquad (3.9)$$

$I_e = 41$ mA and $v_e = 0.064c$ are typical values for the electron current and the electron velocity in our experiment. The radius of the beam tube is $R_{\rm tube} = 10$ cm, that of the electron beam $R_{\rm beam} = 2.6$ cm. As the ion velocity of an electron-cooled beam is determined by the electron velocity, the ion beam has to be spatially stable. A transverse movement of the ion beam would lead to a change of the longitudinal ion velocity.

3.1.2 Ion beam bunching

The ion velocity of an electron-cooled beam is determined by the velocity of the electrons and, therefore, by the cathode voltage U_c. However, the stability of the

power supply (FUG) is limited to 10^{-4} leading to ion velocity shifts of the order of a few widths of the velocity distribution. As a consequence, the argon ion laser is not fixed in resonance with the center of the distribution, which results in intensity fluctuations as well as a frequency shift due to the AC-Stark effect (see section 5.4.2). The ions can even be drifting out of resonance completely. In addition, instabilities, e.g of the magnetic fields of the TSR magnets can cause small transverse beam displacements. Due to the space charge parabola of the electron beam these displacements are translated into velocity fluctuations. The fluorescence measurements of the velocity distribution revealed a small 50 Hz jitter and a very slow fluctuation at a frequency of ≈1.6 Hz. In order to suppress these instabilities we apply the well-established technique of ion beam bunching [Wille, 1996]. This method has been investigated in detail in the course of laser cooling experiments at TSR [Eisenbarth, 2001], where it serves as the counterforce to the laser force. As in these experiments we utilize the horizontal kicker plates[1] installed in the third section of the storage ring, to which we apply an rf-signal $U(t) = U_0 \cos 2\pi\nu_{\mathrm{rf}} t$ at the harmonic h of the average revolution frequency ν_{rev} of the ions ($\nu_{\mathrm{rf}} = h\nu_{\mathrm{rev}}$) in the way depicted in figure 3.5. Both plates, which have a length of 20 cm, are set to the same potential resulting in a longitudinal electric field along the beam axis. Ions, that enter the kicker device at the voltage $U(t)$, leave it at $U(t + \Delta t)$, where Δt is the time of flight through the device. Thus, the ions experience a net potential difference $\Delta U(t) - U(t + \Delta t) \approx \dot{U}(t)\Delta t$ assuming Δt to be short compared to the rf period. With the parametrization $t(s) = \gamma^2\eta h s/(\nu_{\mathrm{rf}} C)$ (h : harmonic number, $C = 55$ m ring circumference, $\eta = 0.985$: machine parameter) one can deduce a position-dependent force $F_{\mathrm{rf}}(s) = e\Delta U(t(s))/C$, averaged over the ring circumference C. This force can be described by a pseudopotential

$$V_{\mathrm{rf}}^{(\mathrm{s})} = \frac{eL_{\mathrm{eff}}h}{\gamma^2\eta C} U(t(s)) \tag{3.10}$$

moving in the ring with the synchroneous velocity $v_{\mathrm{s}} = \nu_{\mathrm{rf}} C/h$. $L_{\mathrm{eff}} = 10$ cm is the effective length of the kicker plates [Eisenbarth, 2002]. For sinusoidal potentials, ions with a small amplitude oscillate in this pseudopotential with the velocity-independent synchrotron frequency

$$\nu_{\mathrm{sync}} = \sqrt{\frac{L_{\mathrm{eff}} h^2 e U_0 \eta}{m_0 \gamma C^3}}, \tag{3.11}$$

where m_0 is the ion rest mass. For $U_0 = 30$ V the synchrotron frequency in our experiment is about $\nu_{\mathrm{sync}} \approx 47$ Hz.

[1] The kicker plates are usually used for the slow extraction technique in molecular physics experiments at TSR [Albrecht et al., 1996].

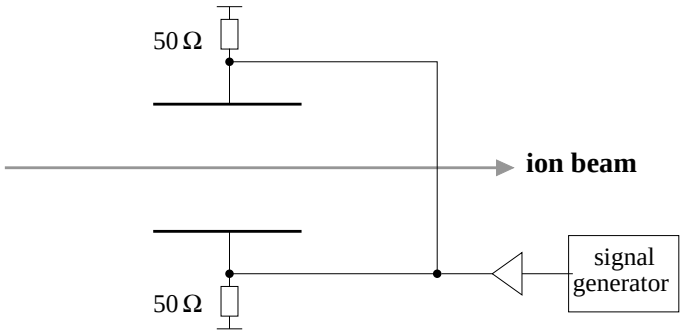

Figure 3.5: *Sketch of the bunching setup. The rf-signal from a signal generator is amplified and applied to both plates of a capacitor placed around the ion beam.*

3.2 Ion beam diagnosis

A fast and non-destructive ion beam diagnosis is essential for successful operation of a storage ring. In our experiment the longitudinal momentum distribution is determined by Schottky analysis, whereas the transverse profile is measured with the beam profile monitor (BPM). In addition to these universal methods, the $^7Li^+$ beam contains a closed two-level transition, which is accessible by lasers. This makes another longitudinal diagnostic tool, the fluorescence measurement, possible. These methods are described in the following.

Schottky analysis

Schottky analysis [Boussard, 1985] allows to determine the revolution frequency of the ions in the storage ring. To this end, a capacitive pickup is installed in TSR, which detects the noise signal produced by the circulating ions. A single ion would lead to an infinite series of equally spaced delta spikes reflecting the revolution frequency f_0. A Fourier expansion shows a line spectrum with one discrete line at each harmonic of f_0. For an ensemble of randomly distributed ions each line at frequency nf_0 is replaced by a frequency band around f_0 with a width, according to equation 3.8, of

$$\Delta f = nf_0 \cdot \eta \frac{\Delta p}{p_0}. \tag{3.12}$$

Hence, the relative momentum spread $\Delta p/p_0$ can be determined from the Schottky spectrum, whereas the absolute momentum p_0 is dependent on the orbit length,

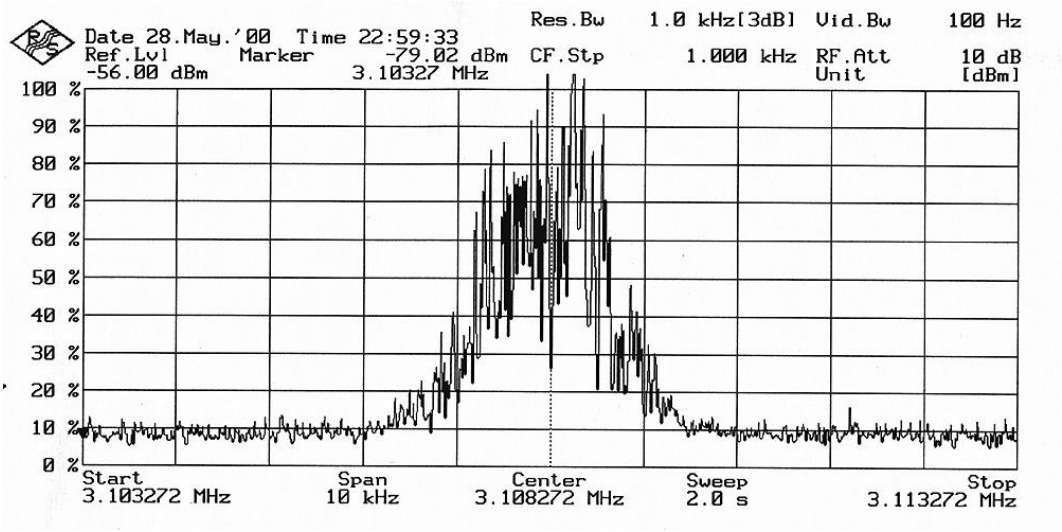

Figure 3.6: *Schottky-spectrum of the $^7Li^+$ ion beam during electron cooling measured at the 9^{th} harmonic of the ion revolution frequency . In this example the equilibrium temperature has not yet been reached. According to equation 3.12 the signal width corresponds to a momentum spread of $\Delta p/p \approx 5 \times 10^{-4}$.*

which is not known sufficiently accurate for our experiment. However, it is possibble to measure p_0 with the aid of the dye laser as follows.

Fluorescence measurement

The tunable dye laser provides another tool for the investigation of the longitudinal velocity distribution. To this end the laser is tuned across the $5/2 \rightarrow 7/2$ transition. Due to the Doppler effect the frequency distribution of the laser-induced fluorescence translates into a velocity distribution via

$$P(\beta)\mathrm{d}\beta = P_\nu(\nu(\beta))\frac{\mathrm{d}\nu}{\mathrm{d}\beta}\mathrm{d}\beta \tag{3.13}$$

with

$$\frac{\mathrm{d}\nu}{\mathrm{d}\beta} = -\gamma\nu_0\frac{1}{1+\beta} \tag{3.14}$$

as the laser beam is antiparallel to the ion beam, i.e. $\nu = \gamma(1-\beta)\nu_0$. When the laser is aligned exactly collinear with respect to the ion beam, the actual ion velocity can, in contrast to the Schottky method, be determined to high accuracy because the rest frame frequency ν_0 as well as the laboratory frame frequency ν can be determined very precisely.

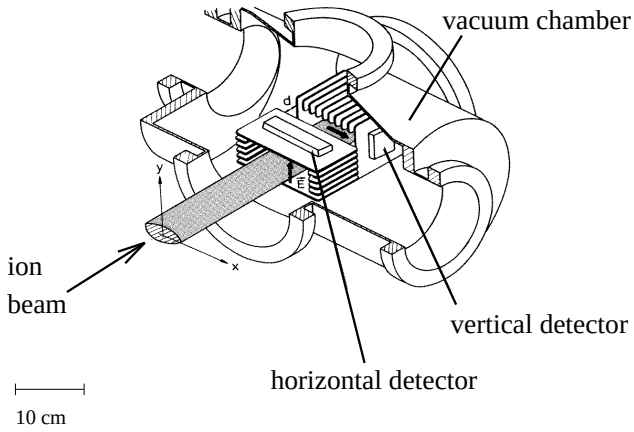

Figure 3.7: *The Beam Profile Monitor*

As the ion beam in the present experiment is sufficiently slow ($\beta = 0.064$), we can assume $\gamma \approx 1$. In this case, the Gaussian velocity distribution leads to a Gaussian distribution of the fluorescence and the relative momentum width $\Delta p/p$ is obtained from the relative width $\Delta\nu/\nu$ of the fluorescence signal via:

$$\frac{\Delta p}{p} = \frac{1-\beta}{\beta}\frac{\Delta\nu}{\nu}. \tag{3.15}$$

Beam Profile Monitor

The horizontal and vertical emittance of the ion beam can be determined with the beam profile monitor (BPM) [Hochadel, 1994], which is shown in figure 3.7. Two pairs of parallel metal plates provide homogeneous electric fields of $|\vec{E}| = 60\ \mathrm{kV/m}$ in the horizontal and vertical direction. Rest gas atoms, that are ionized by the ion beam, are accelerated towards the negative capacitor plates, where a position sensitive microchannel plate detector (MCP) measures a projected image of the density distribution of the ion beam at that location. Due to the thermal energy of the rest gas atoms their position is smeared out when travelling towards the detector leading to a limited spatial resolution, that can be described by a Gaussian distribution of width σ_{res} reflecting the thermal distribution of the rest gas ions. The measured spatial distribuion is, therefore, a convolution of the (Gaussian) resolution function of width σ_{res} with the density distribution of the ion beam. Since the latter is also almost Gaussian (of width σ_{ion}), the actual beam size can be calculated as $\sigma^2_{\mathrm{ion}} = \sigma^2_{\mathrm{meas}} - \sigma^2_{\mathrm{res}}$, where σ_{meas} is the width of the measured distribution. The resolutions, as estimated in [Beutelspacher, 2000], are

$$\sigma_{\mathrm{x,res}} \simeq \sigma_{\mathrm{y,res}} \simeq (250 \pm\ 50)\ \mu\mathrm{m}. \tag{3.16}$$

Since the transverse beam profiles are described by a Gaussian distribution, the standard deviations $\sigma_{\mathrm{x,y}}$ are usually used to define the emittance. According to equation 3.6 we get the emittances from the beam widths $\sigma_{\mathrm{x,y}}$ and the beta functions $\beta_{\mathrm{x,y}}$ at the position of the BPM s_{BPM}

$$\epsilon_{\mathrm{x,y}} = \frac{\sigma^2_{\mathrm{x,y}}(s_{\mathrm{BPM}})}{\beta_{\mathrm{x,y}}(s_{\mathrm{BPM}})}. \tag{3.17}$$

In addition to the beam profile measurement, the BPM provides the integral count rate, which serves as a measure for the number of ions stored in the sorage ring.

3.3 The Laser Setup

3.3.1 Optical frequency standards

Precision spectroscopy requires optical reference standards, which frequencies to be measured can be referred to. These reference frequencies are generated by frequency-stabilized lasers, which have been developed at a variety of frequencies ranging from the near ultraviolet to the infrared. Table 3.1 shows the standards as recommended by the *Comité International des Poids et Mesures* (CIPM) [CIPM, 1997]. Such an optical frequency standard can be provided by the radiation of a single-frequency laser with low frequency noise, interacting with an ensemble of atoms, ions or molecules, that possess absorption lines with a high quality factor $Q = \delta\nu/\nu$ and a weak dependence of their transition frequency on external fields and collisions. The absorption profile taken by tuning[2] the laser frequency across the resonance can be transformed into an error signal by various methods and then be used to stabilize the laser to the center of the absorption line. The frequency of such a stabilized laser has to be determined by comparison with the primary time and frequency standard, the Cs atomic clock. This has been done for the radiations listed in table 3.1. Especially since the invention of widely tunable single-frequency lasers such as dye lasers, diode lasers and optical parametric oscillators practically any suitable absorption line in the optical spectrum can be selected and serve as a frequency reference for the corresponding application. In our experiment the two laser freuencies ν_{p} and ν_{a} parallel and antiparallel to the ion beam have to be calibrated. Both frequency references are realized by lasers stabilized to hyperfine structure transitions of the $X \rightarrow B$ electronic transition of molecular iodine ($^{127}\mathrm{I}_2$), which has a rich spectrum of narrow absorption lines in

[2]The so-called fixed-frequency lasers can also be tuned over a small range.

Table 3.1: *Optical frequency standards as recommended by the CIPM [CIPM, 1997].*

Molecule	Transition	Wavelength (μm)	Rel. Standard Uncertainty
^{1}H	1S-2S	0.2431346246260	8.5×10^{-13}
^{127}I	P(13) 43-0, a_3	0.5146734664	2.5×10^{-10}
^{127}I	R(56) 32-0, a_{10}	0.53224503614	7.0×10^{-11}
^{127}I	R(12) 26-0, a_9	0.5435163331	2.5×10^{-10}
^{127}I	R(47) 9-2, a_7	0.6119707700	3.0×10^{-10}
^{127}I	R(127) 11-5, a_{13}	0.63299139822	2.5×10^{-11}

the visible range. This transition has zero orbital and spin moments in the ground state (X) and zero total moment in the upper state (B). Thus, only a Zeeman effect due to the nuclear magneton is present. Measurements on hyperfine structure components of this transition at 514 nm concerning energy shifts due to transversal [Goncharov et al., 1996] as well as longitudinal [Goncharov et al., 1991] magnetic fields estimated the influence of magnetic fields of 1 G to be of the order of $\Delta\nu/\nu = 10^{-15}$.

As for the parallel light, the ion velocity is adjusted such, that the ions are Doppler-shifted into resonance with an $^{127}I_2$-stabilized fixed-frequency argon ion laser at 515 nm (see table 3.1), described in section 3.3.3. The antiparallel light is provided by a tunable single-frequency dye laser. In the case of Λ-spectroscopy the optical frequency standard is realized by the stabilization of this dye laser to the i-component of the R(99)15-1 transition in $^{127}I_2$, which has been calibrated by comparison with the $^{127}I_2$-stabilized He-Ne laser at 633 nm [Grieser et al., 1994a]. For saturation spectroscopy the a-component of the P(10)14-1 transition is chosen as the reference. Its frequency has been calibrated relative to the i-transition mentioned by means of rf-techniques (see appendix A). The dye laser system is described in section 3.3.4.

3.3.2 Saturation spectroscopy on molecular iodine

As mentioned, both frequency standards needed in the TSR experiment are realised by lasers stabilized to molecular iodine, which has a rich spectrum of narrow absorption lines in the visible range. These components belong to the electronic transition between the B-level and the X-level (ground state). As the iodine molecule is heavy, its velocity at room temperature is comparably low leading only to small collision-induced frequency shifts, which can be conveniently suppressed even further by cooling the iodine absorption cell.

In order to compare a laser with the molecular transition serving as the frequency reference, laser spectroscopy on the molecules has to be performed. For both lasers used in this experiment Doppler-free saturation spectroscopy with a glas cell containing iodine vapor is employed. The setup, which is similar for both lasers, is shown schematically in figure 3.9 (grey panel). Two weak beams serving as a probe beam and a reference beam are split off from the incoming laser beam by a thick beam splitter and guided through a calibrated iodine glas cell provided by the Physikalisch-Technische Bundesanstalt in Braunschweig. The absorption of the beams is measured with photodiodes. By tuning the laser frequency over a resonance the Doppler-broadened absorption profile is recorded. The main part of the incoming laser beam is transmitted by the beam splitter and, in order to saturate the absorption, overlapped with the probe beam antiparallel apart from a small angle of 7 mrad. Due to the opposite direction of the pump and

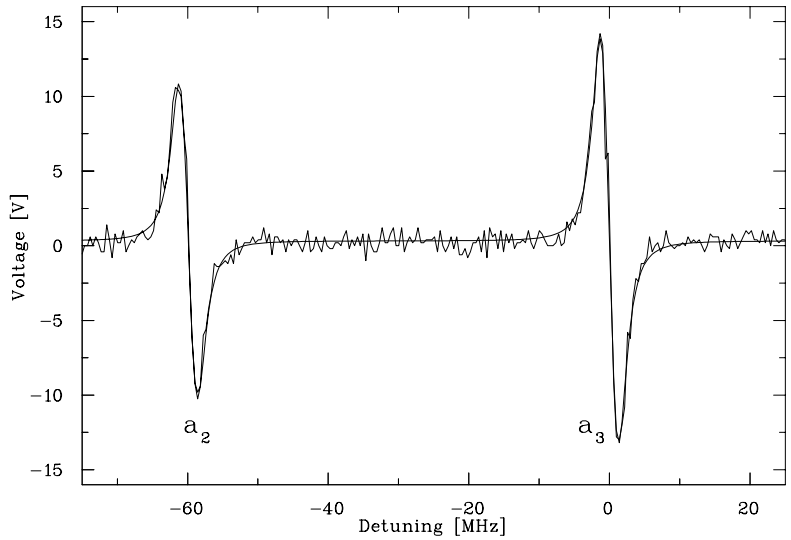

Figure 3.8: *The 1^{st} derivative of the a_2- and a_3-hyperfine structure component of the P(13)43-0 line of iodine taken with the argon ion laser using the lock-in technique described in the text. The a_3-component is used for stabilization of the argon ion laser thus providing a frequency standard as recommended by [CIPM, 1997] (see table 3.1).*

the probe beam the Doppler shift for ions having non-zero velocity goes into opposite directions. These ions, when shifted into resonance with the probe laser, are off-resonant with respect to the pump laser and, therefore, no saturation occurs. Only the ions having zero velocity can be resonant with both lasers simultaneously. Due to saturation the absorption decreases and a Lamb dip occurs at the corresponding frequency. To suppress the Doppler background and to compensate for intensity variations of the laser, the difference signal between the probe beam and the reference beam is observed, so that the saturation dip is isolated.

The lineshape of the Lamb dip is expected to be Lorentzian

$$L(\omega) = L_0 \frac{\gamma_{\mathrm{S}}^2/4}{(\omega - \omega_0)^2 + \gamma_{\mathrm{S}}^2/4} \tag{3.18}$$

with the saturation-broadened FWHM $\gamma_{\mathrm{S}} = \gamma\sqrt{1+S}$. S denotes the saturation parameter. The measurement of this dip is accomplished by the lock-in technique in order to suppress background noise and, in the case of the argon ion laser, to produce an error signal having a zero crossing at the line center, which is then used for stabilization. To this end, the laser frequency ω_{L} is modulated with a sinusoidal of frequency Ω and modulation amplitude ω_{M}:

$$\omega(t) = \omega_{\mathrm{L}} + \omega_{\mathrm{M}} \sin(\Omega t). \tag{3.19}$$

If ω_{M} is small compared to the signal width γ, $L(\omega(t))$ does not change strongly over time and $\omega(t)$ can approximately be regarded as constant. In this case, one can expand $L(\omega(t))$ into a power series around ω_{L}:

$$\begin{aligned} L[\omega(t)] &= \sum_{n=0}^{\infty} \frac{1}{n!} \frac{\mathrm{d}^n L(\omega_{\mathrm{L}})}{\mathrm{d}\omega^n} (\omega_{\mathrm{M}} \sin(\Omega t))^n \\ &= [L(\omega_{\mathrm{L}}) + \frac{\omega_{\mathrm{M}}}{4} \frac{\mathrm{d}^2 L(\omega_{\mathrm{L}})}{\mathrm{d}\omega^2}] \\ &+ [\omega_{\mathrm{M}} \frac{\mathrm{d}L(\omega_{\mathrm{L}})}{\mathrm{d}\omega} + \frac{\omega_{\mathrm{M}}^3}{8} \frac{\mathrm{d}^3 L(\omega_{\mathrm{L}})}{\mathrm{d}\omega^3}] \sin(\Omega t) \\ &- [\frac{\omega_{\mathrm{M}}^2}{4} \frac{\mathrm{d}^2 L(\omega_{\mathrm{L}})}{\mathrm{d}\omega^2}] \cos(2\Omega t) \ldots . \end{aligned} \tag{3.20}$$

When the lock-in amplifier is operated at Ω, the signal reflects the coefficient of the first harmonic

$$L(\omega_{\mathrm{L}}) \propto -\omega_{\mathrm{M}} \frac{\omega_{\mathrm{L}} - \omega_0}{[(\omega_{\mathrm{L}} - \omega_0)^2 + \gamma^2/4]^2}. \tag{3.21}$$

Equation 3.21 is only valid for modulation amplitudes that are small compared to the width of the Lorentzian signal. In general, $L[\omega(t)]$ has to be expanded into a Fourier series:

$$\begin{aligned} L[\omega(t)] &= \frac{A_0}{2} + \sum_{m=1}^{\infty} [A_m \cos(m\Omega t) + B_m \sin(m\Omega t)] \qquad (3.22) \\ A_m &= \frac{2}{\pi} \int_0^{\pi} L(\omega_{\mathrm{L}} + \omega_{\mathrm{M}} \cos\tau) \cos(m\tau) \mathrm{d}\tau \\ B_m &= \frac{1}{2\pi} \int_0^{2\pi} L(\omega_{\mathrm{L}} + \omega_{\mathrm{M}} \cos\tau) \sin(m\tau) \mathrm{d}\tau = 0 \end{aligned}$$

When operated at the modulation frequency Ω, the lock-in signal is proportional to the Fourier component A_1, which can be expressed analytically after [Bayer-Helms and Helmcke, 1977]

$$A_1 = \frac{1}{\delta_{\mathrm{M}}} [(\mathrm{sgn}\delta_{\mathrm{L}}) P_- - \delta_{\mathrm{L}} P_+] \tag{3.23}$$

with the definitions

$$P_{\pm} = \sqrt{\frac{2[\sqrt{(1+\delta_{\mathrm{M}}^2 - \delta_{\mathrm{L}}^2) + 4\delta_{\mathrm{L}}^2} \pm (1 + \delta_{\mathrm{M}}^2 - \delta_{\mathrm{L}}^2)]}{(1+\delta_{\mathrm{M}}^2 - \delta_{\mathrm{L}}^2)^2 + 4\delta_{\mathrm{L}}^2}} \tag{3.24}$$

$$\delta_{\mathrm{L}} = \frac{\omega - \omega_0}{\gamma/2} \tag{3.25}$$

$$\delta_{\mathrm{M}} = \frac{\omega_{\mathrm{M}}}{\gamma/2} \tag{3.26}$$

Figure 3.8 shows the result of a measurement of two hyperfine structure lines taken with the argon ion laser as well as the result of the fit of the first Fourier component.

3.3.3 The I_2-stabilized argon ion laser

The fixed-frequency laser light, overlapped parallel with the ion beam, is generated by an argon ion laser (Lexel 85-1). A built-in prism and temperature-controlled quartz etalon provide single-mode operation at 514.5 nm with a typical output power of 120 mW. Fig 3.9 shows the laser setup, which is described in short in the following. Further details can be found in [Merz, 1991]. After passive stabilization the frequency jitter and, hence, the laser linewidth amounts to about 6 MHz/ms, which makes an active frequency stabilization necessary in order to resolve the hyperfine structure of $^{127}I_2$ (natural linewidth: ≈ 60 kHz). To this end, part of the light is split off by a beam splitter and guided through a confocal Fabry-Perot interferometer (Tec optics, SA300) with a free spectral range[3] of 300 MHz and a finesse[4] of 62.5. The slope of the transmission peak serves as a stable (not absolute) frequency reference. By generating the difference signal between this transmission signal and an attenuable reference beam a zero-crossing is produced on the slope, which determines the lock point of the stabilization. In addition, the subtraction of the reference beam compensates for intensity fluctuations of the laser light. By feedback of the difference signal, which reflects the frequency deviation of the laser from the lock point, to a piezo crystal moving the output coupler, the laser frequency is stabilized to the lock point by controlling the laser cavity length. This method reduces the laser linewidth to $\Delta\nu_{\mathrm{RMS}} = 190$ kHz.

In order to generate a frequency standard, the laser frequency now has to be stabilized to a well-known frequency marker, which is largely independent of external fields and collisions. This marker is provided by the Lamb dip produced by saturation spectroscopy on molecular iodine as decribed in the preceding section. The gain profile of the argon-ion laser coincides with a strong absorption line at 19429.8204 cm^{-1} ($\#4077$ in [Gerstenkorn and Luc, 1978]). The a_3-component of the $B^3\Pi^+_{Ou} \rightarrow X^1\Sigma^+_g$ P(13)43-1 transition is used for stabilization of the laser as recommended by [CIPM, 1997].

Figure 3.9 shows the setup of the saturation spectroscopy. One of the mirrors of the FPI is mounted on a piezo crystal which allows to scan the FPI and, therefore, the argon ion laser over 100 MHz without mode-hops.

In order to use the lock-in technique for the iodine spectroscopy the laser is modulated with a frequency of $\Omega = 29$ kHz and a modulation amplitude of about

[3] free spectral range (FSR): distance between to transmission modes

[4] Finesse $F = FSR/\delta\nu$, where $\delta\nu$ is the width of a transmission peak (FWHM)

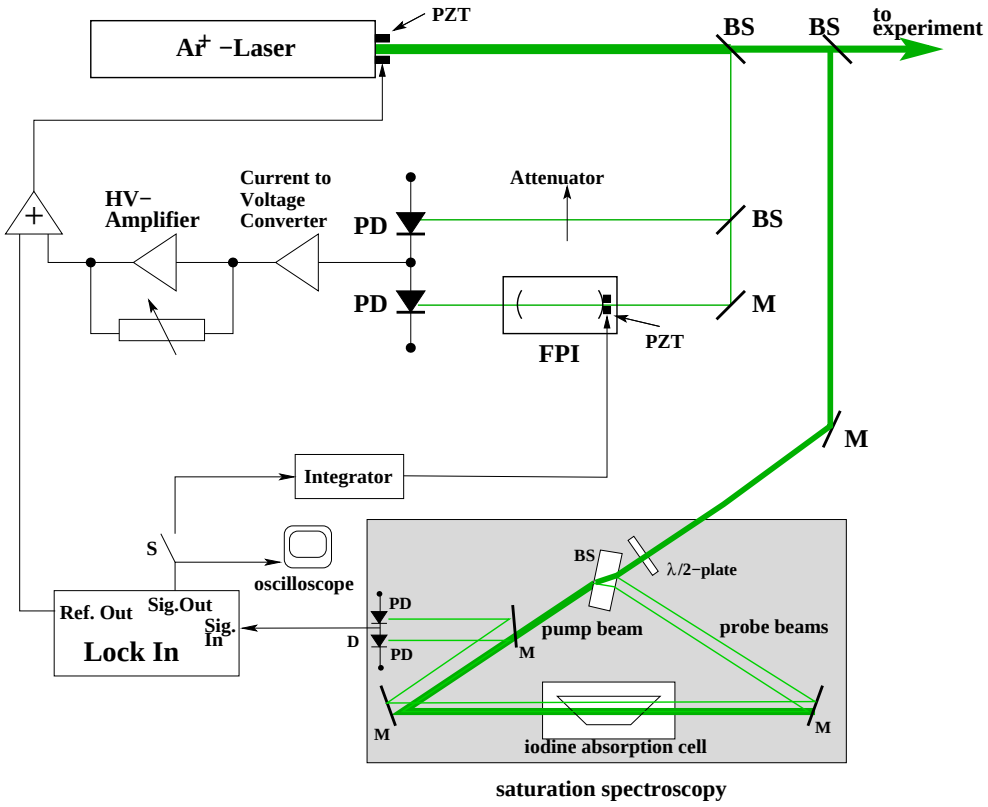

Figure 3.9: *The I_2-stabilized argon ion laser: part of the light is split off by a beamsplittter (BS) and guided through the Fabry-Perot interferometer (FPI). The difference between the transmission signal and a reference beam, which determines the stabilization point and compensates for intensity fluctuations, is fed back to the output coupler of the laser, that is mounted on a piezo crystal (PZT), to reduce the frequency jitter (short term stabilization). Another part of the light is guided to the iodine saturation spectroscopy. By the lock-in technique the iodine absorption profile is transformed into an error signal, that is used to stabilize the FPI to the center of the absorption line (long term stabilization).*

2 MHz by applying a sinusoidal signal to the piezo-driven output coupler of the laser. With this setup typical iodine hyperfine structure signals as shown in figure 3.8 are recorded with help of a lock-in amplifier operated at the first harmonic of the modulation frequency. The zero-crossing of the a_3-component was used to stabilize the reference FPI of the argon laser to the absolute frequency of the a_3-component.

The uncertainty for the argon ion laser frequency is composed of the following contributions (1σ-level):

- Uncertainty of the CIPM-recommendation: < 130 kHz
- Deviation of the temperature of the iodine cell, which was stabilized to $6°$C during the measurements, with respect to the recommended temperature of $-5°$: < 35 kHz
- Uncertainty caused by the residual Doppler background caused by the small angle between probe and saturation beam: < 50 kHz
- Other systematic uncertainties [Spieweck, 1980]: < 5 kHz

In conclusion, the argon ion laser frequency is determined to be

$$\nu_{\mathrm{Ar}} = (582\ 490\ 603\ 370\ \pm\ 144)\ \mathrm{kHz}. \tag{3.27}$$

3.3.4 The dye laser system

Through the choice of the ion velocity achieving resonance with the parallel light of the fixed-frequency argon ion laser, the wavelength of the antiparallel light is also determined. In our case ($\beta = 0.064$) the Doppler shift leads to a wavelength of about 584.5 nm. This light is provided by a commercial tunable single-mode ring dye laser (*Coherent* 699/21) operated with the dye rhodamine 6G and pumped by a frequency-doubled Nd:YAG-laser (*Coherent* Verdi 10) at 532 nm and 6 W.

The essential characteristic of dye lasers is their broad *homogeneous* gain profile, which allows all excited dye molecules to contribute to the laser amplification and, therefore, large output powers at a single frequency using suitable frequency-selective elements. Additionally, the dye laser is tunable over a wide range (typically some ten nm) by properly changing the transmission frequency of the frequency-selective elements.

Figure 3.10 schematically shows the resonator of the CR 699/21 dye laser. The ring resonator setup together with an optical diode provides larger output powers and higher stability compared to standing-wave cavities, because only a unidirectional travelling wave builds up, which doesn't suffer spatial hole burning[5].

[5]Spatial hole burning: the inversion in the laser medium saturated by a standing wave laser

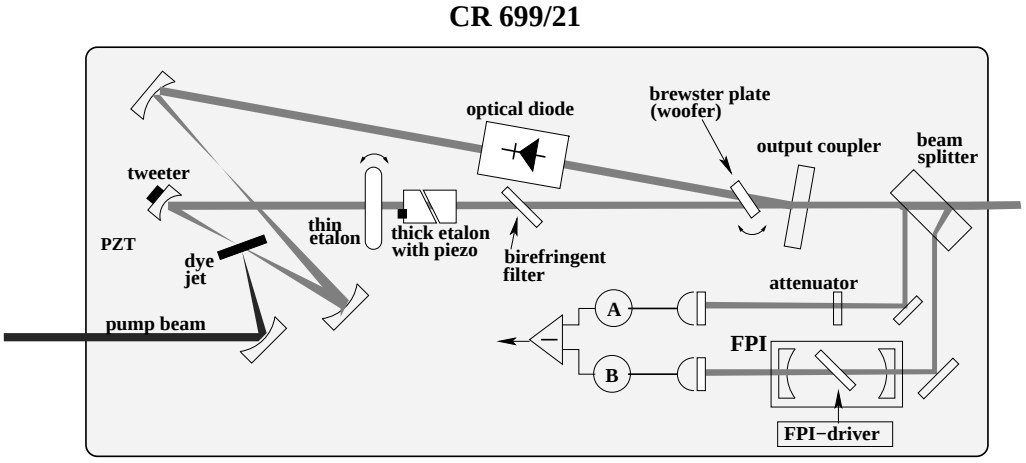

Figure 3.10: *Schematic of the Coherent 699/21 ring dye laser.*

Coarse wavelength tuning is accomplished by a birefringent filter. A further frequency selection by a thin and a thick etalon leads to single-mode operation. This frequency can now be tuned by varying the optical length of the cavity. Slow changes (up to 1 kHz) are achieved by tilting a galvo-driven glas plate (woofer) mounted in the beam path near the brewster angle and providing a tuning range of 30 GHz. Fast frequency changes up to about 70 kHz are done by a small piezo-driven mirror (tweeter). The *Coherent* 699/21 dye laser is equipped with a temperature-stabilized reference cavity for short-term frequency stabilization. The error signal is generated in the same way as for the argon ion laser by the difference between the signal transmitted through the Fabry-Perot interferometer and an attenuable reference signal as shown in figure 3.10. The quality of the dye jet of the commercial laser was improved by replacing the *Coherent* nozzle by a saphire nozzle operated with a dye pressure of 10 bar. Additionally, the dye solution was cooled to 16 °C. These passive stabilization measures reduced the laser linewidth to below 1 MHz, which allows for the resolution of hyperfine structure components of transitions in molecular iodine serving as an absolute frequency reference. The setup for the saturation spectroscopy is the same as for the argon ion laser. The dye laser is modulated with a frequency of $\Omega = 36$ kHz and a modulation amplitude of about 2 MHz by applying a corresponding sinusoidal voltage to the piezo-driven laser mirror (tweeter). The iodine cell temperature was set to

mode experiences a spatial modulation according to the longitudinal intensity distribution of the standing wave. Small fluctuations of the cavity length by only one wavelength shift the maxima and nodes into regions of different gain relations leading to significant intensity fluctuations.

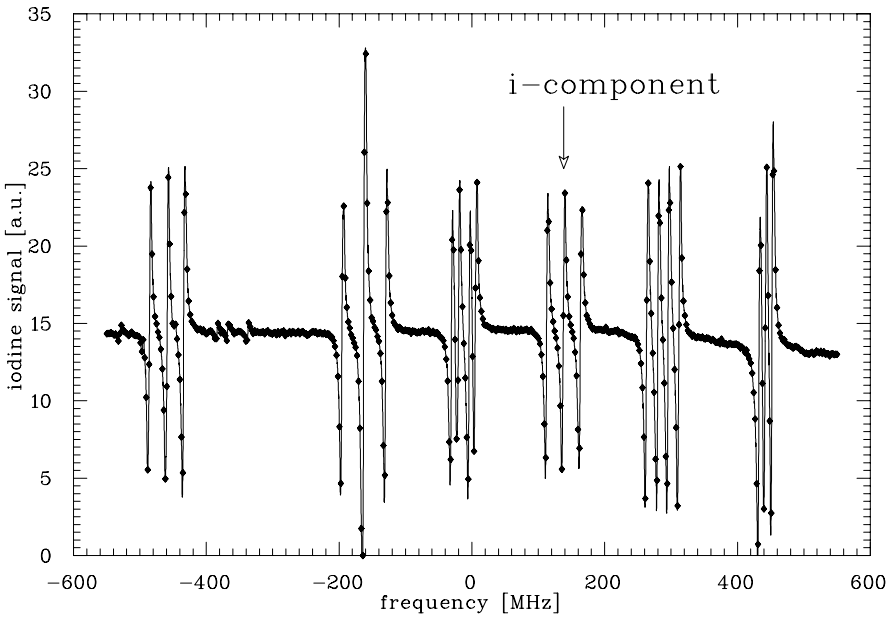

Figure 3.11: $^{127}I_2$ *hyperfine structure components of the R(99)15-1 transition. The indicated i-component has been calibrated by comparison with the iodine-stabilized He-Ne laser at 633 nm with a Michelson interferometer [Grieser et al., 1994a]. It lies about 29 MHz away from the* Λ*-resonance in the TSR experiment at* $\beta = 0.064$ *and is, therefore, chosen as a frequency reference for the dye laser in* Λ*-spectroscopy.*

6 ± 0.3°C. The iodine lines chosen as a reference are shown in the overview scans in figures 3.11 and 3.12. For Λ-spectroscopy the i-component of the R(99)15-1 transition has been calibrated by Grieser et al. [Grieser et al., 1994a] to be:

$$\nu_{\mathrm{i-comp}} = (512\ 667\ 622\ 777\ \pm\ 67)\ \mathrm{kHz} \tag{3.28}$$

at 6°C. For the saturation spectroscopy on $^7Li^+$, which has first been performed in this work, we chose the a-component of the P(10)14-1 transition, which is about 3405 MHz away from the i-component. We measured the hitherto uncalibrated frequency by comparison with the i-component using rf-techniques [Reinhardt, 2003]. A short description of the measurement is given in appendix A. The result of this frequency calibration is:

$$\nu_{\mathrm{a-comp}} = (512\ 671\ 028\ 023\ \pm\ 152)\ \mathrm{kHz}. \tag{3.29}$$

In contrast to the argon ion laser, the dye laser is not stabilized to the iodine line but scanned across the $^7Li^+$ resonance by typically 200 MHz. In order to accomplish the absolute frequency calibration the iodine signal is recorded at the

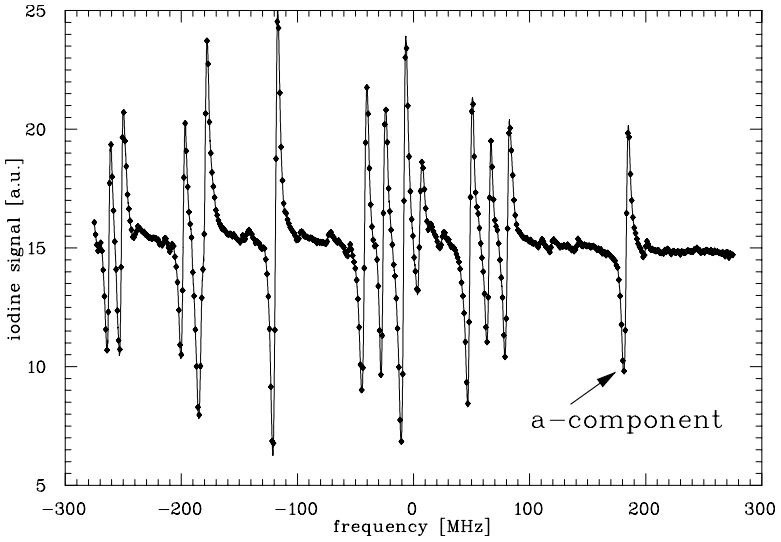

Figure 3.12: *Overview scan over some hyperfine structure components belonging partly to the R(15)14-1 transition and the P(10)14-1 transition in $^{127}I_2$. The a-component of the P(10)14-1 transition labelled in the spectrum is about 66 MHz away from the Lamb dip measured in the TSR-experiment at $\beta = 0.064$ and is used for the frequency determination in the saturation spectroscopy on $^7Li^+$. Its frequency has been determined by comparison with the i-component of the R(99)15-1 transition used in the Λ-spectroscopy.*

same time and fitted as described in section 3.3.2. The corresponding fit error and the uncertainty of the iodine reference line mainly determine the absolute frequency uncertainty as is discussed in chapter 5. The scanning method makes a relative frequency calibration necessary in addition, which is described in the next section.

3.3.5 The acousto-optic modulator as a frequency shifter

In previous experiments at TSR [Grieser, 1994] the relative frequency calibration was accomplished by recording the transmission peaks of a Fabry-Perot interferometer with a free spectral range of 606.8(1.9) MHz. Between two transmission peaks the frequency was determined by linear interpolation, which led to an error of 1.9 MHz [Grieser, 1994] for the determination of the free spectral range due to nonlinearities of the dye laser scan. The accuracy of the relative frequency determination of the dye laser decreases with increasing distance of the laser frequency from the calibrated molecular transition. In the old Λ-type experiment

this accuracy was limited to 125 kHz for a distance of the Λ-resonance from the i-component of the R(99)15-1 transition in $^{127}I_2$ of about 29 MHz. In contrast, the Lamb dip measured by saturation spectroscopy of the $(F = 5/2) \rightarrow (F = 7/2)$ transition is 66 MHz away from the a-component of the P(10)14-1 transition used for the calibration. In order to avoid the corresponding large uncertainty of at least 250 kHz we implemented acousto-optic modulators to shift the frequency of the laser beam sent to TSR with respect to the beam guided to the iodine spectroscopy. These devices are desribed in the following.

An acousto-optic modulator as shown in figure 3.13 consists of a crystal with a piezo fixed on one surface. By application of an rf-signal the piezo excites a travelling sound wave of the applied radio frequency Ω in the crystal. This wave leads to a corresponding modulated strain field, which is coupled to the optical index of refraction by the photoelastic effect [Yariv and Yeh, 1983]. A monochromatic plane light wave of wavelength λ incident at an angle θ with respect to the plane sound wavefronts will be reflected and refracted due to the change of the refractive index. Constructive interference in reflection occurs, when the well-known Bragg condition $m\lambda = 2 \cdot n \cdot d \sin\theta_B$ is satisfied, where m is an integer, n is the refractive index and d denotes the wavelength of the acoustic wave. As d is related to the acoustic frequency Ω by $d \cdot \Omega = v$, where v is the speed of the sound wave, also the Bragg angle θ_B is frequency-dependent. Up to now the wavefronts have been considered to be stationary. However, the reflection of light with frequency ω by moving wavefronts leads to a Doppler frequency shift given by

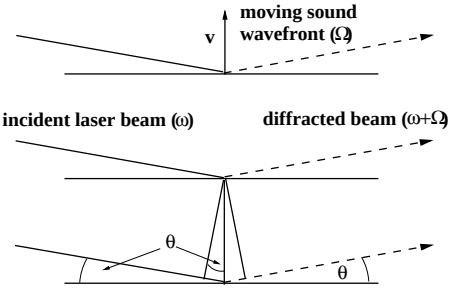

$$\Delta\omega = 2\omega \frac{v_{\parallel}}{c/n}, \tag{3.30}$$

where $v_{\parallel} = v \sin\theta$ is the projection of the velocity of the wavefront on the light propagation direction. Using the Bragg condition for $\sin\theta$, we obtain

$$\Delta\omega = \frac{2\pi v}{d} = \Omega. \tag{3.31}$$

The frequency of the deflected light is, therefore, upshifted by exactly the sound wave frequency Ω. If the direction of propagation of the sound wave is reversed, the Doppler shift changes sign and the frequency of the deflected light is shifted down. This Doppler frequency shift reflects the conservation of energy and momentum, when the interaction of light and sound is interpreted as photon-phonon interaction.

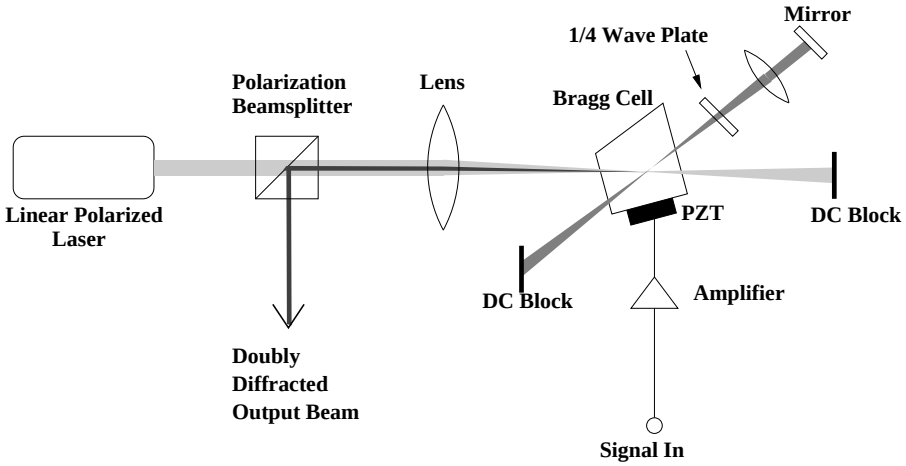

Figure 3.13: *Double-pass setup of an acousto-optic modulator.*

In our experiment acousto-optic modulators are used to shift the frequencies both of the argon ion laser and the dye laser beam going into TSR with respect to the beams sent into the iodine spectroscopies, respectively. Both AOMs are setup in a double-pass arrangement as depicted in figure 3.13. The incoming linearly polarized light is transmitted by a polarization beamsplitter and focussed into the AOM. The deflected upshifted (or downshifted) beam then passes a quarter wave plate resulting in circular polarization and is collimated by a lens placed one focal length away from the focus. In this way the parallel beam can be reflected by a flat mirror to be refocussed into the AOM again. The beam experiences a second frequency shift in the same direction as the incoming beam, whereas the deflection angles of the two passages through the AOM cancel. Due to the reflection from the flat mirror the handedness of the circular polarization changes, so that after passing the quarter wave plate the light is polarized linearly and *perpendicularly* to the incoming beam. Thus, it is reflected by the polarization beam splitter and, therefore, separated from the incoming beam. This double-pass setup makes the angular displacement of the deflected laser beam largely independent of the radio frequency. This allows quick changes of the frequency shifts without the necessity of realignment of the optical elements following the AOM.

In addition, the acousto-optic modulators can shift the laser beams by twice its center frequency. Since broadband frequency shifters as employed in this experiment can be operated in a range of about 20% around the center frequency, also the tuning range is doubled in the double-pass arrangement.

The use of acousto-optic modulators provides another great advantage for our experiment. The radio frequency driving the AOMs and, therefore, the deflected laser beam going into the experiment, can be switched on and off with switching

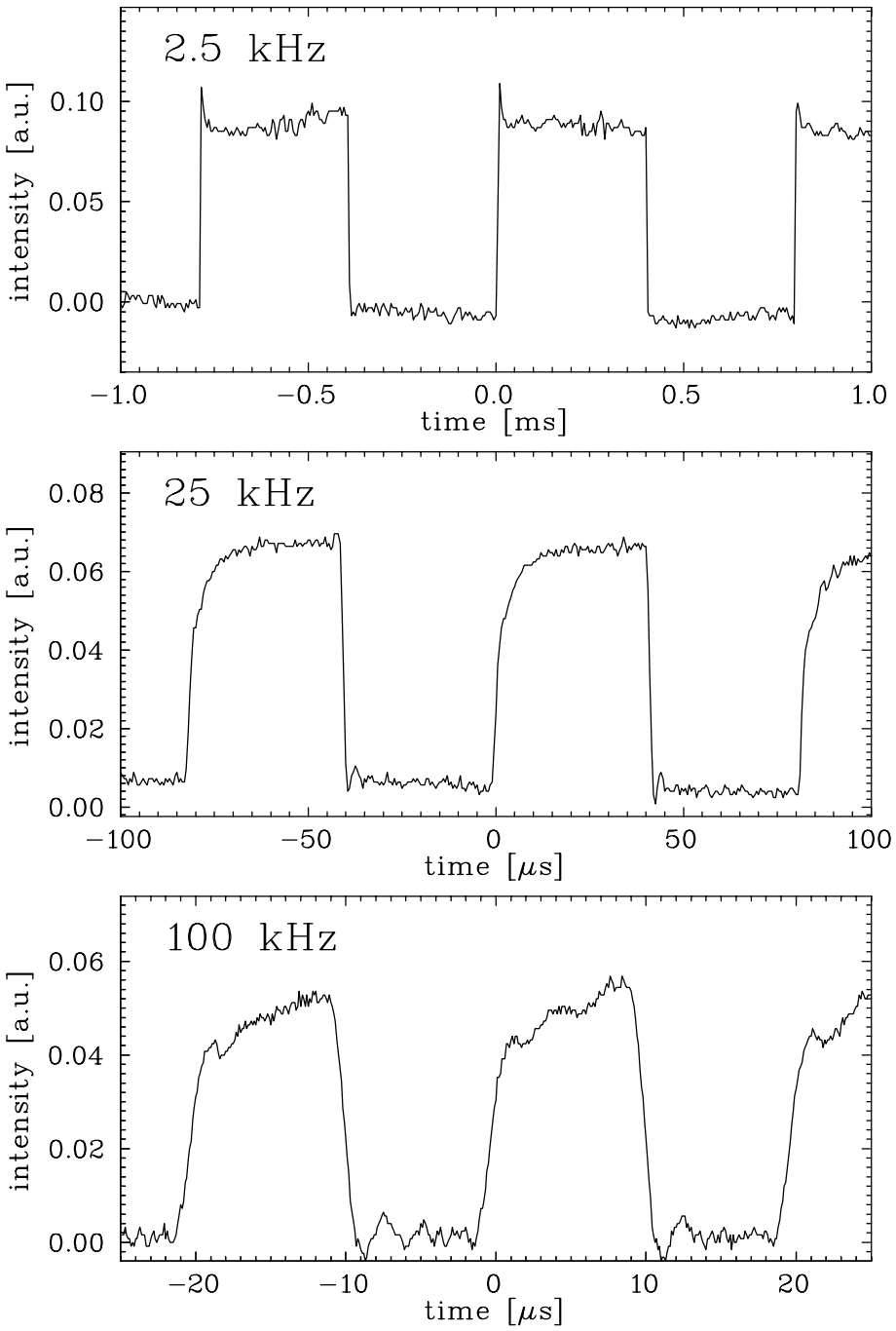

Figure 3.14: *Laser intensity of the switched dye laser beam sent into TSR versus time for three different switching frequencies (2.5 kHz, 25 kHz and 100 kHz). The rise time to reach 90% of the maximum intensity is about 7 μs.*

frequencies up to a hundred kHz by means of rf-switches (*Mini-Circuits* GaAs high isolation switches ZASW-50DR). This has been used to measure the Doppler background in the saturation spectroscopy by recording the fluorescence into four different scalers for different time windows, where the lasers are switched on simultaneously (1), separately (2,3) and switched off (4), respectively. To this end, both lasers have to be switchable, so that we installed frequency shifters in both the dye laser beam and the argon ion laser beam. Figure 3.14 shows the result of a test of the rf-switches. The dye laser power is measured behind the fibre, that guides the light to TSR, with a fast photodiode for three switching frequencies. The rise time to reach 90% of the maximum rf-power turned out to be of the order of 7 μs.

3.4 Laser beam alignment

The resonance condition $\nu_p \nu_a = \nu_0^2$ (equation 2.15) is only valid for exactly parallel and antiparallel alignment of the lasers with respect to the ion beam, respectively. The angle between the two lasers as well as between the lasers and the ion beam have to be properly adjusted. Due to the noisy environment (acoustic vibrations, magnetic fields) it is not possible to run single frequency cw-lasers with the required stability directly at TSR. Therefore, the laser setup is situated in a laser hut in the basement of the TSR hall, about 20 meters away from TSR. The argon ion laser and dye laser beams are merged with a dichroic mirror and then guided to TSR through a single-mode polarization maintaining fibre (see figure 3.16). The usage of a fibre for the beam transport has several advantages. First, the Gaussian shape of the laser beams is strongly distorted after passing several optical elements in the laser hut. The fibre here acts as a spatial filter and provides the required Gaussian beams with low wavefront distortions. Second, when guided to TSR through the air unavoidable small movements of mirrors in the laser hut would translate into large fluctuations of the laser beam position at TSR due to the large distance of 20 m. The fibre output coupler is placed directly in front of the TSR entrance window downstream the ion beam. In order to adjust the Rayleigh range and the position of the focus the bichromatic laser beam is guided through a telescope consisting of a microscope objective ($10\times$) and an achromatic lens ($f = 600$ mm). To establish overlap with the ion beam the horizontal and vertical position as well as the corresponding angles have to be adjustable. This is accomplished by two translation and two rotation stages, which are driven by computer-controllable stepper motors. These devices have an accuracy of $1.2\ \mu m$ and $12.3\ \mu rad$, respectively. The (bichromatic) laser beam is directed through the experimental section of TSR antiparallel to the ion beam. Due to the large Doppler shifts the parallel argon laser beam is far from resonance with the $^7Li^+$ ion. To provide the antiparallel laser light the argon ion laser beam is reflected back by a dichroic mirror, which is also mounted on a $\theta - \phi$ rotation stage with stepper motors. For mode-matching with the antiparallel dye laser beam the argon laser beam is focussed onto the (flat) dichroic mirror. To minimize the laser-laser angle a movable aperture is centered around the bichromatic beam just in front of the entrance window. The argon laser can then be reflected back through this aperture to an accuracy of ± 0.5 mm ensuring an almost perfect anti-parallelism of the two laser beams (see also section 4.1).

In order to optimize the laser-ion overlap the argon ion laser is switched off and the dye laser is tuned into resonance with the two-level system of the $^7Li^+$ ions for the center velocity class. With the stepper motors the laser beam can be displaced parallel in the horizontal as well as the vertical direction. The fluorescence is now recorded as a function of the transverse position of the laser by

three photomulipliers situated at different positions along the experimental section (see figure 3.16). For each position measurement new ions are injected into TSR. After five seconds of electron cooling the fluorescence rate is measured for 2 seconds. Figure 3.15 shows the result of a scan in horizontal direction. The upper graph shows the recorded fluorescence rate. Since the ion current can vary strongly for different injections, as can be seen in the middle graph, the fluorescence is normalized to the BPM-rate, which reflects the number of stored ions[6]. Each photomultiplier[7] measures the convolution of the transverse laser profile and the ion beam profile both having a Gaussian shape. The normalized curves (lower graph) show this Gaussian shape. The compensation for fluctuating ion currents works very well, as can be seen from the data point for position zero. In general the maxima of the fluorescence curves measured at different photomultipliers are at different transverse positions because of angular misalignment of the laser with respect to the ion beam. From the measured distances of these positions and the known longitudinal distance between the photomutipliers one can calculate this angle and correct it with the $\theta - \phi$ rotation stage. With another motor scan the achieved overlap is checked and documented.

In addition to the control of the overlap, the motor-scans provide information about the transverse laser beam profile. Since both the laser and the ion beam profile have a Gaussian shape, the dye laser beam width can be determined as $\sigma_{\mathrm{Dye}} = \sqrt{\sigma^2_{\mathrm{meas}} - \sigma^2_{\mathrm{ion}}}$. This procedure can also be done with the argon ion laser in order to determine its beam width.

[6]Each data point is taken during the same time interval after injection, so that the BPM count rate reflects not only the total number of ions but also the metastable part as the lifetime of the metastable beam is about 11 s, i.e long compared to the measuring time of 2 s.

[7]The measurement in figure 3.15 has been taken before the third photomultiplier was installed.

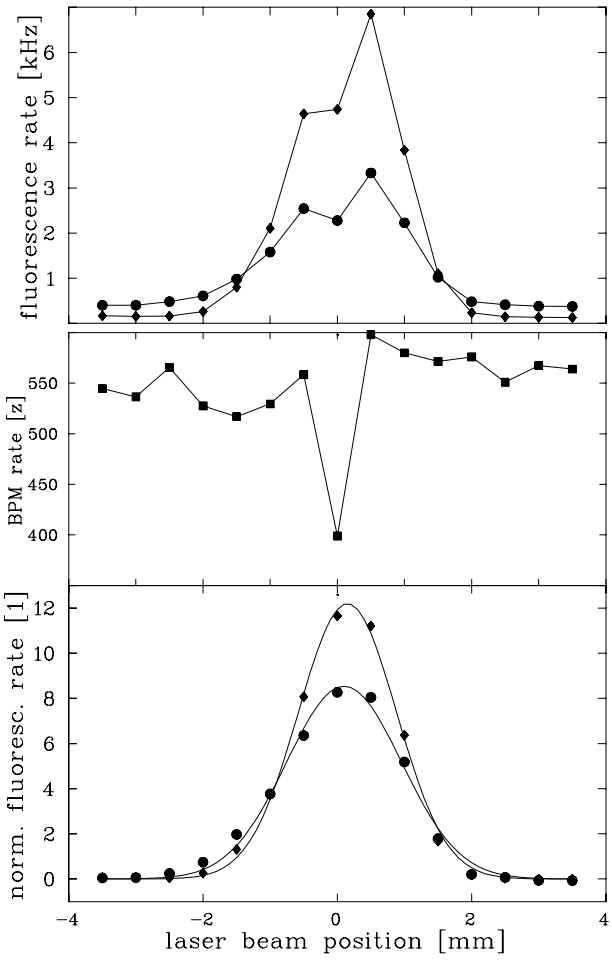

Figure 3.15: *Result of a horizontal motor scan. The upper picture shows the fluorescence taken with two photomulipliers (◇PMT1 ●PMT2) at different positions along the experimental section as a function of the motor position. In the middle picture the BPM rate reflecting the ion current is depicted. In the lower picture the fluorescence, normalized to the BPM rate is shown. The normalization yields a good compensation for the ion current fluctuations.*

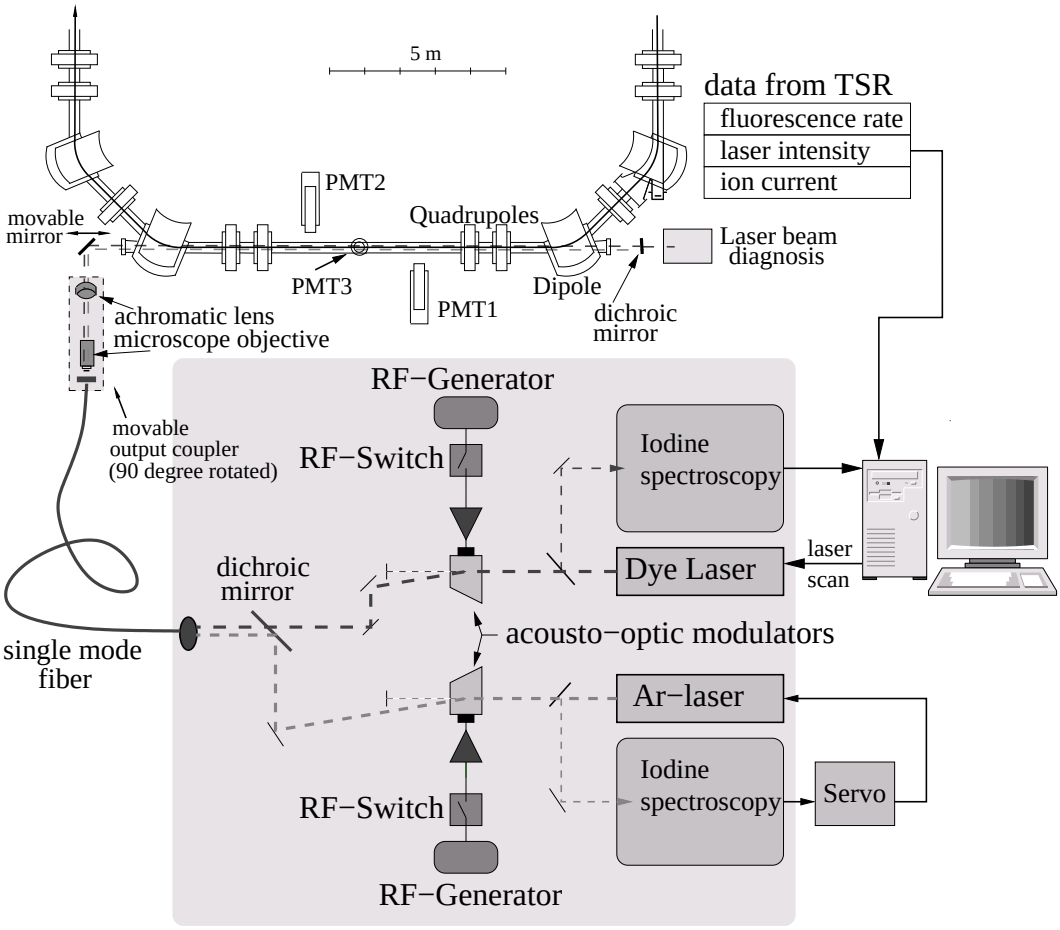

Figure 3.16: *Overview of the experimental setup. Both lasers pass acousto-optic modulators. These are drawn here in a single-pass arrangement for simplicity, wheras in the experiment a double-pass-setup is used as described in the text. The laser beams are overlapped with a dichroic mirror, transmitting the dye laser light (585 mm) and reflecting the argon laser light (514 nm), and then sent to TSR through a polarization maintaining single-mode optical fibre. At TSR the fibre is plugged into a movable output coupler containing a (achromatic) microscope objective and an achromatic lens used for collimation. The collimated bichromatic beam is reflected by a mirror and guided through the beam tube of the experimental section of TSR. The output coupler is sketched rotated into the plane of drawing by 90 degrees. It can be moved perpendicularly to the ion beam tube providing a parallel displacement of the laser.*

Chapter 4

Systematic errors

4.1 Angle-misalignment

To gain insight into the effects caused by some misalignment of the lasers and the ion beam with respect to each other we first restrict ourselves to the ideal case of plane light waves and a beam of parallel ions without any divergence.

Assuming Special Relativity to be valid, the frequency relation $\nu_\mathrm{a} = \nu_1\nu_2/\nu_\mathrm{p}$ is only true, if both lasers are collinear to the motion of the ion, where the Doppler formula 2.5 leads to the two relations $\nu_1 = \nu_\mathrm{a}\gamma(1+\beta)$ and $\nu_2 = \nu_\mathrm{p}\gamma(1-\beta)$. However for slightly misaligned laser beams the resonance conditions read

$$\nu_1 = \nu'_\mathrm{a}\gamma(1-\beta\cos\vartheta_a) \tag{4.1}$$

$$\nu_2 = \nu'_\mathrm{p}\gamma(1-\beta\cos\vartheta_p), \tag{4.2}$$

where ϑ_a and ϑ_p are the angles between the ion beam and the respective laser beams, respectively, measured in the laboratory frame. Using $\vartheta_\mathrm{a} = 180^\circ - \theta$ and $\vartheta_\mathrm{p} = \phi$, multiplication of the two equations leads to

$$\nu'_\mathrm{a} = \frac{\nu_1\nu_2}{\nu'_\mathrm{p}}\frac{1}{\gamma^2(1+\beta\cos\theta)(1-\beta\cos\phi)} \tag{4.3}$$

Using the relation $\nu_1\nu_2 = \nu_\mathrm{a}\nu_\mathrm{p}$ for exactly aligned lasers as well as the fact, that the parallel laser frequency is fixed ($\nu_\mathrm{p} = \nu'_\mathrm{p}$), we obtain for the frequency shift $\Delta\nu_\mathrm{a} = \nu'_\mathrm{a} - \nu_\mathrm{a}$ caused by some misalignment of the lasers

$$\frac{\nu'_\mathrm{a}}{\nu_\mathrm{a}} = \frac{1}{\gamma^2(1+\beta\cos\theta)(1-\beta\cos\phi)} - 1 \tag{4.4}$$

We consider two special cases, as shown in figure 4.1: first, both lasers are assumed to be perfectly antiparallel but have a small angle $\phi = \theta \ll 1$ with

respect to the ion beam (laser-ion beam misalignment) and, second, one laser is assumed to be aligned correctly ($\theta = 0$), whereas the other one is misaligned by $\phi \neq 0$ (laser-laser beam misalignment).

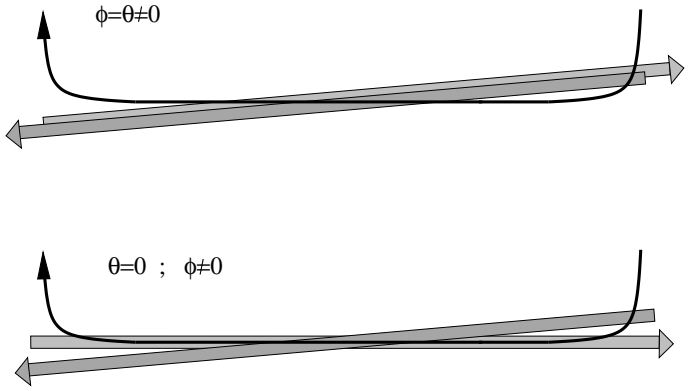

Figure 4.1: *Considered laser-ion angle misalignment (upper picture) and laser-laser angle misalignment (lower picture).*

Assuming ($\phi = \theta \neq 0$) the relative frequency shift is given by

$$\frac{\Delta\nu_{\mathrm{a}}}{\nu_{\mathrm{a}}} = \frac{1-\beta^2}{1-\beta^2\cos^2\theta} - 1. \tag{4.5}$$

For small ion velocities β (in our case $\beta = 0.064$) and for small angles, 4.5 can be approximated by

$$\frac{\Delta\nu_{\mathrm{a}}}{\nu_{\mathrm{a}}} = -\theta^2\beta^2. \tag{4.6}$$

Assuming ($\theta = 0, \phi \neq 0$) the relative frequency shift is

$$\frac{\Delta\nu_{\mathrm{a}}}{\nu_{\mathrm{a}}} = \frac{1-\beta^2}{(1+\beta)(1-\beta\cos\phi)} - 1, \tag{4.7}$$

which can again be expanded for small angles to give

$$\frac{\Delta\nu_{\mathrm{a}}}{\nu_{\mathrm{a}}} = -\frac{1}{2}\frac{\beta\phi^2}{1-\beta}. \tag{4.8}$$

4.2 Ion beam divergence

In addition to misaligned laser beams one has to take into account the divergence of the ion beam, i.e. the distribution of angles of the ions with respect to the central orbit. Figure 4.2 shows the influence of a divergence of 2.5 mrad, which

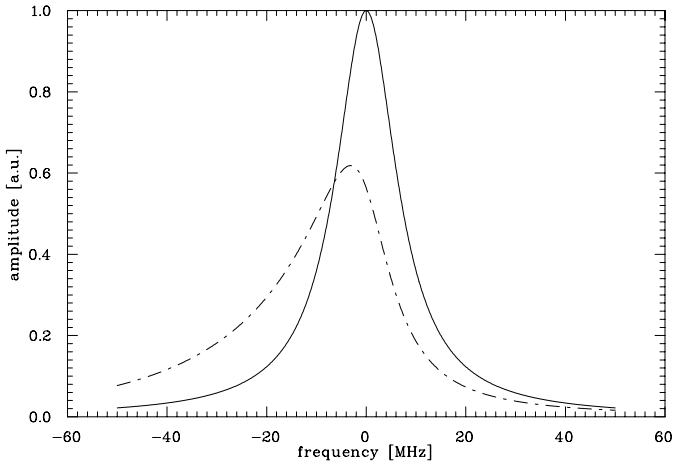

Figure 4.2: *The solid line is a Lorentzian lineshape with a width (FWHM) of 15 MHz for an ion beam with no divergence. The dash-dotted line shows the same signal calculated for an ion beam with a divergence of 2.5 mrad.*

is a typical value for an uncooled ion beam in the experimental section of the TSR. A monoenergetic ion beam with a Gaussian distribution of the angles with the beam divergence as standard deviation has been assumed. Due to its angle with respect to the direction of propagation of the plane laser waves, each ion of the considered ensemble contributes a Lorentzian shifted to lower frequencies according to equation 4.6. The Lorentzians for all ions are summed up leading to the resonance depicted in figure 4.2, that is not only shifted by some MHz, but also shows an asymmetry.

Figure 4.3 shows the calculation of the frequency shift of a Lorentzian resonance with a linewidth of 15 MHz and 60 MHz, respectively, as a function of the ion beam divergence. For different divergences the lineshape as shown in figure 4.2 is calculated and fitted with a Lorentzian. It turns out, that a homogeneous broadening of the resonance, e.g. as caused by saturation broadening, is accompanied by an increased frequency shift.

A typical divergence of an uncooled beam of about 2.5 mrad shifts the center frequency of the resonance significantly by 6 MHz for a signal width of 15 MHz and by 9.5 MHz for a signal width of 60 MHz. The electron-cooled ion beam has instead a divergence of 50 μrad. The corresponding frequency shift is below 100 kHz and, therefore, negligible.

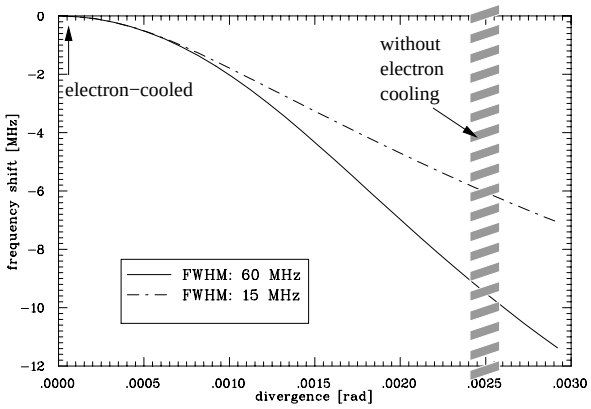

Figure 4.3: *Frequency shift of the line center of a Lorentzian resonance as a function of ion beam divergence for signal widths of 60 MHz and 15 MHz. The shadowed region depicts the divergence of a $^7Li^+$ beam without electron cooling of 2.5 mrad. The arrow indicates the divergence of 50 μrad as measured for the cooled beam.*

4.3 Curvature effects caused by Gaussian laser beams

Up to now we only considered the lasers as plane waves. However, the real laser beams, which are to a good approximation monochromatic, show slight deviations from plane waves and can be described in the vicinity of the optical axis z by the paraxial wave equation [Siegman, 1986]

$$\frac{\partial^2\Psi}{\partial x^2} + \frac{\partial^2\Psi}{\partial y^2} - 2i \cdot k_{\mathrm{L}} \cdot \frac{\partial\Psi}{\partial z} = 0, \tag{4.9}$$

where $\Psi(x, y, z)$ describes the modification to a monochromatic plane wave propagating in the z-direction

$$E(x, y, z, t) = \Psi(x, y, z) \cdot e^{-ik_{\mathrm{L}}z} \cdot e^{i2\pi\nu_{\mathrm{L}}t}. \tag{4.10}$$

A solution to this equation is given by the *Gaussian Beam* with $r^2 = x^2 + y^2$

$$\Psi(x, y, z) = \frac{w_0}{w(z)} e^{i\xi(z)} \cdot e^{-ikr^2/(2R(z))} \cdot e^{-r^2/w^2} \tag{4.11}$$

with the *radius of curvature* $R(z)$, the *beam radius* $w(z)$ and a *phase deviation* $\xi(z)$ from the plane wave:

$$R(z) \;=\; z + \frac{z_{\mathrm{R}}^2}{z} \tag{4.12}$$

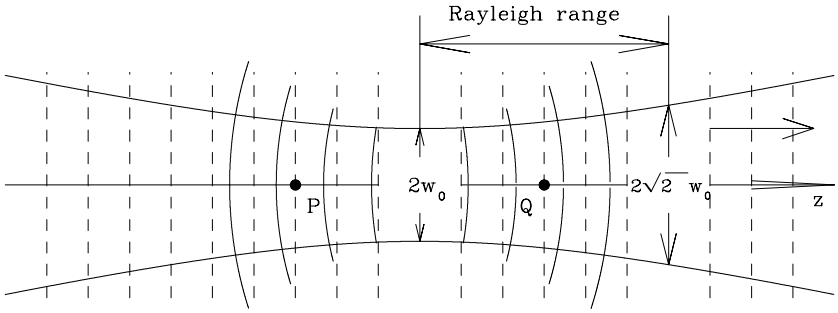

Figure 4.4: *Longitudinal intensity profile of a Gaussian beam. The corresponding wavefronts of a plane wave of the same frequency are depicted by the dashed lines.*

$$w(z) = w_0 \cdot \sqrt{1 + \left(\frac{z}{z_\mathrm{R}}\right)^2} \tag{4.13}$$

$$\xi(z) = \arctan \frac{z}{z_\mathrm{R}} \tag{4.14}$$

$$z_\mathrm{R} = \frac{\pi w_0^2}{\lambda} = \frac{1}{2} k_\mathrm{L} w_0^2. \tag{4.15}$$

The field pattern of the Gaussian beam is characterized entirely by the wavelength λ and either the *beam waist* w_0 or the *Rayleigh range* z_R.

The paraxial wave equation is considered to be valid for optical beams, which converge or diverge by angles of up to 30° [Siegman, 1986]. For typical values of $w_0 = 1$ mm and $\lambda = 500$ nm we find $z_\mathrm{R} = 6$ m.

Figure 4.4 shows a sketch of such a Gaussian beam. The longitudinal coordinate z is defined to be zero at the beam focus, positive in the direction of a divergent beam and negative in the direction of a convergent beam. For a laser travelling from negative to positive z we consider two cases. In point P ($z < 0$) the laser beam is convergent. Here, the phase front of the Gaussian beam is delayed compared to that of the plane wave (dashed lines). The phase deviation is negative. In contrast, in point Q ($z > 0$) in the divergent part the Gaussian wavefront is advanced with respect to the plane wave leading to a positive phase deviation.

To investigate the influence of the Gaussian beam shape on the frequency experienced by an ion in detail, we consider the total phase of the Gaussian beam 4.10:

$$\begin{aligned} \varphi(r,z) &= 2\pi\nu_\mathrm{L} t - k_\mathrm{L} z + \xi(z) - \frac{k_\mathrm{L} r^2}{2R(z)} \\ &= 2\pi\nu_\mathrm{L} t - k_\mathrm{L} z + \arctan(\frac{z}{z_\mathrm{R}}) - \frac{k_\mathrm{L} r^2}{2} \frac{z}{z^2 + z_\mathrm{R}^2} \end{aligned} \tag{4.16}$$

The third term describes a z-dependent and the fourth term a r-dependent phase deviation as compared to the plane wave. The frequency ν' experienced by the ion of velocity $v = \beta \cdot c$ is determined, up to first order terms in β, by the total derivative of the phase with respect to time, $2\pi\nu' = \mathrm{d}\varphi/\mathrm{d}t$. Due to the movement of the ion, the parameters z and, if the ion is moving at a (small) angle[1] ϕ with respect to the light ($k \| z$), also r become time-dependent. The total time derivative then becomes a convective derivative

$$\nu' = \frac{1}{2\pi}\frac{\mathrm{d}\varphi}{\mathrm{d}t} = \frac{1}{2\pi}\Big(\frac{\partial\varphi}{\partial t} + \frac{\partial\varphi}{\partial z}\frac{\partial z}{\partial t} + \frac{\partial\varphi}{\partial r}\frac{\partial r}{\partial t}\Big). \tag{4.17}$$

Assuming the particle to pass through the focal point, i.e. $z = 0$, $r = 0$, we find

$$\begin{aligned} \frac{\partial z}{\partial t} &= v\cos\phi \approx v(1 - \phi^2/2) \\ \frac{\partial r}{\partial t} &= \pm v\sin\phi \approx \pm v\phi \end{aligned} \tag{4.18}$$

with the - sign for $z < 0$ and the + sign for $z > 0$. Using $k_\mathrm{L} = 2\pi\nu_\mathrm{L}/c$ we get

$$\begin{aligned} \nu' = \nu_\mathrm{L}(1-\beta)\Big[&\frac{r|z|}{z^2 + z_\mathrm{R}^2}\phi + (1 - \frac{\phi^2}{2})\Big(1 - \frac{w_0^2}{2}\frac{1}{z^2 + z_\mathrm{R}^2} \\ &- \frac{r^2}{2}\frac{z^2 - z_\mathrm{R}^2}{(z^2 + z_\mathrm{R}^2)^2}\Big)\Big] \end{aligned} \tag{4.19}$$

For $|z| \gg 0$ and/or $z_\mathrm{R} \gg 0$ equation 4.19 reduces to the first order Doppler shift formula for a laser beam parallel to the ion movement and a slight angular misalignment ϕ. Note, however, that these conditions are difficult to fulfill since z_R is of the order of 3 m, as will be seen in the next chapter. Moreover, even for a perfect aligned ion beam ($\phi = 0$) there remains an additional velocity proportional frequency shift when compared to a plane wave.

Considering a laser beam travelling in the z-direction, i.e. antiparallel to the ion beam, the resulting frequency in the rest system of the ion is given by the analogous formula to equation 4.19 with $-\beta$ replaced by β and ϕ by $-\theta$.

In conclusion, moving ions pass regions of different phases of the Gaussian beam , which causes frequency shifts proportional to the ion velocity β and which therefore have to be considered in spectroscopic measurements on fast beams.

[1] Note that $\phi \geq 0$ by definition.

Chapter 5

Results

5.1 Ion beam properties

A major requirement for the feasibility of high resolution spectroscopy is a high ion beam quality. First, the ion beam has to be very narrow and spatially stable in order to guarantee a proper overlap with the lasers. Second, the beam divergence has to be minimized to avoid a frequency shift of the resonance due to an angle between the interacting photons and ions. And third, the ion beam velocity has to be both sufficiently fine adjustable and stable to achieve and keep resonance with the fixed-frequency laser light as well as to minimize shifts due to the AC-Stark effect. In this section the ion beam properties are analyzed and documented.

Figure 3.3 shows the impact of electron cooling on the transverse beam profile. The size shrinks from about 18 mm to a few tenth of a mm within several seconds permitting a very good control of the overlap between laser and ion beam as described in the next section.

Figure 5.1 presents a closer look onto the horizontal and vertical profiles of the ion beam as measured with the beam profile monitor after 5 seconds of electron cooling, revealing a two-component distribution. Two Gaussians are fittet to the data, respectively, accounting for the electron cooled part as well as an uncooled residual component. From the relative areas of the two Gaussians one can extract, that about 15% of the ions belong to the uncooled fraction, which has a width of $\sigma_{\mathrm{unc,x}} = 2.38$ mm and $\sigma_{\mathrm{unc,y}} = 2.64$ mm, respectively. In order to determine the real width of the cooled component one has to take the resolution widths 3.16 into account. We find beam sizes of $\sigma_x = (220 \pm 38)\ \mu$m and $\sigma_y = (239 \pm 36)\ \mu$m at the position of the BPM. The fit errors of the σ_{meas} are negligible compared to the error of the resolution widths.

After equations 3.17 the corresponding horizontal and vertical emittances are $\epsilon_x = 1.05 \times 10^{-8}$ m·rad and $\epsilon_y = 1.81 \times 10^{-8}$ m·rad. From these, together with the

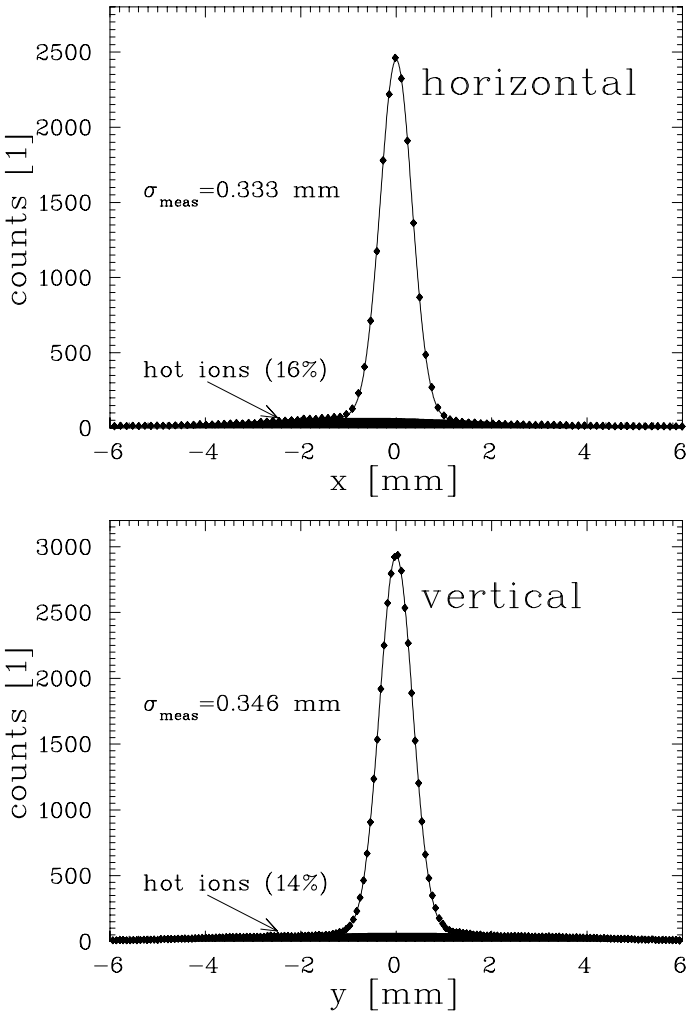

Figure 5.1: *Horizontal and vertical $^7Li^+$ ion beam profile after 5 seconds of electron cooling as measured with the beam profile monitor.*

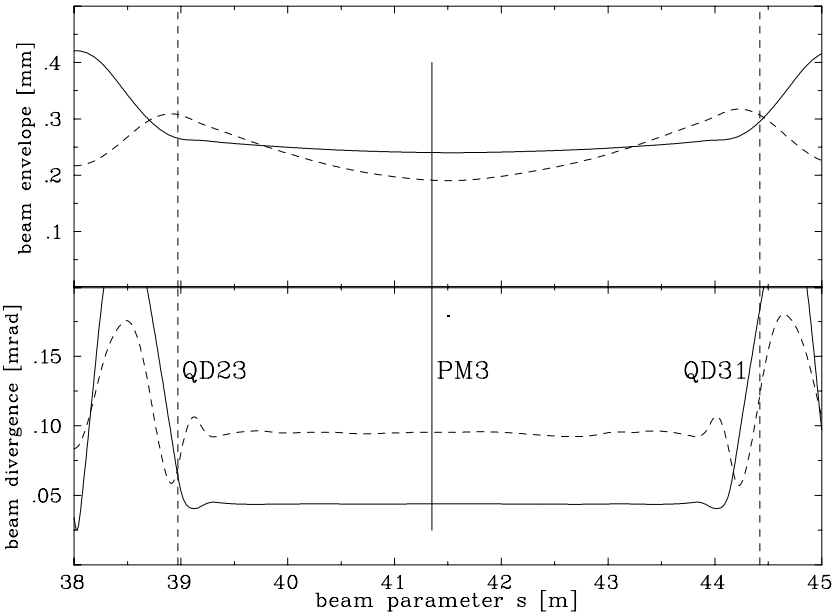

Figure 5.2: *Horizontal (solid line) and vertical (dashed line) profile (upper picture) as well as divergences (lower picture) of the electron-cooled $^7Li^+$ ion beam in the experimental section. The position of the nearest quadrupole magnets and of the photomultiplier is indicated.*

beta function (figure 3.2), one can calculate the ion beam diameters as well as the divergences at any position in the storage ring. Figure 5.2 shows both quantities for the experimental section. In contrast to an uncooled ion beam lineshifts caused by the maximum divergence of about 0.1 mrad of the cooled beam are negligible.

The investigation of the longitudinal velocity distribution can be done via laser-induced fluorescence as described in section 3.2. Figure 5.3 shows the typical result of one laser scan over the $5/2 \rightarrow 7/2$ transition of an electron-cooled ion beam. The fluorescence signal is expected to be a Gaussian distribution modified by the exponentially decreasing ion current. The photomultiplier rate is, therefore, normalized to an exponential curve with the lifetime of the metastable ions as determined below. This normalized rate, reflecting the ion velocity distribution, is shown in figure 5.3. The dye laser is scanned from lower to higher frequencies over 8 GHz. As the dye laser is travelling antiparallel with respect to the ions, the fluorescence at low frequencies comes from fast ions and vice versa. Surprisingly, the spectrum shows strong distortions from the expected Gaussian shape. We found peaks on the left and dips on the right side of the distribution, independently of the scan direction. Further investigation showed no dependence of the peaks and dips on the frequency. In contrast, the features appeared every

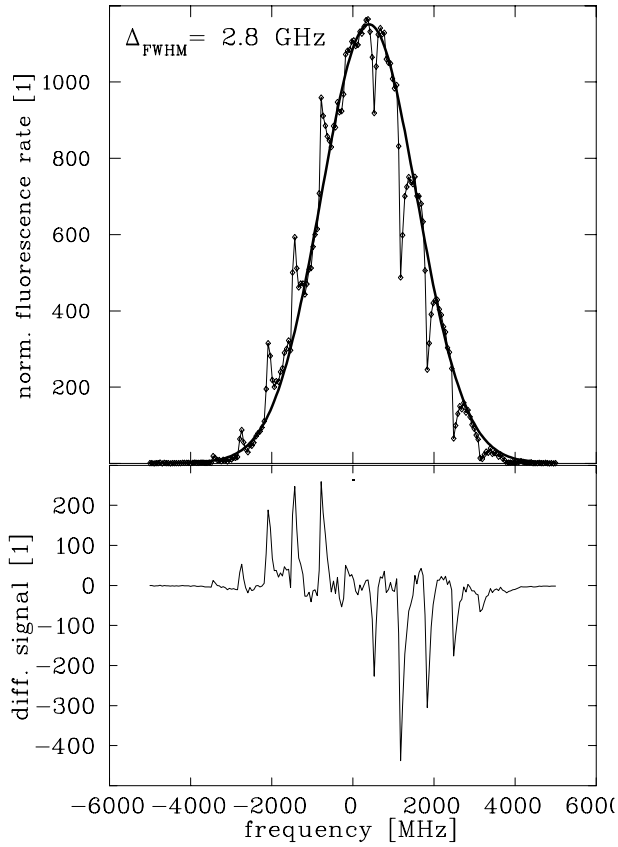

Figure 5.3: *Upper picture: Fluorescence scan across the* $5/2 \rightarrow 7/2$ *resonance, normalized to the ion current. The expected Gaussian profile is modified by peaks on the left and dips on the right side of the resonance, which are caused by a movement of the velocity distribution to higher velocities every 625 ms. Lower picture: Difference between the distorted resonance and the corresponding undistorted Gaussian.*

625 ms, so that one gets more peaks and dips for slower laser scans. The structure can be explained with a movement of the whole ion velocity distribution by about 500 MHz to higher velocities (i.e. to smaller frequencies in the spectrum) and back every 625 ms. This corresponds to a relative momentum deviation of $\Delta p/p = 1.4 \times 10^{-5}$ and does not affect most of the experiments at TSR. In contrast, the saturation spectroscopy as well as the Λ-spectroscopy is performed in a 200 MHz range around the center of the velocity distribution. The ion current can be assumed as constant except for the exponential decay, which is, however, possible to be taken into account, as is described below. The back-and-forth movement of the velocity distribution takes some 100 ms, which is much longer than the measuring time for one data point of a laser scan of 0.02 s. Thus, the corresponding changes in the ion current do not cancel for single data points. This leads to significant decreases in the fluorescence spectrum making the isolation of the Lamb dip or the Λ-resonance impossible in a single scan. Only after many scans the fluorescence fluctuations cancel out. Furthermore, a shifted ion velocity distribution causes a shift of the Lamb dip (or Λ-resonance) through the AC-Stark effect. As the movement always goes to the same direction, also the AC-Stark does so and, therefore, does not cancel out. In order to avoid these problems we

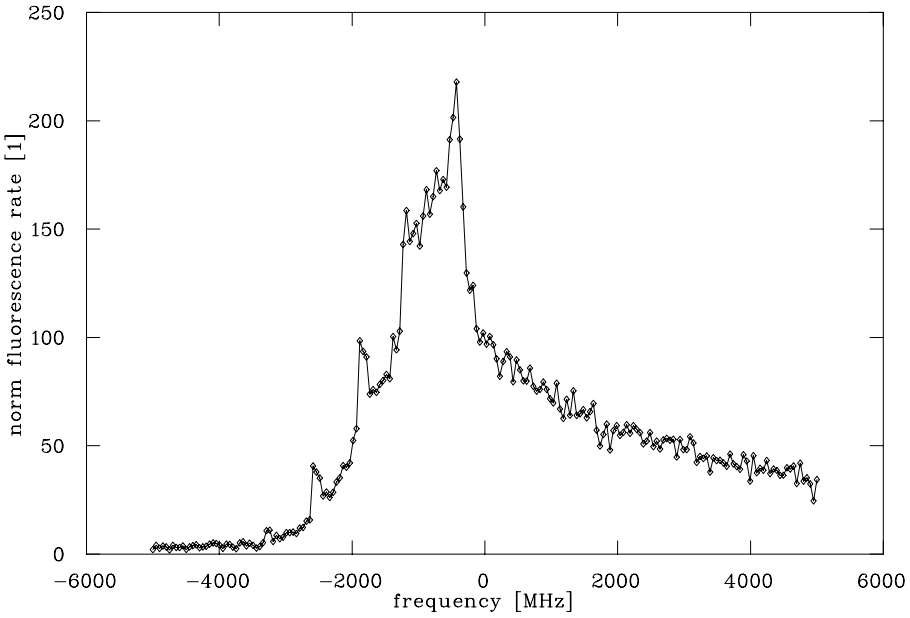

Figure 5.4: *Dye laser scan across the initially electron-cooled velocity distribution. In the middle of the scan the electron cooler is switched off. As a result the distribution becomes broader due to heating processes and the dips, which are caused by the movement of the whole distribution for the electron-cooled beam, disappear.*

first tried to find the reason for this instability. Figure 5.4 shows a single scan with the dye laser across the velocity distribution, whereby the electron cooler is switched off in the middle of the scan. The width of the velocity distribution increases due to heating processes leading to a smaller slope. Nontheless, the ion velocity movements should lead to significant dips here as well, which are not observable. However, we did not find an instability on the 625 ms time scale at the power supplies of the devices of the electron cooler. The fact, that the ion velocity is always shifted in the upward direction makes the following scenario conceivable: Either the ion beam or the electron beam is moving transversally in space. This spatial movement would translate into velocity changes of the ion beam caused by the space charge distribution of the electron beam. The ions, ideally traversing the electron beam in the center, would experience a higher electron velocity when shifted away from the center axis, because the accelerating cathode voltage is less shielded by the outer electrons. According to equation 3.9 the ion beam has to be shifted by ± 0.7 mm in the electron cooler in order to cause a velocity shift corresonding to the observed 500 MHz. After equation 3.8, this shift would amount to a 4 mm shift of the ion beam in the experimental section due to the larger dispersion in this region. This would be observable with the beam profile monitor as well as in the saturation spectroscopy, because the laser-ion overlap would be lost almost completely. However, a movement of the electron beam is also possible.

Since the reason for the shifts of the velocity distribution could not be found, we employed the technique of ion beam bunching, which has already been implemented at TSR for laser cooling experiments [Eisenbarth, 2001]. As already described in section 3.1.2, the ion velocity of a bunched beam is determined by the bunching frequency rather than by the electron cooler. When accelerated by the electron cooler, the ions are reflected by the wells of the bunching potential. They perform synchrotron oscillations of 47 Hz around the central velocity. These oscillations are faster than a laser scan (of the order of the measuring time of one data point), so that the changes of the ion current cancel out. Figure 5.5 shows a single dye laser scan accross the velocity distribution of a bunched beam. The ions are confined in the bunching potential. No changes of the ion current on the time scale of the laser scan, except for the exponential decay, are present. The ion beam bunching also prevents the ion velocity distribution from slow drifts due to changes in the cathode potential, which are typically of the order of 500 to 1000 MHz. This strongly reduces frequency shifts of the Lamb dip or the Λ-resonance due to the AC-Stark effect.

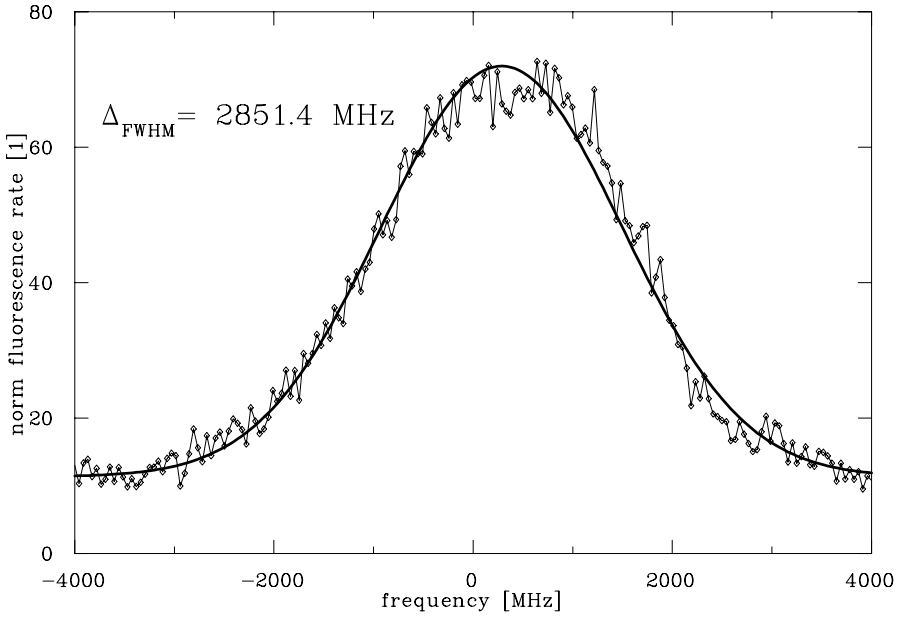

Figure 5.5: *Single fluorescence scan of an electron-cooled and bunched ion beam. No fluctuations on the time scale of the laser scan are observable.*

5.2 Laser-ion beam overlap

After setting up the storage, electron cooling as well as the bunching of the ion beam, the laser beams have to be overlapped. At first, motor-scans as described in chapter 3.4 are performed with the dye laser in the horizontal and vertical direction. Figure 3.15 shows the result of such a scan for the horizontal direction, taken with the dye laser tuned into resonance with the $^3S_1(5/2) \rightarrow ^3P_2(7/2)$ transition in the center of the velocity distribution. For each spatial laser position a new bunch of ions is injected into TSR. After five seconds of electron cooling the fluorescence is measured with the three photomultipliers for two seconds . At the same time the BPM count rate is recorded, providing a measure for the total number of ions stored in TSR for the respective injection. By the normalization of the fluorescence to the BPM rate variations in the fluorescence signal due to different ion currents cancel. The resulting normalized rates reflect a convolution of the Gaussian-shaped laser and ion beam at three photomultipier positions along the experimental section. The measured transverse profiles can, therefore, be fitted with a Gaussian, providing information about the overlap as well as the transverse laser beam radius.

From the three maximum positions one can deduce the trajectory of the ion beam and calculate the angle and the displacement of the laser beam with respect

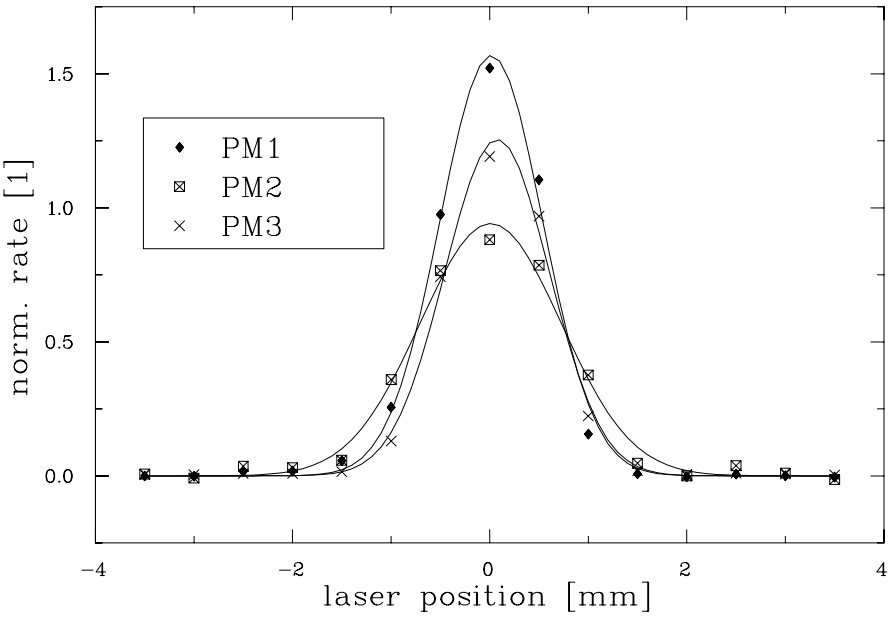

Figure 5.6: *Horizontal motor-scan with the dye laser, which documents the overlap with the ion beam. For the spectroscopy the laser is placed at zero position. From the Gaussian fit the residual angle with respect to the ion beam as well as the laser beam radius is extracted as described in the text.*

to the ion beam. In this way the parallel alignment of the dye laser with respect to the ion beam can be controlled with an accuracy of better than ± 50 μrad in one transverse direction, which corresponds to an overall radial angle uncertainty of ± 70 μrad. In addition, the angle calculated from the profiles measured with photomultiplier 1 and 3 as well as the angle determined between photomultiplier 2 and 3 agree with each other within the fit errors. Thus, no significant bend of the ion beam caused by possible electric or magnetic stray fields in the experimental section was found.

The easiest way to overlap the argon ion laser beam is to place an aperture around the bichromatic laser beam in front of the TSR entrance window after optimizing the dye laser overlap. The argon ion laser is then reflected back by a mirror placed behind the TSR experimental section. It turned out, that the reflected argon laser beam can be centered to the aperture to ± 0.5 mm. Over the distance between the aperure and the reflection mirror of 12 m this results in an error of the laser-laser adjustment of ± 50 μrad in one transverse direction. The overall radial laser-laser angle uncertainty is, therefore, ± 70 μrad.

From the widths of the measured profiles we obtain the transverse dye laser widths at the three positions of the photomultilpliers.

In order to get information about the argon ion laser profile, we also performed

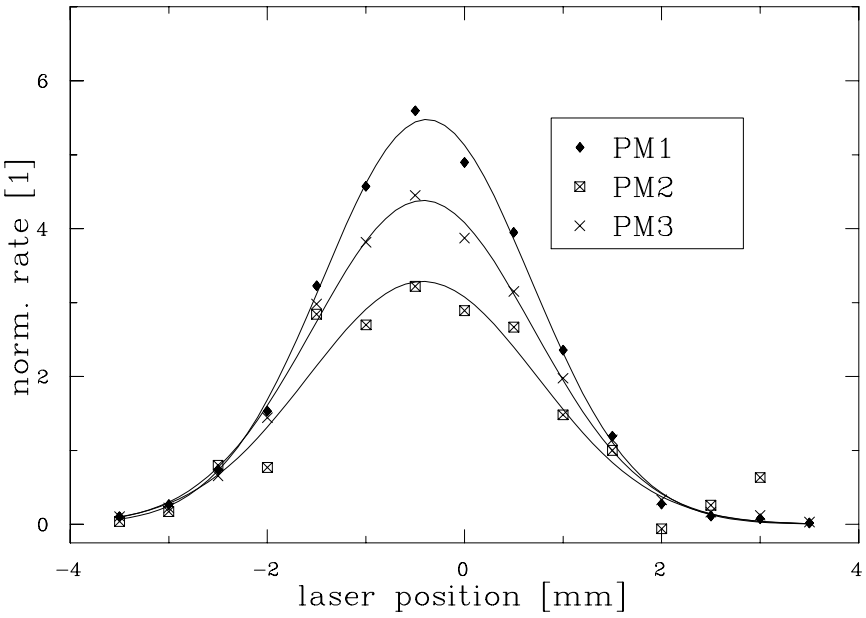

Figure 5.7: *Horizontal motor-scan with the argon ion laser. The fits confirm the good parallelism between laser and ion beam. From the widths one can obtain the longitudinal profile of the Gaussian beam.*

a motor-scan with that laser. As in this case only the reflected beam interacts with the ions, the mirror has to be adjusted very accurately. It turned out, that the parallelism of the incoming and the reflected beam stayed sufficiently stable during the motor-scan leading to reliable data also for the argon laser. The measurement confirms the good overlap of the argon laser with the ion beam and yields information about the beam radius.

In order to mode-match the incoming dye laser and the reflected argon ion laser, ideally, the focus of the bichromatic beam has to be put onto the (flat) mirror. The longitudinal profiles of the laser beam have been measured as described in the following. The width of the fitted Gaussian to the motor-scan data provides the radius of the laser beam at three positions along the beam axis. In order to get the net width from the measured value, one has to take the width of the ion beam into account: $\sigma^2_{\mathrm{laser}} = \sigma^2_{\mathrm{meas}} - \sigma^2_{\mathrm{ion}}$. Two further data points for the radius have been measured outside TSR near the windows with the aid of a razor blade. Figure 5.8 shows the two sets of five data points as a function of the TSR beam parameter. According to the usual definition in laser physics the *beam radius* w is used, which is defined as the $1/e^2$-width (power) and is related to the σ-width by $w = 2\sigma$. Equation 4.13, which reflects the longitudinal profile of a Gaussian laser beam, is fitted to the data points with the Rayleigh range z_{R} and the focal position

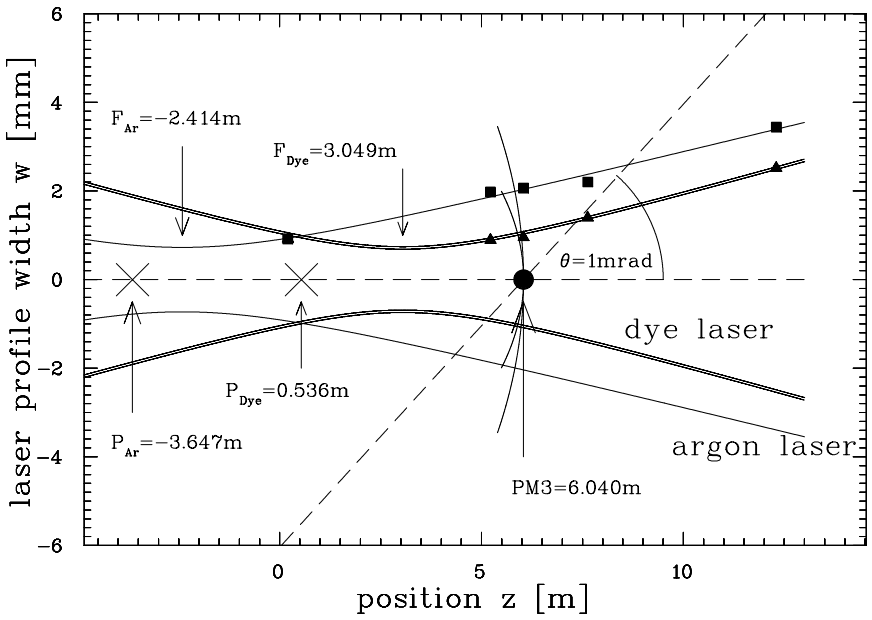

Figure 5.8: *Profile of the Gaussian argon ion laser as well as the dye laser beam in the experimental section. The position of photomultiplier 3 is indicated. The mirror reflecting the argon ion laser beam is located at 0 m and the ion beam travels in the positive z-direction. P_{Dye} and P_{Ar} are the centers of the spherical wavefronts of the lasers at the position of PM3. F_{Dye} and F_{Ar} indicate the foci of the lasers.*

z_0 as fit parameters:

$$w(z) = \sqrt{\frac{\lambda z_{\mathrm{R}}}{\pi}} \cdot \sqrt{1 + \left(\frac{z - z_0}{z_{\mathrm{R}}}\right)^2}. \tag{5.1}$$

The factor $\sqrt{\lambda z_{\mathrm{R}}/\pi}$ is the beam waist w_0. By this fit both Gaussian laser beams are determined completely. For the dye laser we find $z_{\mathrm{R}}^{\mathrm{Dye}} = 2.7$ m corresponding to $w_0^{\mathrm{Dye}} = 0.715$ mm. The focus lies at $z_0^{\mathrm{Dye}} = 3.0$ m, where $z = 0$ m is defined to be at the mirror. Thus photomultiplier 3 is about one Rayleigh range away from the dye laser focus. As for the argon ion laser we find $z_{\mathrm{R}}^{\mathrm{Ar}} = 3.2$ m corresponding to $w_0^{\mathrm{Dye}} = 0.727$ mm and the focus is at $z_0^{\mathrm{Ar}} = -2.4$ m, thus, about 2.6 Rayleigh ranges away from photomultiplier 3. As can be seen from figure 5.8, the position of the focus of the bichromatic incoming beam lies 3 m in front of the mirror. As a result the virtual focus of the reflected argon ion laser lies considerably behind the mirror. The influence of this mismatching of the two laser beams on the spectroscopy, especially as far as the wavefront curvature is concerned, is discussed in chapter 4.

Once the ion laser overlap is optimized, the TSR windows, which are tiltable, are adjusted nearly perpendicularly to the laser beams in order to make the window reflections leave the beam tube through the respective opposite window. In this way, the reflections are prevented from hitting the photomulipliers and, thus, causing straylight background. However, exact perpendicular alignment has to be avoided, because otherwise a standing wave builds up between the windows, which then act as a resonator.

5.3 Lifetime of the metastable ions

The optical transition used in this experiment is part of the metastable spectrum of the $^7Li^+$ ion. A certain fraction of the ions injected into TSR are excited to this metastable state by the stripping process in the tandem accelerator. Its radiative lifetime amounts to 50 seconds in vacuum, but is lowered by stripping due to collisions with rest gas ions as well as electron impact ionization in the electron cooler [Saghiri, 1999]. In order to investigate the time development of the ion beam the dye laser is tuned into resonance with the $^3S_1(5/2) \rightarrow ^3P_2(7/2)$ transition for the ions in the center of the velocity distribution. After five seconds of electron cooling the induced fluorescence, which is proportional to the number of metastable ions, is recorded with time (see upper graph of figure 5.9). From an exponential fit a lifetime of 12.6 s is obtained. As the duration of a typical laser scan described below is in the same order of magnitude (about 5 s), the ion lifetime is sufficiently long to perform spectroscopy, but has to be taken into account in the analysis. The lower graph of figure 5.9 shows the count rate of the beam profile monitor recorded simultaneously with the fluorescence. Due to the two-component composition of the ion ensemble this curve can be fitted with a sum of two exponentials taking the lifetime of the metastable fraction from the fluorescence measurement. This yields the lifetime τ_0 of the ground state component of the ions as well as the relative height at t=0. From the latter an initial fraction of metastable ions of about 10% has been deduced, taking the different cross-sections for rest gas ionization ($\sigma_{\mathrm{meta}} = 1.83 \cdot \sigma_{\mathrm{ground}}$ [Saghiri, 1999]) and, thus, different detection efficiencies into account.

5.4 Saturation Spectroscopy

The ion beam properties as well as the laser beam alignment with respect to the ion beam now allows for high precision spectroscopy. In this section a series of measurements on saturation spectroscopy of the closed two-level system realised by the $^3S_1(5/2) \rightarrow ^3P_2(7/2)$ transition is reported. At first, the procedure of the

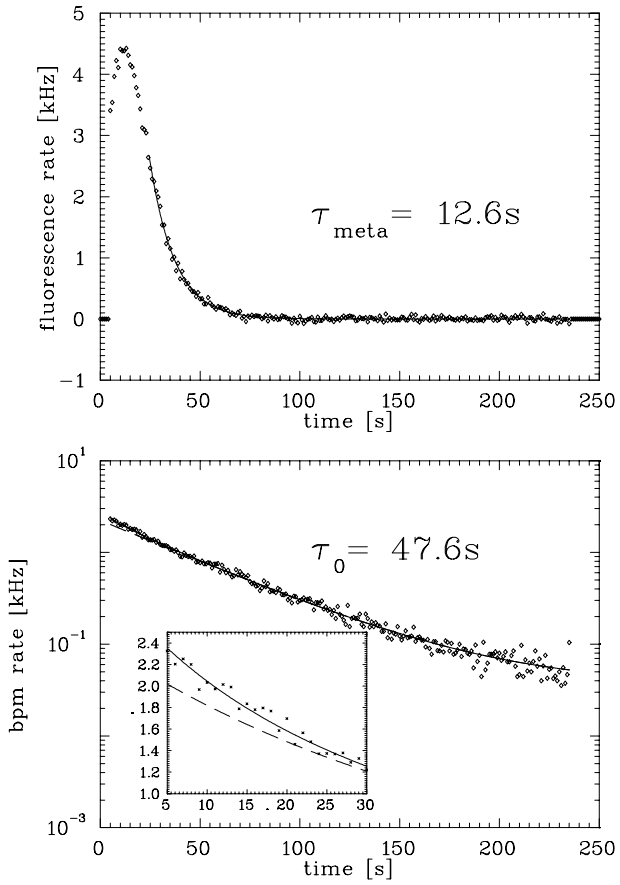

Figure 5.9: *Upper picture: Fluorescence taken with the dye laser tuned into resonance with the center of the ion velocity distribution as a function of time. The fluorescence comes only from the metastable part of the ions. Lower picture: BPM count rate as a function of time. This reflects the total number of ions.*

measurements is described in detail. The second subsection discusses the systematic errors and the third one comprises the results.

5.4.1 Measurement procedure

At first the ion velocity has to be adjusted such, that the argon ion laser is resonant with the ions in the center of the velocity distribution in order to suppress AC-Stark shifts. Figure 5.10 shows a broad dye laser scan (5 GHz) across the whole velocity distribution. The position of the argon laser is clearly visible with the narrow dip. By adjusting the electron cooler voltage as well as the bunching frequency the dip can be centered exactly. Especially the bunching allows for

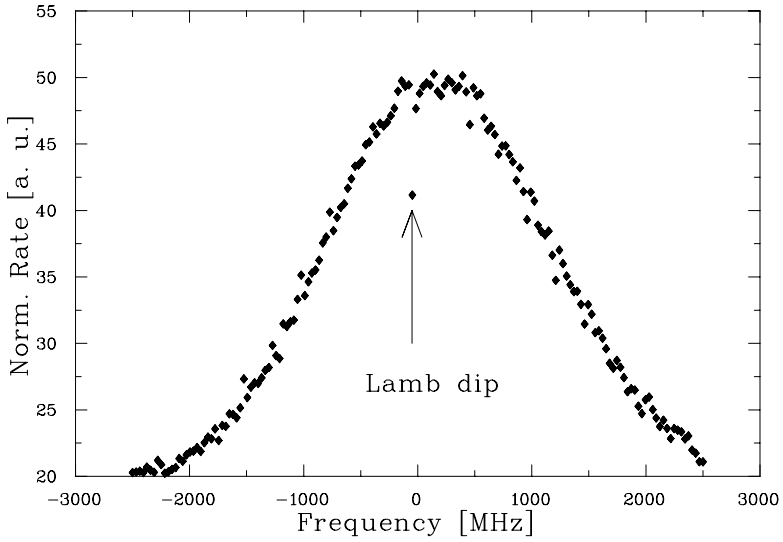

Figure 5.10: *Saturation spectroscopy: The dye laser is scanned across the whole velocity distribution (5 GHz). With help of these broad scans the ion velocity can be adjusted by adjusting the electron cooler voltage as well as the bunching frequency such, that the narrow saturation dip indicated by the arrow lies exactly in the center of the distribution.*

fine-tuning, wheras the cooler voltage is only adjustable in steps of 500 MHz. Furthermore, this adjustment can be done considerably more precisely as compared to Λ-spectroscopy, because the V-resonance used there is much broader (about 1 GHz) [Grieser, 1994].

Figure 5.11 shows a 300 MHz scan over the Lamb dip taken without usage of acousto-optic frequency shifters. Both laser intensities were about 700 μW at a beam radius of about 1-2 mm as shown in figure 5.8. After injection the lasers are blocked for five seconds, until the ion beam reaches its electron-cooled equilibrium state. Then, the dye laser is scanned down from high frequencies to low ones. When the scan is finished, a new bunch of ions is injected and the procedure is repeated. The run shown here contains 67 ion injections. For each scan the iodine line, which is recorded simultaneously, is fitted. The frequency axis of the single scans are then corrected according to the center position of the iodine line. In this way, frequency drifts of the dye laser, which frequently happen between two scans, are compensated for. After this frequency correction the scans are summed up. As the scanning range of about 300 MHz is considerably smaller than the Doppler width of about 3 GHz, the velocity distribution can be regarded as constant over the scan except for the lifetime decay of the ion number. Thus, the spectrum shows the Lamb dip lying on an exponential fluorescence background,

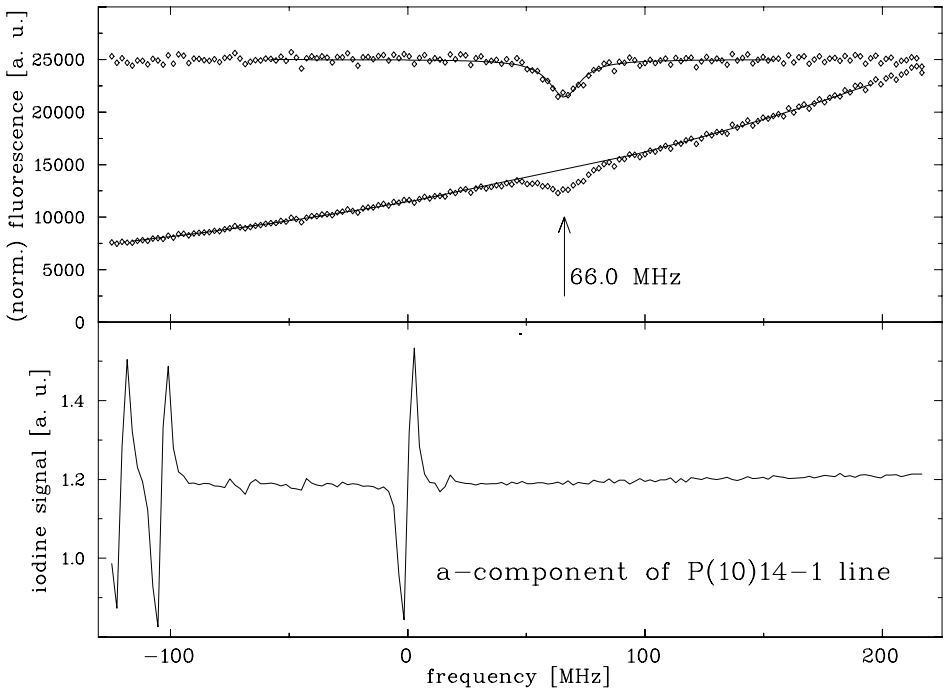

Figure 5.11: *One of the first Lamb dip measurements roughly showing the frequency position with respect to the iodine spectrum. The exponentially decreasing data is subtracted from and then normalized to the fit (solid line, see text). The resulting data (upper curve) has been given an offset for better illustration. It is fittet with a Lorentzian. The Lamb dip shows to be about 66 MHz away from the nearest hyperfine structure line, which is chosen for absolute frequency calibration. The width of the Lamb dip is about 16 MHz and, thus, considerably smaller than that of the* Λ*-resonances measured by [Grieser, 1994] (60 MHz).*

which is fitted with an exponential plus an offset outside the Lamb dip. After subtraction of the data from this fitted curve, it is additionally used to normalize the data to the number of ions. The possibility of this normalization is an essential advantage of saturation spectroscopy compared to Λ-type spectroscopy. The resulting curve (upper curve in figure 5.11), which is given an offset for better illustration, can now be fitted with a Lorentzian function. The width of the Lamb dip showed to be 16 MHz. The narrowest linewidths observed in Λ-spectroscopy by Grieser et al. were of the order of 60 MHz. The lower graph of figure 5.11 shows an iodine signal taken with the dye laser simultaneously in order to determine its frequency. The hyperfine structure line nearest to the Lamb dip is the a-component of the P(10)14-1 line. This line is, therefore, chosen to accomplish the absolute determination of the dye laser frequency. However, the frequency of

this line has not been measured yet. For this reason we determined the frequency with an accuracy sufficient for our purpose by comparison with the i-component of the R(99)15-1 line, which was calibrated in [Grieser et al., 1994a] to serve as the reference for the Λ-resonance [Grieser, 1994]. The rather small distance between these two lines of about 3.4 GHz allows the comparison to be done with rf-techniques using acousto-optic modulators. This measurement is described in appendix A.

The relative frequency calibration is in general accomplished by additional frequency markers, which are recorded simultaneously with the saturation dip. In the experiment by Grieser et al. [Grieser, 1994], for example, an etalon with a free spectral range of about 600 MHz has been used. The calibration of the frequency between two markers is done by interpolation. This requires a high linearity of the dye laser scan. The frequency uncertainty increases with increasing distance from the absolute frequency marker (the iodine line). The Lamb dip of the $5/2 \rightarrow 7/2$ transition is about 66 MHz away from the iodine line, which would lead to a frequency uncertainty of at least 250 kHz (see chapter 3.3.5). To avoid this large error, both laser beams going to TSR are frequency-shifted with acousto-optic modulators of 200 MHz center frequency in a double-pass arrangement, whereas the beams going into the iodine spectroscopy are not[1]. The broadband acousto-optic modulators allow operation within a bandwidth of typically $\pm 20\%$ of the center frequency providing sufficient flexibility in the choice of the frequency shift. Due to the double-pass arrangement both laser beams can be frequency-shifted by 400 $\pm$80 MHz with respect to the iodine spectroscopy. To accomplish the net frequency shift of the Lamb dip with respect to the iodine line of about $\delta\nu \approx 66$ MHz, which is far out of the operating range of the acousto-optic modulators (about 400 ± 80 MHz for the double-pass arrangement), the AOMs have to shift the lasers in opposite directions and, thus, coarsely compensate their shifts except for $\delta\nu$. Due to the opposite directions of the lasers with respect to the moving ions, the frequency shifts $\Delta\nu_{\mathrm{a}}$ and $\Delta\nu_{\mathrm{p}}$ are transformed into the ions rest frame differently. In order to compensate a frequency shift of the argon ion laser of $\Delta\nu_{\mathrm{p}}$, which selects a slightly different velocity class of the ion ensemble, the dye laser has to be shifted by

$$\Delta\nu_{\mathrm{a}} = -\frac{1-\beta}{1+\beta}\Delta\nu_{\mathrm{p}}. \tag{5.2}$$

Therefore, the deviation between the Lamb dip and the iodine line can be adjusted

[1] In principle, it would be sufficient only to shift the dye laser with an AOM of 80 MHz center frequency operated at 66 MHz. However, the AOMs not only serve as frequency shifters, but also as switches for the lasers going into TSR. As our measurement scheme requires both lasers to be switchable, both are provided with AOMs.

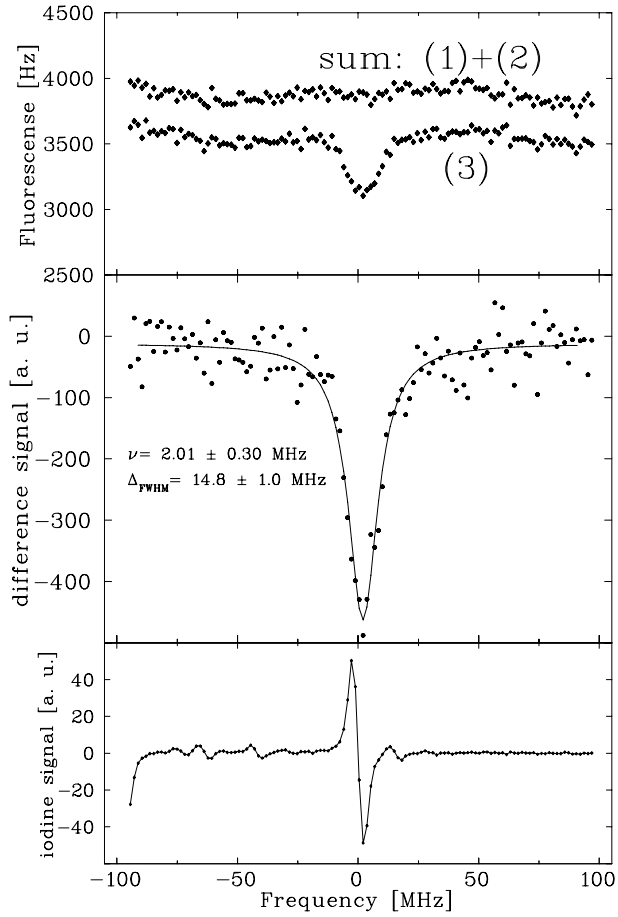

Figure 5.12: *Example for a Lamb dip taken with switched lasers and decoupling of the start of the laser scan from the ion injection. The spectrum consists of 200 data points. Every 46 data points the scan is paused for injecting and electron-cooling of a new ion beam. In this run about 80 scans are taken and summed up after frequency correction according to the line center of the co-recorded iodine line (lower panel), which defines the zero point on the frequency scale. In the upper panel the sum of spectra (1) and (2) taken with the lasers switched on separately, as well as spectrum (3), where both lasers were on at the same time, are depicted. An offest is added to the sum spectrum for clarity. The middle panel shows the difference of both spectra. Fluctuations of the fluorescence background, which are due to residual variations of the ion number, appear in both spectra and mainly cancel in the difference signal.*

as

$$\delta\nu = \Delta\nu_{\mathrm{a}} + \frac{1-\beta}{1+\beta}\Delta\nu_{\mathrm{p}}. \tag{5.3}$$

The values $\Delta\nu_{\mathrm{p}} = -400$ MHz and $\Delta\nu_{\mathrm{a}} = 414$ MHz, chosen in our experiment, lead to $\delta\nu = 62.12$ MHz, which is a coarse estimate to shift the Lamb dip into the vicinity of the iodine line. The remaining frequency deviation is below 5 MHz and the corresponding error in the determination of the dye laser frequency decreases from 250 kHz to about 20 kHz. For the final determination of the Lamb dip position compared to the iodine line, the frequency shifts $\Delta\nu_{\mathrm{a}}$ and $\Delta\nu_{\mathrm{p}}$ have to be taken into account. However, the knowledge of the ion velocity is not necessary, as will be seen later.

Apart from fitting the Doppler background outside the Lamb dip, we employed another method to take the limited lifetime of the metastable ions into account. Both AOMs are switched on and off at frequencies up to 200 kHz (corresponding roughly to the TSR roundtrip time) with help of rf-switches. The chopping pattern shown here[2] is as follows: during one time window (3) both lasers are on and the saturation signal is recorded with a scaler, in two additional windows (1,2) the lasers are switched on separately and the corresponding fluorescence is measured with scalers 1 and 2. In the fourth time window both lasers are off and the photomultiplier dark count rate is recorded. The combined fluorescence of (1) and (2) can be subtracted from (3) in order to isolate the saturation feature, which is only present in (3), from the fluorescence background. In addition, it can also be used to normalize the Lamb dip with respect to the ion current decay in the ring.

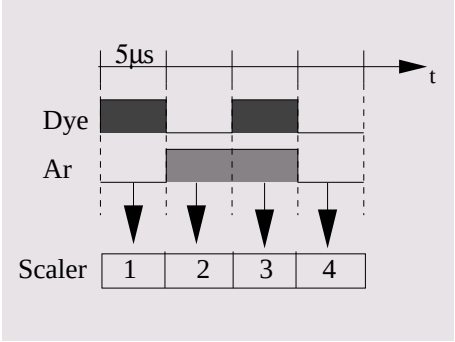

Although, by this method, the dependence of the fluorescence background on the number of ions is taken into account, an influence of the ion number on the Lamb dip frequency, for example by intra beam scattering, is still conceivable, because the ion current is still correlated to the laser frequency. In order to account for this problem, we decoupled the ion injection from the start of the laser scan in order to get spectra with the same mean number of ions at each data point after averaging over many scans. In our scheme only $n = 46$ of the 200 data points of one laser scan are taken at one ion injection. After that the laser scan is paused in order to inject and electron-cool a new bunch of ions, on which the second set of n data points is taken. In this way, after averaging over many laser scans,

[2]Note that the duration of a measuring cycle is always given by $4 \times \nu_{\mathrm{cp}}^{-1}$, where ν_{cp} is the switching frequency.

new ion injections occur at various frequencies in the laser scan and not always at the beginning. Ideally, one data point per injection ($n = 1$) would be desirable, but as electron cooling takes five seconds after each injection, the number of ions taken at one injection should be as large as possible with regard to the duty cycle. Another requirement for the choice of the number n is, that the lowest common multiple (LCM) of n and total number of data points per scan be as large as possible, for the number of data points at which, after $LCM/200$ laser scans, a new bunch of ions is injected, is LCM/n. Our choice of $n = 46$ proves as a good compromise. With $LCM = 4000$ 100 injection are distributed over 100 different frequency positions after averaging over 23 laser scans, leading roughly to a constant ion number over the scan range. Figure 5.12 is a typical example for a scan taken with this method. The upper picture shows the sum of the spectra (1) and (2) (fluorescence background without Lamb dip) as well as spectrum (3) (fluorescence background with Lamb dip). For clarity, the graphs have been given an offset. The remaining fluctuations in the fluorescence background appear in both spectra and, thus, cancel in the difference signal (middle picture).

5.4.2 Systematic errors

Laser intensity dependence

Several effects scaling with the laser intensity are conceivable to influence the frequency of the Lamb dip. E.g. the high photon scattering rate of the Doppler background may lead to local changes in the ion velocity distribution giving rise to AC-Stark shifts. In addition, an increasing laser power would saturate the ions near the central orbit and excite more and more ions in the wings of the transverse ion distribution. Thus, more and more ions from the hot component of the distribution (see figure 5.1) having a larger mean divergence would contribute to the signal. Furthermore, ions excited in the wings of the transverse laser beam profile experience frequency shifts due to the different phase behaviour. In order to investigate this influence, a series of Lamb dips has been recorded with the method described above at different laser powers. Each run contains about 50 laser scans.

In the following, the determination of the laser intensities is described. Before each run the total dye laser power has been set to the desired value. It has been measured behind the TSR exit window with a calibrated power meter. To get the corresponding power, as seen by the ions, one has to transform the measured power into the rest frame of the ions according to:

$$P_{\mathrm{Dye}}^{\mathrm{ion}} = P_{\mathrm{Dye}}^{\mathrm{lab}} \frac{1+\beta}{1-\beta}. \tag{5.4}$$

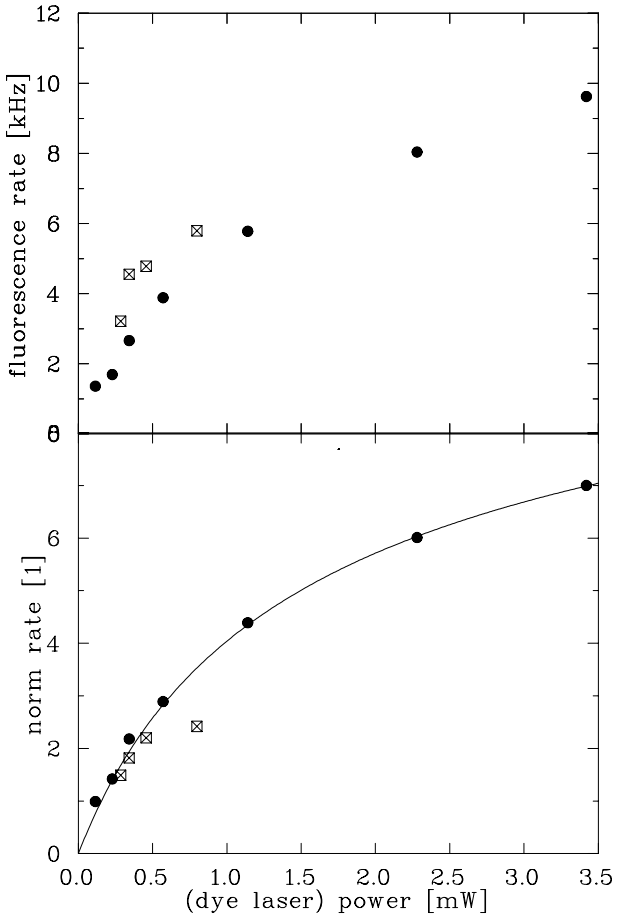

Figure 5.13: *Upper figure: laser-induced fluorescence as a function of dye laser power. The data indicated with squares has been taken at a different ion current than the ones indicated as circles . Lower figure: The same data, now normalized to the BPM rate. The solid line is a fit to the data except for the data point at 0.7 mW.*

To balance the light forces of the two lasers, the *intensities* are desired to be equal. Yet, as the lasers have a different beam radius, it is not possible to adjust the argon laser *power*. However, the applied laser switching scheme provides spectra for each laser present in the interaction zone alone. The corresponding laser-induced fluorescence rates can be used as a measure for the laser intensities. As all scans are performed in the asynchroneous mode[3], the average number of ions over the scan is constant. The Gaussian shape of the ion velocity distribution is also not influencing the ion number because the dye laser scan width of 200 MHz is considerably smaller than that of the velocity distribution. At first, the fluorescence rate is calibrated with respect to the dye laser power. In order to take laser power drifts during one run into account, only the first 20 injections, where the power is to be considered stable, are chosen for the calibration. The mean fluorescence rate during these 20 injections after subtraction of the background for the different dye laser powers is shown in figure 5.13. Four of the data points (squares) are taken at a considerably higher ion current than the others (circles). Therefore, the fluorescence is normalized to the BPM rate, which reflects the total number of ions, but, as the measuring time is equal for all data points, can also be used as a measure for the metastable ions. The result is shown in the lower part of figure 5.13. Except for one, all data points lie on a curve, that can be fitted with the function

$$F = a \cdot \left(1 - \frac{1}{\sqrt{1 + \frac{P}{P^{\mathrm{sat}}}}} \right) . \tag{5.5}$$

The deviation of the data point at 0.7 mW is unreasonably large and has therefore been excluded from the analysis.

This calibration is now used to determine an actual mean effective power[4] for both lasers from the respective normalized fluorescence rates, averaged over the run. As a result the sum of the dye laser effective power and the argon laser effective power serves as a measure for the total laser intensity seen by the ions in their rest frame. In figure 5.14 the Lamb dip center frequencies, measured with respect to the iodine line center, are plotted versus the corrected laser intensities (both laser powers summed up). The three curves reflect the data taken at three different radio-frequencies for the acousto-optic modulator in the argon laser beam. The measurement reveals a slight shift of the Lamb dip with increasing laser intensity. This shift is supposed to be caused by serveral effects. First of all, the photon scattering rate is increasing at high laser intensities leading to possible local changes in the ion velocity distribution giving rise to AC-Stark shifts. However, no significant modulation in the ion number is observable in the spectra taken, when the

[3] Laser scan start and ion injection are decoupled as described in the preceding subsection.

[4] effective power: power related to the dye laser beam radius serving as a measure for the laser intensity. For the dye laser the effective power equals the actual power. For the argon ion laser the

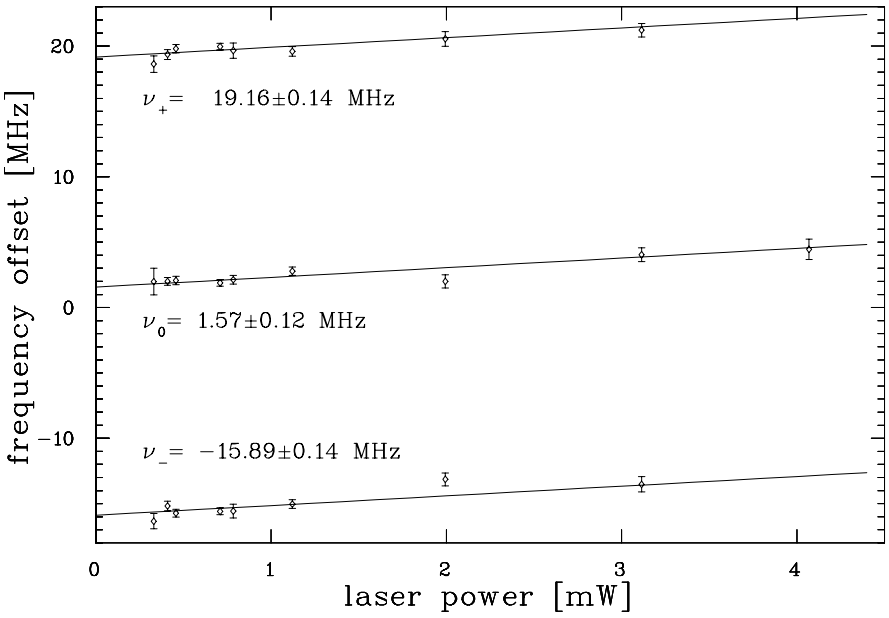

Figure 5.14: *Center frequencies of the Lamb dip as a function of the applied sum of the two laser powers. The single laser powers are determined via the laser-induced fluorescence averaged over a run, which is measured during the time intervalls (1) and (2), respectively, where the lasers are switched on separately. The fluorescence is calibrated by the total dye laser power, which has been measured with a semiconductor power meter and transformed into the ions rest frame before each run. In this way the argon laser power is related to the transverse dye laser profile via the laser-induced fluorescence. Thus, the sum of the effective laser powers is proportional to the total laser intensity experienced by the ions.*

argon laser is switched on alone. A second cause for frequency shifts may arise from the ion beam divergence (see chapter 4.2). An increase of the laser intensity would saturate ions, that are moving more and more aside the central orbit. As the ion beam contains a small fraction of hot ions, which has a larger diameter as well as a larger mean divergence, more ions having larger mean divergences contribute to the Lamb dip leading to a shift to higher frequencies.

All three data sets can be well fitted using a linear function in the laser power. The radio frequencies of the acousto-optic modulator of the argon ion laser differ by 20 MHz respectively, leading to a corresponding frequency offset of 17.6 MHz between the three data sets (see section 5.4.1). Therefore, the three curves must have the same slope. Figure 5.14 shows a linear fit to all three data sets with a

effective power is lower than the actual one because its beam radius is larger than that of the dye laser.

common slope. By extrapolation to zero intensity we get the Lamb dip frequencies, which should be free from all intensity-caused shifts. As the frequency error caused by nonlinearities in the dye laser scan decreases with decreasing offset of the Lamb dip with respect to the iodine line (absolute frequency reference), we use the result of the middle curve for the absolute frequency determination of the Lamb dip:

$$\nu_\Delta = 1570 \pm 120\,\mathrm{kHz}. \tag{5.6}$$

The results of the outer curves are taken to check the relative frequency calibration. The offset between the curves are 17.59 MHz and 17.46 MHz, respectively, which deviates by about 1% from the expected value of 17.6 MHz. As the measured Lamb dips lie away from the iodine lines by less than 5 MHz, the relative frequency calibration contributes an error of 50 kHz.

Since no model is known for the intensity dependence of the Lamb dip frequency, the data has also tentatively been fitted with a square root function, as it would be expected if some saturation effect caused the shift:

$$\nu_\Delta = \nu'_\Delta + \sqrt{\frac{P}{P^{\mathrm{sat}}}}. \tag{5.7}$$

Here, P^{sat} is the free parameter. Like in the linear fit all three curves must show the same behaviour except for an offset. P^{sat} is therefore a common fit parameter for all three curves. The result is shown in figure 5.15. The χ^2 value for this fit is somewhat lower than for the linear case, but still acceptable and results in

$$\nu'_\Delta = 1250 \pm 120\,\mathrm{kHz}. \tag{5.8}$$

The difference of 320 kHz between this value and the value from the linear fit is considered to reflect the largest possible uncertainty caused by the extrapolation.

Line broadening

In the old TSR experiment testing time dilation with Λ-spectroscopy the frequency determination was mainly limited by a large broadening of the resonance to 60 MHz (the natural linewidth is 3.8 MHz), which could not be explained by saturation. As long as the origin of this broadening was not determined, it could not be ruled out, that the same mechanisms also lead to frequency *shifts*.

Figure 5.16 shows the width of the Lamb dips as a function of the sum of the laser powers. The data is fitted by $\Delta\nu = a\sqrt{1 + P/P^{\mathrm{sat}}}$ describing saturation broadening. From extrapolation to zero power we get the unsaturated linewidth which is of the order of 11 MHz. Part of the remaining broadening is due to the modulation of the lasers, which have amplitudes of at least 2 MHz. This leads to

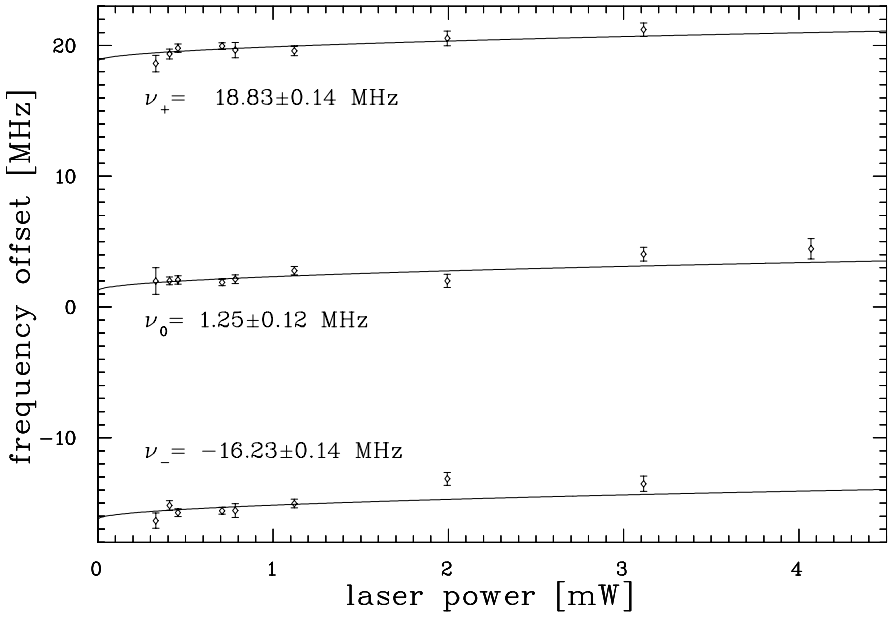

Figure 5.15: *In this picture the intensity-dependence of the frequency offset of the Lamb dip from the iodine line center is fitted with a square root function as would be expected if the dependence was caused by a saturation effect. The extrapolated value for the frequency offset deviates by 320 kHz from the linear fit shown in figure 5.14.*

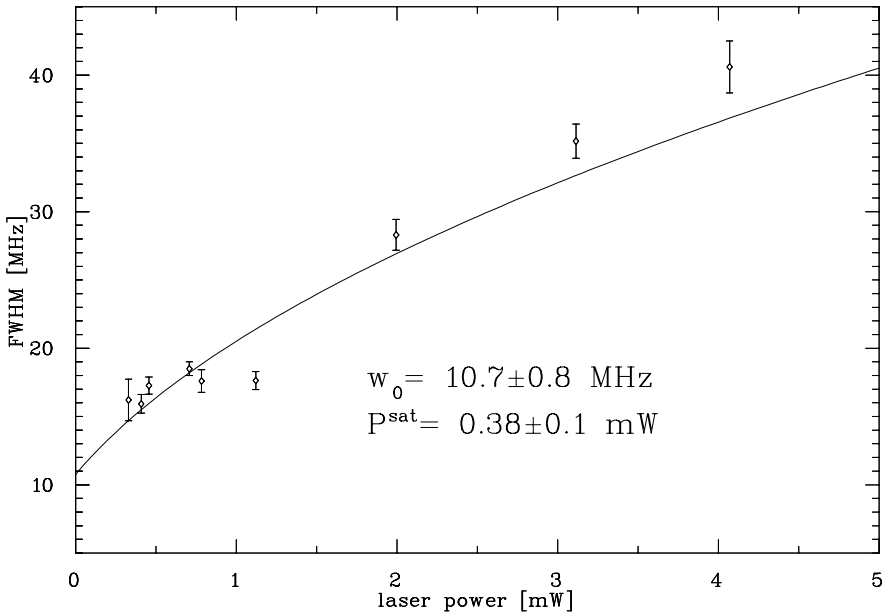

Figure 5.16: *Saturation broadening. The extrapolation to zero yiels the unsaturated width. Only a small further broadening remains, that, however, can be explained.*

a estimated modulation broadening of the resonance of at least 7 MHz following the discussion in [Bayer-Helms and Helmcke, 1977]. Furthermore, the AC-Stark shifts of the off-resonant ions in the velocity distribution, which average to zero, lead to a broadening.

The fit also yields the saturation power $P^{\text{sat}} = 380\ \mu$W, which corresponds to an intensity of 16 mW/cm^2. This is about a factor of two larger than the theoretical value. One reason for this deviation is the data point near 1 mW, which deviates strongly from the fit. Another reason may be the AC-Stark broadening, which scales linearly with the laser power, but is not contained in the fit function.

In conclusion, the width of the resonances is well understood. It is caused by mechanisms, which are not expected to cause additional shifts that are not included in our analysis of systematic errors.

Laser-ion-beam misalignment

The frequency error connected to laser-ion beam misalignment ($\theta = \phi \neq 0$, case I) as well as laser-laser beam misalignment ($\theta = 0, \phi \neq 0$, case II) has been

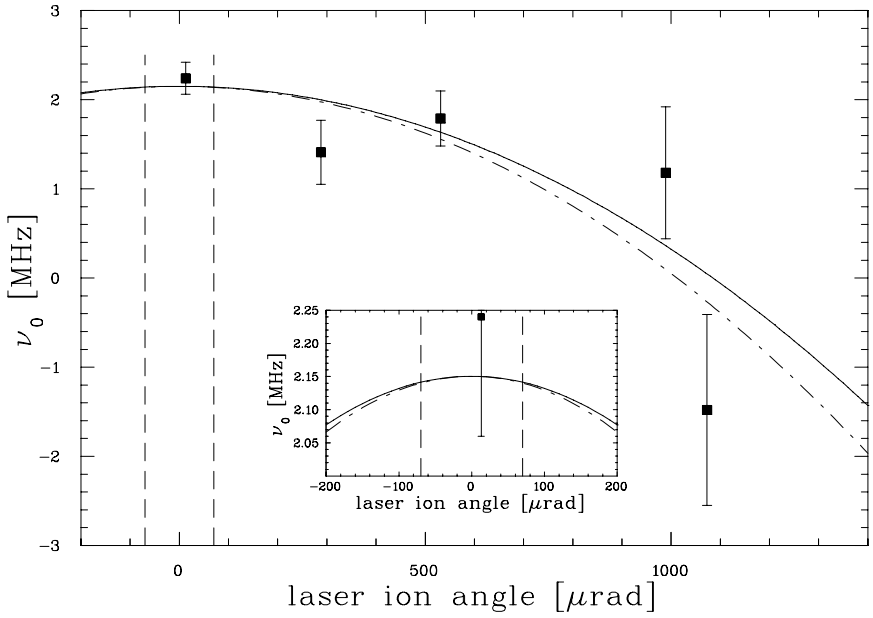

Figure 5.17: *Shift of the center frequency of the Lamb dip as a function of the angle of the ion beam with respect to the two laser beams (case I). The parabolic fit (solid line) agrees well with the calculated curve (dashed line). The vertical dashed lines indicate the experimental uncertainty.*

measured. For case I[5] the dye laser is first overlapped with the ion beam at a defined angle, which is controlled by means of motor-scans, from which the angle can be derived very accurately. In a second step, the argon ion laser is overlapped with the dye laser exactly with help of the aperture. The center of rotation is chosen to lie at the position of PM3 in order to maximize the overlap. For case II the dye laser is adjusted parallel to the ion beam and the argon laser is reflected at an angle. The Lamb dip has been recorded for different angles adjusted in this way. All data points have been taken at a laser power of 300 μW and with the laser scan decoupled from the injection. The results are shown in figure 5.17 for case I and in figure 5.18 for case II.

For the laser-ion angle the measurement (the solid line in figure 5.17 is a parabolic fit) agrees with the expected behaviour described by equation 4.6, which is indicated by the dashed line in figure 5.17. The vertical dashed lines indicate the uncertainty of the adjustment of 70 μrad. The corresponding systematic frequency error amounts to less than 10 kHz.

The frequency shift caused by the laser-laser angle (figure 5.18) turned out to

[5]Laser-ion angle: both lasers are tilted by the same angle with respect to the ion beam as defined in section 4.1, i.e. $\theta = \phi$.

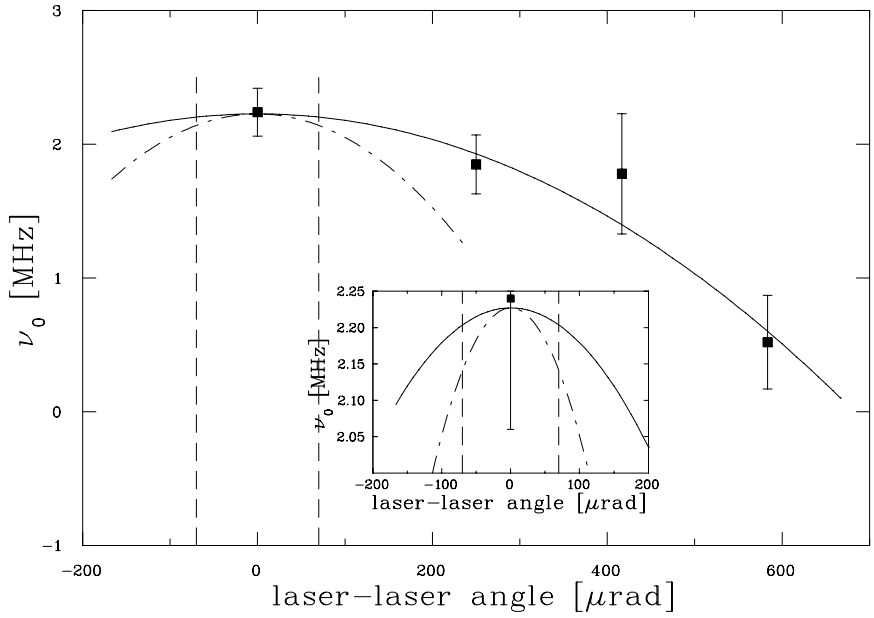

Figure 5.18: *Shift of the center frequency of the Lamb dip as a function of the angle between the laser beams (case II). The dye laser is parallel to the ion beam in this measurement. The parabolic fit (solid line) shows a weaker dependence on the angle than expected (dashed line).*

be smaller than predicted by formula 4.8. This can be explained by the spherical wavefronts of the Gaussian beams. In the derivation of equation 4.8 a plane wave has been assumed. The relevant angle in the experiment is the angle of the photon direction, which is given by the normal vector to the wavefront, with respect to the ion propagation. For plane waves this angle equals the ion-laser angle. In the case of a Gaussian beam, however, these two angles are generally different, dependent on the position of the center of rotation. The laser-laser angle is accomplished by tilting the argon ion laser around the mirror. As can be seen in figure 5.8, this point is near the center of the spherical wavefront at the position of photomultiplier 3. Thus, the angle between photon and ion propagation direction is considerably smaller than the angle between the ion and the laser beam. The vertical dashed lines in figure 5.18 indicate the uncertainty of the adjustment of about 70 μrad, which leads to a frequency shift of below 40 kHz.

It should be noted that in the laser-ion angle measurement (case I), the full rotation applies, because the center of rotation coincides with the wavefront at PM3 where the fluorescence is detected. Thus, the measurement reflects the expected angle dependence.

AC-Stark shift

The interaction of near-resonant electromagnetic radiation with an atom leads to a light-induced shift of the energy levels involved in the transition (AC-Stark shift). When this transition is probed with another radiation field, the resonance frequency is shifted with respect to the unperturbed transition frequency. These shifts have to be taken into account in saturation spectroscopy as well as Λ-type spectroscopy. Qualitatively, light shifts can be expressed as [Bjorkholm and Liao, 1975]

$$\Delta\omega \propto I_0 \frac{\omega_0 - \omega_\mathrm{L}}{(\omega_0 - \omega_\mathrm{L})^2 + \gamma^2}, \tag{5.9}$$

where I_0 denotes the laser intensity, ω_0 is the atomic transition frequency and ω_L is the laser frequency. For saturation spectroscopy on an inhomogeneously broadened ion ensemble this means, that off-resonant ions give rise to a shifted Lamb dip frequency. However, since the effect is symmetric around ω_0, there are as many ions with a frequency $\omega = \omega_0 - \delta\omega$ present as ions with a frequency $\omega = \omega_0 + \delta\omega$, when the argon ion laser is exactly resonant with the center of the velocity distribution. The AC-Stark shifts then average to zero only causing a broadening of the Lamb dip.

If the argon ion laser is not centered within the ion velocity distribution, the Lamb dip will experience a net line shift. After equation 5.9 only ions within a range of the order of $\pm\gamma$ (the natural line width ≈ 4 MHz) cause a significant AC-Stark-shift, which is much smaller than the width of the velocity distribution (FWHM=3200 MHz). Hence, we use the slope of the velocity distribution as a measure of the asymmetry in the number of ions with slower and ions with higher velocity, respectively. A Gaussian $G(\nu-\nu_0)$ has its maximum (absolute) slope one standard deviation σ away from the line center. This maximum slope is dependent on σ: $G'(\sigma - \nu_0) = A/(\sqrt{2\pi e}\sigma^2)$, where A denotes the area of the Gaussian.

For this reason, a high stability of the mean ion velocity is of great importance. To reduce the typical long-term drift of the ion velocity of about 1 GHz, which is caused by the instability of the cathode voltage of the electron cooler, we applied the technique of ion beam bunching as described in chapter 3.1.2. For the mean velocity of a bunched ion beam is determined by the bunching frequency, which defines the velocity of the pseudo-potential co-moving with the ions. The bunching frequency is more stable as well as fine-adjustable, so that the center of the velocity can be set to resonance with the argon ion laser very accurately. If the velocity of the electron beam in the electron cooler deviates from the velocity of the bunching potential, the ion velocity will approach an equilibrium velocity in between. Thus, the buncher reduces possible drifts of the ion velocity caused by the electron cooler. In addition, the width of the velocity distribution increases

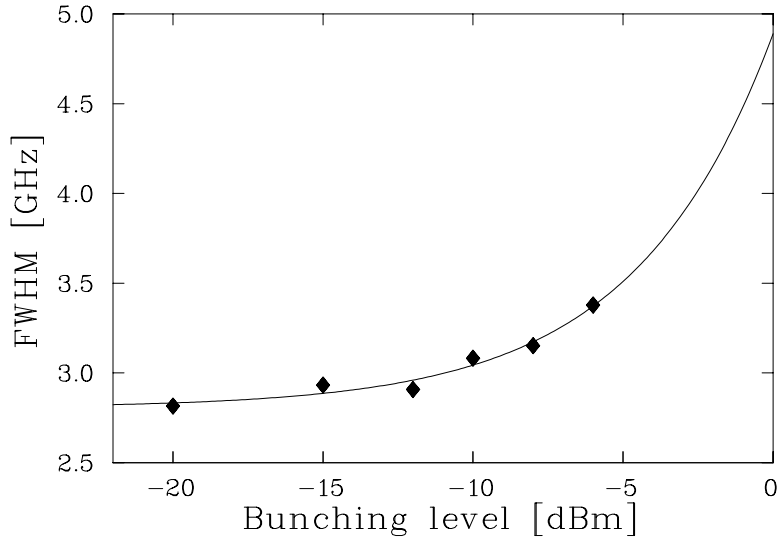

Figure 5.19: *FWHM of the ion velocity distribution versus bunching amplitude. The data can be fitted exponentially.*

exponentially with the bunching amplitude (see figure 5.19). Since the maximum slope of the Gaussian distribution is inversely proportional to the square of the width, AC-Stark shifts due to possible drifts of the ion velocity decrease. We applied a bunching amplitude of -8 dBm leading to a broadening of the velocity distribution from 2.8 GHz to 3.2 GHz.

In order to estimate the influence of the AC-Stark shift caused by residual instabilities of the ion velocity, we detuned the electron cooler voltage from the correct value. From a fluorescence scan on the two-level transition with the dye laser only, we determine the slope of the velocity distribution at the position resonant with the argon laser. Subsequently, we measured the Lamb dip with both lasers. Figure 5.20 shows the result of a set of such measurements at a laser power of 300 μW for each laser. The Lamb dip center frequency is plottet versus the slope of the velocity distribution, normalized to the maximum slope. The extrapolation of the linear fit to 100% of the maximum slope gives an estimate for an upper limit for the AC-Stark shift possible at that laser power. Figure 5.21 shows a second measurement at 1 mW for each laser. The plot of the maximum AC-Stark shift versus the laser power (figure 5.22) allows to interpolate to arbitrary powers with the expected linear dependence given by equation 5.9 (solid line).

The position of the velocity distribution was checked frequently during the beamtime. The remaining drifts can be estimated from these observations to less than 30% of the maximum slope (dashed line in figure 5.22). This leads to a corresponding shift for each data point in the intensity-dependent Lamb dip mea-

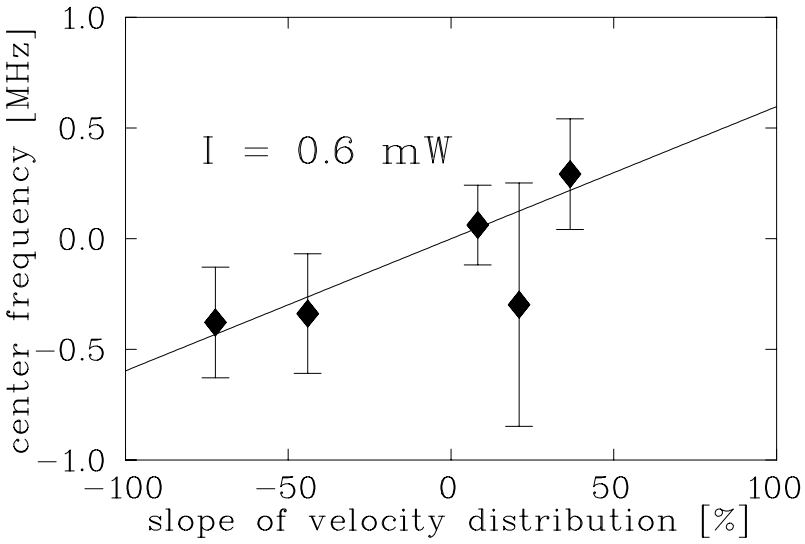

Figure 5.20: *Measurement of the AC-Stark shift at 300 μW for each laser. The Lamb dip center frequency is plotted versus the slope of the velocity distribution at the position of the argon ion laser and serves as a measure of the asymmetry in the ion number around this point.*

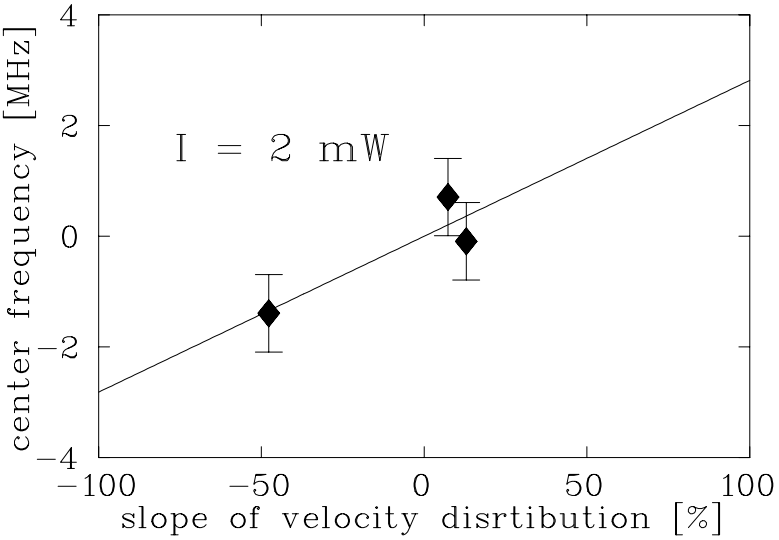

Figure 5.21: *AC-Stark shift measurement with 1 mW for each laser.*

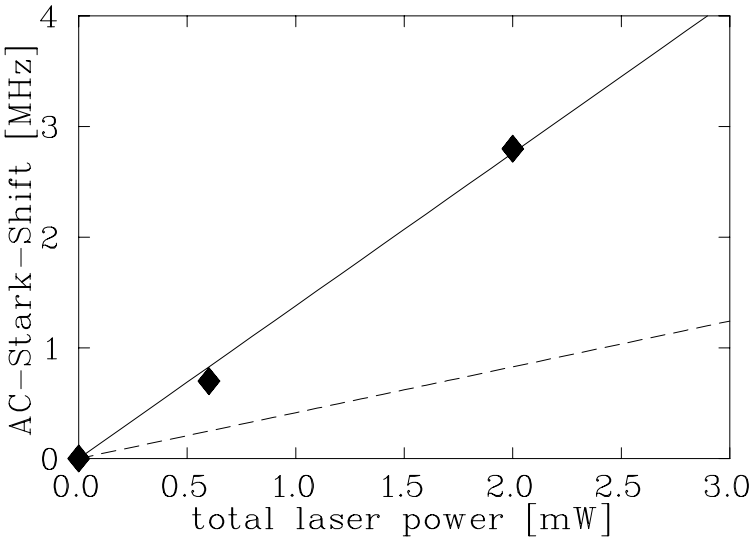

Figure 5.22: *The maximum possible AC-Stark shift, which occurs, when the argon ion laser is resonant with ions at maximum slope of the velocity distribution, is plottet versus total laser power (solid line). The dashed line indicates the AC-Stark shifts caused by remaining drifts of the ion velocity distribution, which are estimated to be below 30% of the maximum slope.*

surement 5.14. However, in the extrapolation to zero intensity the AC-Stark shifts average to zero. Even a slight systematic misadjustment of the velocity distribution would not cause a shift in the extrapolated Lamb dip frequency, because the AC-Stark shift is linearly dependent on the intensity as well.

In conclusion the systematic error for the extrapolated Lamb dip frequency caused by AC-Stark shifts is negligible. Due to random drifts the shifts may lead to a weak scattering of the data points, which is contained in the fit error.

Laser profile curvature effects

In section 4.3 the influence of the phase behaviour of the Gaussian beam shape of the lasers on the Lamb dip frequency has been discussed. It turned out that for exactly mode-matched laser beams the corresponding shifts would cancel. The longitudinal beam shapes of both lasers have been determined very accurately. Figure 5.8 shows the result. The knowledge of the positions of the foci and the Rayleigh ranges of the lasers allows for estimating the frequency shifts according to equation 4.19 with a Monte Carlo simulation. An ensemble of ions distributed along and around the beam axis in the beam has been assumed. For each ion the frequency shift due to the local phase properties of the laser beams is calculated. All ions have been assumed to travel parallel to the laser axis ($\theta = \phi = 0$). Thus

only the terms for the on-axis frequency shift as well as for the off-axis frequency shift have been considered. In a second step the divergence of the ion beam has been taken into account by assuming a Gaussian distribution of the angles of the ions with respect to the laser beam axis. For each ion in the simulation an additional frequency shift caused by the respective angle relative to the laser beam has then been calculated after equation 4.6. Thus, for the calculation of this shift a plane wave has been assumed. The contribution of these ions to the fluorescence signal is dependent on their distance from photomultiplier 3. Therefore the respective frequency shifts are weighted with an exponential factor according to the lifetime of the upper level of the two-level system of 43 ns, which corresponds to a path length of the ions of 80 cm. In order to estimate the uncertainty of the simulation the parameters describing the laser beams, namely the beam waist w_0 and the position of the focus z_0, and the ion beam size σ_{ion} have been varied. In this way the uncertainty of the frequency shift can be derived from the respective uncertainties of the parameters. The frequency shifts $\delta\nu^{\mathrm{wf}}_{\mathrm{Dye}}$ and $\delta\nu^{\mathrm{wf}}_{\mathrm{Ar}}$ due to these curvature effects resulting from the simulation, which has been done for both lasers separately, are

$$\delta\nu^{\mathrm{wf}}_{\mathrm{Dye}} = -665 \pm 159\ \mathrm{kHz} \tag{5.10}$$

$$\delta\nu^{\mathrm{wf}}_{\mathrm{Ar}} = +179 \pm 66\ \mathrm{kHz}. \tag{5.11}$$

The sign of the respective shift is determined by the propagation direction of the respective laser with resect to the ion beam direction. As the focus of the dye laser is only one Rayleigh range away from photomultiplier 3 compared to 2.6 Rayleigh ranges in the case of the argon ion laser, the absolute value of the corresponding shift is considerably larger for the dye laser.

Magnetic strayfields

The magnetic strayfields near the photomultiplier 3, which takes the spectroscopic data, have been measured to be of the order of 1 Gauß. These fields are mainly caused by ion pumps installed in the experimental section as well as by the terrestrial magnetic field. The corresponding Zeeman shift of the magnetic sublevels of the levels involved in the two-level transition is of the order of 1 MHz. However, the laser light applied in the spectroscopy is linearly polarized so that no optical pumping will occur. As the Zeeman shifts of the single levels are symmetric and the populations will stay balanced because of the absence of optical pumping, no systematic shift but only a slight broadening is expected.

The deflection of the ion beam by these strayfields are below 50 μrad leading to frequency shifts of about 5 kHz according to equation 4.6.

The influence of the magnetic strayfields can, therefore, be neglected.

	Frequency [kHz]	1σ error [kHz]
Experimental result:		
iodine reference line $\nu_{\mathrm{a-comp}}$	512 671 028 023	152
residual Doppler background (Iodine)		80
AOM shift of dye laser $\delta\nu_{\mathrm{Dye}}^{\mathrm{AOM}}$	414 000	negligible
Lamb dip offset to reference line ν_{Δ}	1 570	120
Wavefront correction (dye laser) $\delta\nu_{\mathrm{Dye}}^{\mathrm{wf}}$	-665	159
laser-laser angle		40
laser-ion angle		10
rel. frequency calibration		50
total $\nu_{\mathrm{a}}^{\mathrm{exp}}$	512 671 442 928	269
Prediction from special relativity:		
argon laser reference line $\nu_{\mathrm{a2-comp}}$	582 490 603 370	144
AOM shift of argon laser $\delta\nu_{\mathrm{Ar}}^{\mathrm{AOM}}$	-400 000	negligible
Wavefront correction (argon laser) $\delta\nu_{\mathrm{Ar}}^{\mathrm{wf}}$	+179	66
$^{7}\mathrm{Li}^{+}$ rest frequency	546 466 918 790	400
total $\nu_{\mathrm{a}}^{\mathrm{SR}}$	512 671 443 249	765

Table 5.1: *The result of the saturation spectroscopy*

5.4.3 Result of the saturation spectroscopy

Table 5.1 comprises all relevant frequencies as well as uncertainties and systematic errors discussed in the previous section.

The systematic errors have been considerably lowered compared to the old TSR experiment (see chapter 2.5). A great deal of this improvement was achieved using acousto-optic modulators. Firstly, the shift of the resonance into the vicinity of the iodine line as well as the generation of frequency markers by doing the spectroscopy at three different relative distances of the signal with respect to the iodine line reduced the error of the relative frequency calibration of the dye laser. Secondly, the quasi-simultaneous measurement of the Lamb dip and the Doppler background by fast laser switching with help of the AOMs eliminated the error caused by the limited lifetime of the ions. Systematic frequency shifts through misalignment of the lasers with respect to the ion beam were achieved by the motor-scan measurements. Slow drifts of the electron cooler voltage and, therefore, the ion velocity giving rise to fluctuations of the fluorescence background and AC-Stark shifts, were improved by ion beam bunching. Intensity-dependent frequency shifts like AC-Stark shifts due to population changes caused by laser forces were eliminated by extrapolation of the Lamb dip center frequency, measured at different laser powers, to zero power. A linear fit yielded a sufficient

confidence level.

A comparably large shift was caused by wavefront curvature effects, which, however, could be estimated in a Monte-Carlo simulation. Nevertheless, the errors of this simulation contribute quite strongly to the total error, so that the curvature effects should be reduced in future measurements by adjusting the longitudinal profile of the lasers such, that the relevant interaction region (at PM3) lies far outside the Rayleigh range. The measurement of the beam diameter in the experimental section by means of the motor-scans makes the control of the longitudinal profiles possible.

Finally, the result of the frequency measurement of the Lamb dip is:

$$\nu_{\mathrm{a}}^{\mathrm{exp}} = 512\ 671\ 442\ 928 \pm 269\ \mathrm{kHz}. \tag{5.12}$$

This has to be compared to the prediction from Special Relativity using the lithium rest frame frequency:

$$\nu_{\mathrm{a}}^{\mathrm{SR}} = \frac{\nu_0^2}{\left(\nu_{\mathrm{a2-comp}} + \delta\nu_{\mathrm{Ar}}^{\mathrm{AOM}} + \delta\nu_{\mathrm{Ar}}^{\mathrm{wf}}\right)} = 512\ 671\ 443\ 249 \pm 765\ \mathrm{kHz}, \tag{5.13}$$

so that the difference results in

$$\delta = \nu_{\mathrm{a}}^{\mathrm{exp}} - \nu_{\mathrm{a}}^{\mathrm{SR}} = -321 \pm 811\ \mathrm{kHz}. \tag{5.14}$$

The deviation between experiment and Special Relativity shows to be well within the $1\ \sigma$ error.

The square root fit to the intensity-dependent Lamb dip frequency, which we consider as the largest conceavable systematic deviation from the linear fit, yields $\delta = -612 \pm 800$ kHz, which still agrees within $1\ \sigma$ and does, therefore, not affect the accuracy of the experiment at the present status.

To infer the result for an upper limit for the test parameter α from this, we start from equation 2.30. The second term describes sidereal and diurnal variations. As the ion velocity β is large compared to the velocity w of the laboratory with respect to the rest frame of the cosmic background radiation, the second term can be neglected. The remaining equation reads:

$$\frac{\nu_{\mathrm{a}}^{\mathrm{exp}}\nu_{\mathrm{p}}}{\nu_0^2} = 1 + 2\alpha\beta^2. \tag{5.15}$$

Solving this equation for α and using the relations $\nu_{\mathrm{a}}^{\mathrm{SR}} = \nu_0^2/\nu_{\mathrm{p}}$ and $\delta = \nu_{\mathrm{a}}^{\mathrm{exp}} - \nu_{\mathrm{a}}^{\mathrm{SR}}$ we obtain

$$\alpha = \frac{1}{2\beta^2} \cdot \frac{\delta}{\nu_{\mathrm{a}}^{\mathrm{SR}}}. \tag{5.16}$$

Our experiment provides a new upper limit for α of

$$\alpha < 1.8 \times 10^{-7}, \tag{5.17}$$

which is the most accurate measurement of time dilation and means an improvement of a factor of 4 compared to the previous TSR experiment [Grieser et al., 1994b]. The result is now limited by the uncertainty of the predicted Lamb dip frequency $\nu_{\mathrm{a}}^{\mathrm{SR}}$, which is mainly caused by the uncertainty of the rest frame frequency ν_0 of 400 kHz, that contributes to $\nu_{\mathrm{a}}^{\mathrm{SR}}$ quadratically leading to an error of $\Delta\nu_{\mathrm{a}}^{\mathrm{SR}} = 800$ kHz. To further improve the test of the time dilation factor it is necessary to lower the uncertainty of the rest frame frequency. As an alternative we plan to repeat the storage ring measurement on an ion beam at the lowest possible velocity in TSR. This is described in further detail in section 6.3.

The frequency measurement can not only be used to test Special Relativity, but also to derive a more accurate value for the lithium rest frame frequency ν_0, when Special Relativity is assumed to hold. In this case we have $\nu_{\mathrm{a}}\nu_{\mathrm{p}} = \nu_0^2$, which is independent of the velocity. Therefore, we can calculate the restframe frequency as

$$\nu_0 = \sqrt{\nu_{\mathrm{a}}\nu_{\mathrm{p}}} \tag{5.18}$$

$$\Delta\nu_0 = \sqrt{\left(\frac{\nu_{\mathrm{p}}}{2\nu_0}\right)^2 \Delta\nu_{\mathrm{a}}^2 + \left(\frac{\nu_{\mathrm{a}}}{2\nu_0}\right)^2 \Delta\nu_{\mathrm{p}}^2} \tag{5.19}$$

with $\nu_{\mathrm{a}} = \nu_{\mathrm{a}}^{\mathrm{exp}}$ and $\nu_{\mathrm{p}} = \nu_{\mathrm{a2-comp}} + \delta\nu_{\mathrm{Ar}}^{\mathrm{AOM}} + \delta\nu_{\mathrm{Ar}}^{\mathrm{wf}}$. Because of the square root dependence of ν_0 on the measured frequency ν_{a} (and also ν_{p}) the error $\Delta\nu_0$ is below the measurement error. For our result a new improved rest frame frequency is obtained

$$\nu_0 = 546\,466\,918\,452 \pm 158 \text{ kHz}. \tag{5.20}$$

However, it must be emphasized, that this result assumes time dilation to be valid on a level better than confirmed experimentally.

5.5 Λ-spectroscopy

In the old 1994 experiment testing the time dilation factor at TSR Λ-spectroscopy was performed [Grieser et al., 1994b]. The accuracy was hampered by an unaccounted 15fold line broadening to about 60 MHz. Laser wavefront distortions and other effects were supposed to be the reason for this broadening and, therefore, limited the accuracy of the determination of the line center, because the effects causing the broadening possibly lead to line shifts as well.

We started our measurements at TSR by replacing the old windows, which showed a surface flatness of $3\ \lambda/\mathrm{cm}$, by windows with a $1/2\ \lambda/\mathrm{cm}$ flatness[6]. Consequently, the wavefront distortions are significantly lowered, so that narrower Λ-resonances were expected.

In order to detect the Λ-resonance, one has to tune the ion velocity such, that the argon ion laser is resonant with the ${}^3S_1(5/2) \rightarrow {}^3P_2(5/2)$ transition for ions in the center of the velocity distribution. A detuning would lead to lower fluorescence and would give rise to AC-Stark shifts. To monitor the position of the argon ion laser within the ion velocity distribution, the dye laser is scanned across the ${}^3S_1(5/2) \rightarrow {}^3P_2(7/2)$ two-level transition with the argon laser on. The common ground state of the transition is depleted into the $F = 3/2$ state due to optical pumping by the argon ion laser. The fluorescence signal shows a dip at the corresponding frequency (V-resonance). Figure 5.23 shows the result of such a measurement. The V-resonance turns out to be much broader (about 1 GHz) than the argon ion laser linewidth, which can be explained as follows: The argon ion laser burns a hole into the velocity distribution, that has a lifetime of roughly 100 ms [Klein, 1991]. This long lifetime increases the saturation parameter related to the applied laser power by orders of magnitude, because only very rare pumping transitions are necessary to deplete the $F = 5/2$ ground state [Klein, 1991]. This broadening of the V-resonance strongly limits the accuracy of the adjustment of the ion velocity, which constitutes a disadvantage of Λ-spectroscopy compared to saturation spectroscopy.

The Λ-signal is now obtained by tuning the dye laser across the ${}^3S_1(3/2) \rightarrow {}^3P_2(5/2)$ transition. Figure 5.24 shows one of the first surprising results. As opposed to the expectation of a narrower linewidth, we detected resonances with widths of about 500 MHz. The lineshape is composed of two components. In a first analysis the double-peak structure is fitted with the sum of a Gaussian accounting for the broad background peak and a Lorentzian describing the narrow peak sitting on top. The width of the background structure is about $\Delta\nu_{\mathrm{FWHM}} = 780$ MHz for both photomultiplier spectra. However, especially for

[6] Of course it is possible to get windows with a flatness of $1/20\ \lambda/\mathrm{cm}$, but this quality decreases first by mounting them to a flange suitable for ultra-high vacuum. A further decrease of the flatness is caused by the air pressure exerted onto the windows, when subjected to the TSR-vacuum.

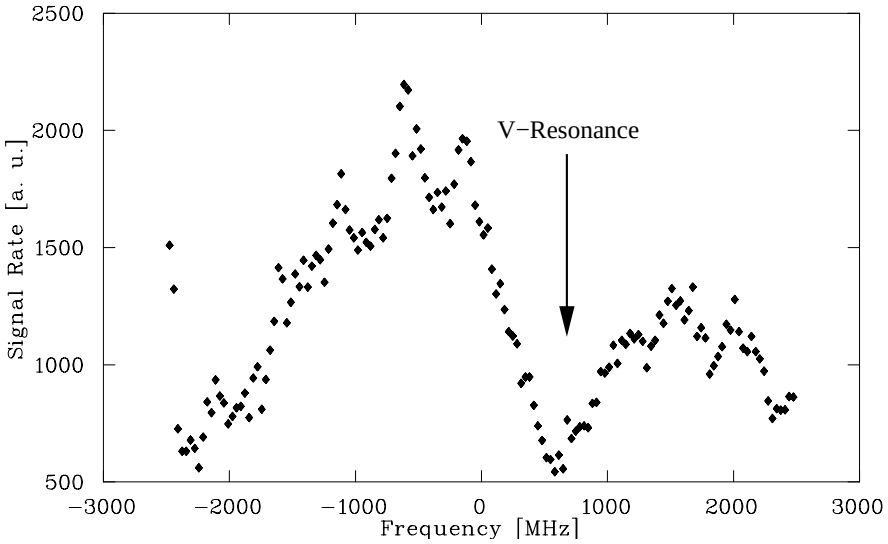

Figure 5.23: *V-resonance: The argon ion laser is tuned into resonance with the* $5/2 \rightarrow 5/2$ *transition and the dye laser is scanned over the* $5/2 \rightarrow 7/2$ *transition. Aside from the V-resonance the peaks and dips due to the slow ion velocity fluctuations are visible.*

the signal from photomultiplier 1 (PM1), which has a considerably higher detection efficiency than PM2, shows, that the broad background structure can not satisfactorily be described by a Gaussian. The fit of a Lorentzian to this background yields even worse results. The width of the narrow peak turns out to be $\Delta\nu_{\mathrm{FWHM}} = 94$ MHz for PM1 and $\Delta\nu_{\mathrm{FWHM}} = 59$ MHz for PM2, respectively. But not only the width of the narrow component of the signal is dependent on the position in the experimental section, but also the ratio of the areas of the components: at PM1 about 10% of the fluorescence is contained in the narrow component compared to 15% at PM2.

These results provide stong evidence that velocity-changing processes, occurring typically over several to many roundtrips of the ions in the storage ring, are the reason for the background fluorescence. Λ-spectroscopy is very susceptible to such velocity changes as nothing requires the two lasers to be in resonance *simultaneously*, i.e. the back-and-forth pumping between the two ground states can occur over many roundtrips in the ring. If during that time velocity-changing collisions occur, e.g. in the electron cooler, the resonance is smeared out. For ions only resonant with one laser because of their 'wrong' velocity are pumped dark

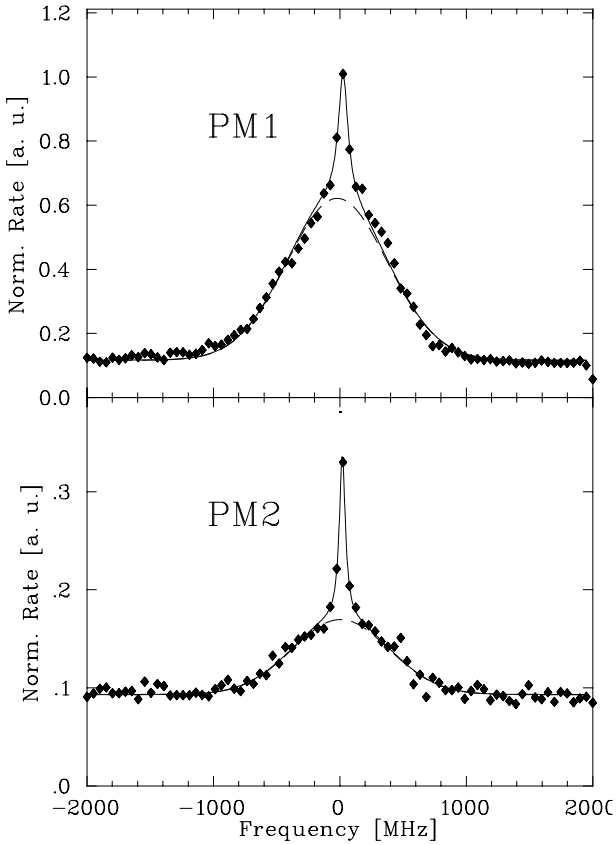

Figure 5.24: *Broad overview scan across the Λ-resonance using an unbunched ion beam, measured at two positions in the experimental section. This run contains 32 laser scans and is taken with one laser scan per injection. The ion current decrease is corrected. The double-peak structure is fitted with the sum (solid line) of a Gaussian (dashed line) and a Lorentzian.*

and should, ideally, stay dark for the rest of the scan. However, velocity changes can bring these ions into resonance with the other laser accidentally. As the Λ-signal shown in figure 5.24 has been taken with an unbunched beam, this mechanism could explain the broad background structure to be caused by the 1.6 Hz fluctuations of the ion velocity distribution described in section 5.1. These fluctuations were probably not present in the measurements by Grieser et al. in 1994. In addition, velocity-changing processes stemming from other sources may cause the remaining broadening of the narrow component of the resonance in our as well as in the Grieser experiment. E.g. a small 50 Hz fluctuation in the ion velocity distribution has been observed. Other sources for velocity-changes are intra-beam scattering [Sörensen, 1987] and collisions in the electron cooler or with rest gas

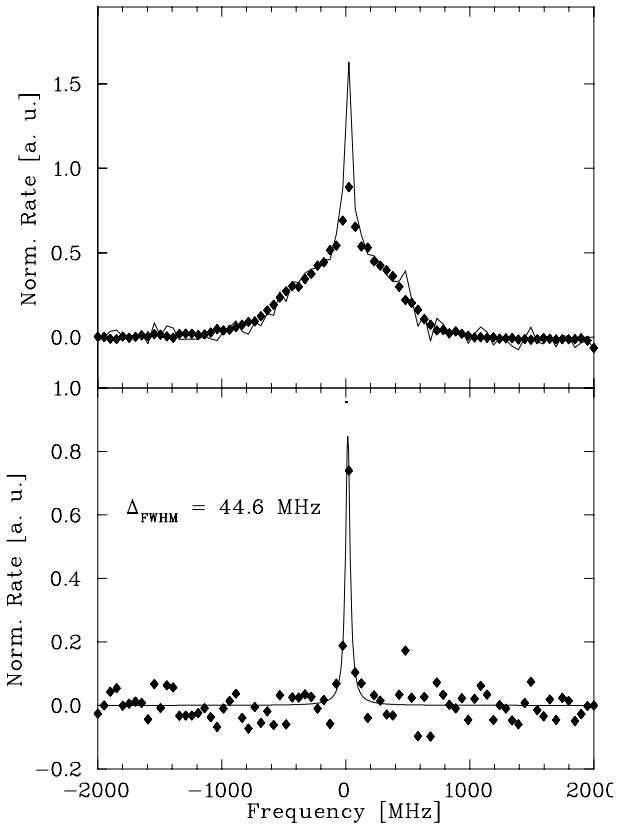

Figure 5.25: *This figure shows the same run as figure 5.24. The straylight and dark count rate background is subtracted. The upper picture shows the original signal from PM1 (data points) and the signal from PM2 (solid line), which is scaled by a factor of 6.9. The lineshape of the broad structure shows to be equal for both photomultipliers. However, the height of the narrow peak is different. In the lower graph the difference of the curves is depicted. The width of the remaining peak is smaller than the Λ-signals measured by [Grieser et al., 1994b] (60 MHz). However, there are very few data points in the resonance.*

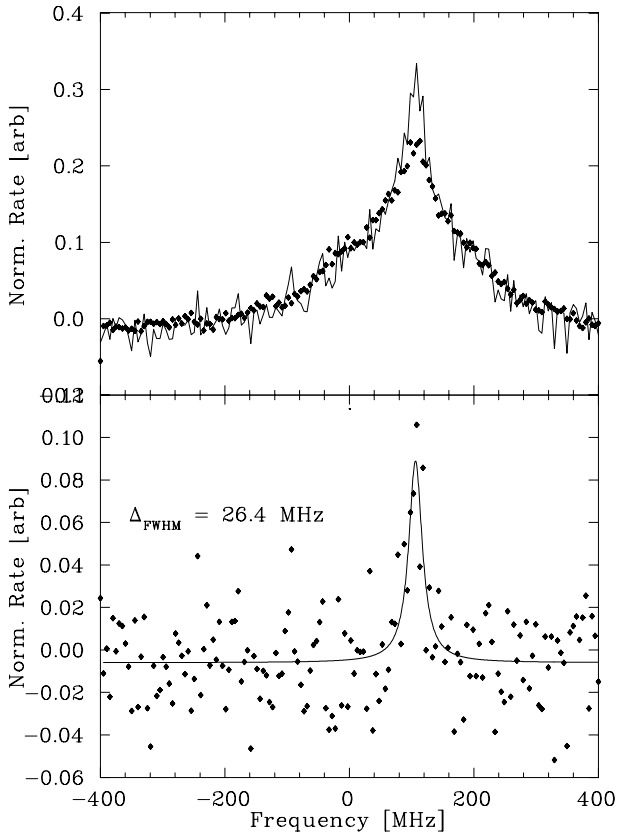

Figure 5.26: *This picture shows a scan with greater resolution. The remaining peak from the substraction of the PM1 signal from the PM2 signal now has a width of only 26 MHz, which is of the order of the width expected from saturation broadening.*

atoms. As mentioned before, the lifetime of a hole in the ion velocity distribution in TSR has been measured by [Klein, 1991] to be of the order of 100 ms.

The different fraction of fluorescence contained in the narrow peak for the two photomultipliers may in this picture be caused by the fact, that PM1 'sees' the ions coming into the interaction region first. A fraction of ions, which was resonant with laser 1 some time before, contains 100% of ions in the ground state belonging to the transition which can become resonant with laser 2 through the change of the velocity. Once they reach the overlap region between lasers and ions they are generally pumped dark into the other ground state again. During the lifetime of the upper level of 43 ns the ions travel about 80 cm in TSR, so that the major part of the back-pumping and, consequently, the fluorescence will occur in the front part of the overlap region. Therefore, the fraction of fluorescence stemming from velocity changes is larger for PM1. Further investigation revealed an asymmetry

of the lineshape of the background which is dependent on the scanning time and the scan direction. The fluorescence is higher on the side, where the dye laser scan starts and the asymmetry is stronger for decreasing scanning velocity. However, a detailed study of the dynamics has not been done yet. Nevertheless, for a given scan the background lineshape turned out to be equal at PM1 and PM2. To see this, the dark count rate background is subtracted from both signals first leaving only the double-peak structure. In a second step the PM2 signal, which is considerably lower than that of PM1 due to a lower detection efficiency of PM1 as well as due to the fact, that PM2 sees less of the fluorescence caused by the velocity changes, is scaled empirically to the same height of the background fluorescence. The result is shown in the upper graph of figure 5.25. The narrow peak of the PM2 signal exceeds the corresponding peak of the PM1 signal. In the lower picture the PM1 signal is subtracted from the PM2 signal, leaving a peak, which mainly contains fluorescence from ions, that scatter photons from both lasers within few passages through the interaction region. It can well be fitted by a Lorentzian with a width of $\Delta\nu_{\mathrm{FWHM}} = 45$ MHz, which is already below the width of 60 MHz measured by [Grieser et al., 1994b]. Figure 5.26 shows another run analyzed in the same way. Here, the scan width is decreased, so that there are more data points lying in the region of the resonance. The resulting width of $\Delta\nu_{\mathrm{FWHM}} = 26$ MHz can mainly be explained by saturation broadening.

We also recorded the Λ-resonance with the laser switching setup. A typical result is shown in figure 5.27. In this case the spectra 1 and 2 should not show a significant fluorescence signal, because in both time windows there is only one of the lasers applied and, except for a few photons per ion no fluorescense should occur, since the ions get pumped dark quickly. We interpret the fluorescence in these two spectra to be caused by velocity changes of the ions during several roundtrips in TSR. Spectrum 3 taken with both lasers switched on simultaneously also contains the fluorescence measured in spectra 1 and 2, but additionally records the "real" part of the Λ-resonance stemming from ions, that scatter photons of both lasers during one or only a few roundtrips (dependent on the duration of a time window). Therefore, the part of the signal caused by velocity changes, that occur on a time scale longer than one time window duration is subtracted from the total fluorescence in the difference spectrum.

In order to investigate the lineshape, a series of Λ-resonances has been taken with different switching frequencies ranging from 1 kHz to 200 kHz. This measurement has been done with an unbunched beam as well as with a bunched one. The results are shown in figure 5.28 and figure 5.29, respectively. In both measurements the width of the resonances decreases as the switching frequency is increased. The difference signal contains not only the "true" Λ-signal stemming from photons scattered in one passage through the interaction region. Additionally, fluorescence from ions, that perform several roundtrips according to

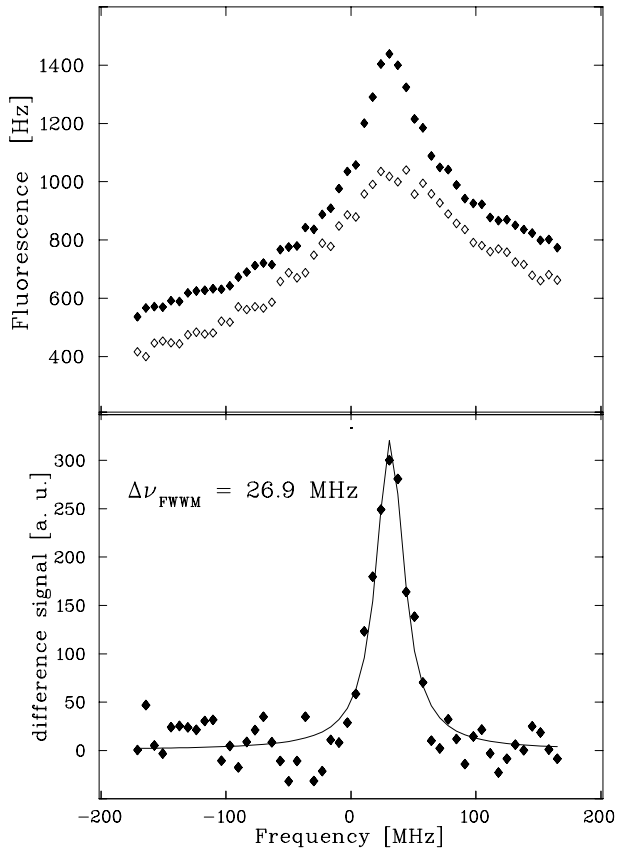

Figure 5.27: *Λ-resonance taken with the laser switching method. The upper figure shows the spectrum with both lasers switched on simultaneously (with an offset for illustration) as well as the sum of the spectra with the lasers switched on separately. In the lower picture the difference spectrum is depicted. The broad background structure stemming from ions that experience velocity changes during several roundtrips in TSR cancel out. The remaining resonance has a width of 27 MHz, that is mainly due to saturation broadening. This indicates, that practically no background fluorescence is left in the difference spectrum.*

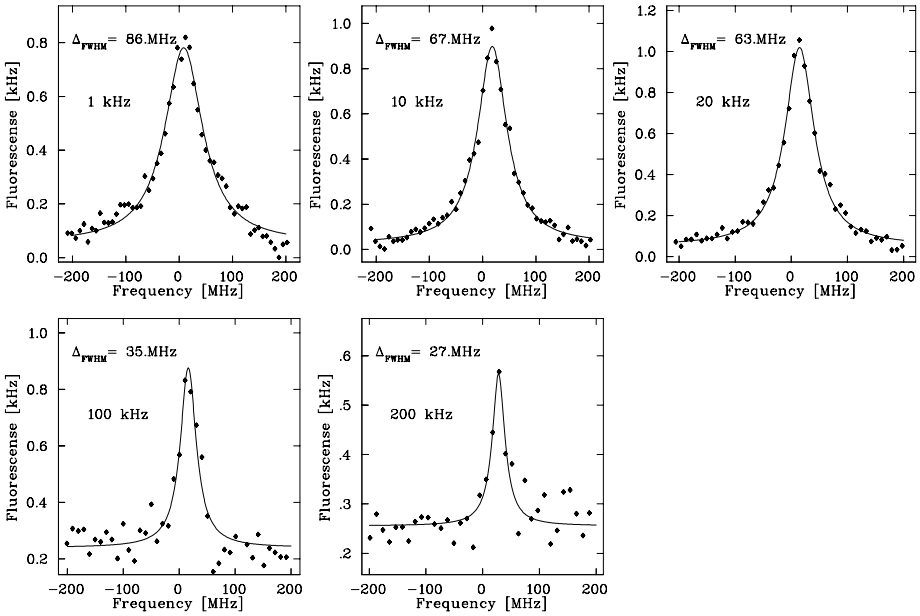

Figure 5.28: *Λ-resonance taken with the laser-switching scheme for different switching frequencies. The ion beam is not bunched in this measurement. The laser power was 2 mW for each laser.*

the duration of one time window, contribute to the difference signal. Velocity changes, that occur on this time scale lead to a broadening of the difference signal. At low switching frequencies the resonances are not only broadened, but also strongly distorted and asymmetric. For high switching frequencies more and more velocity-changing processes are cancelled out in the difference signal because they happen on time scales that are long compared to one time window and are, therefore, present in the time window with both lasers switched on simultaneously as well as in the sum of the time windows with the lasers switched on separately. In figure 5.30 and figure 5.31 the decrease of the width is empirically fitted by an exponential. For the limiting case of zero switching frequency the widths are different for the bunched and the unbunched ion beam. The Λ-resonance is broader for the bunched beam, which can be explained by the additional velocity-changing processes caused by the bunching (synchrotron oscillations). For high switching frequencies the signal widths approach the same value for the bunched and the unbunched case. In this limiting case all velocity-changing processes are cancelled out in the difference signal.

The laser power in these measurements was about 2 mW per laser. The remaining signal width of about 30 MHz corresponds to what has been observed for saturation spectroscopy (see figure 5.13). Thus, the complicated broadening

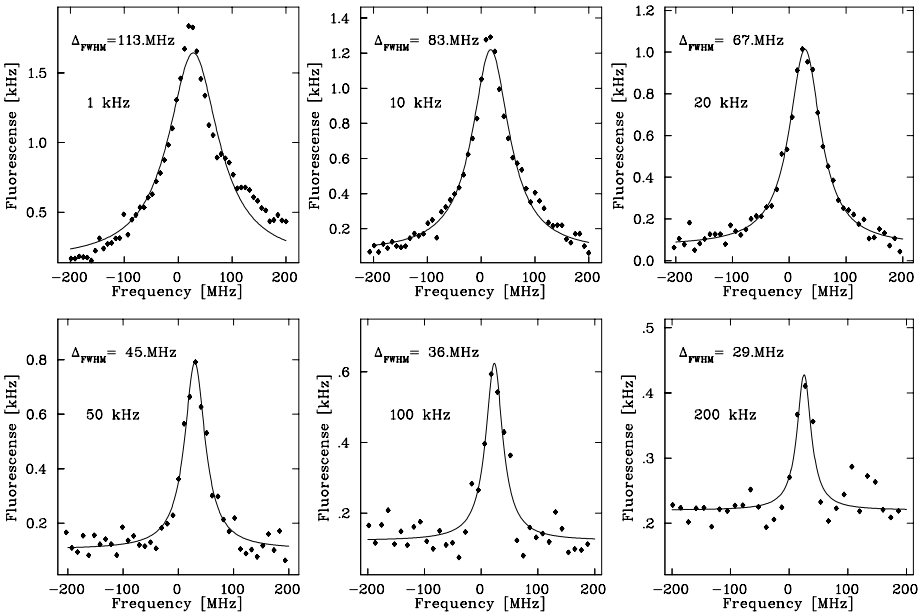

Figure 5.29: *Λ-resonance taken with the laser-switching scheme for different switching frequencies with a bunched ion beam.*

due to the velocity changes is completely suppressed and no frequency shifts are expected as well. However, as can be seen from figures 5.28 and figure 5.29 the statistics strongly decrease at high switching frequencies. Nevertheless, this can be compensated by increasing the laser powers. The corresponding saturation broadening is symmetric, does not lead to a shift of the resonance and is understood.

Until now, we did not apply Λ-spectroscopy to a new test experiment. However, as the origin of the broadening observed in the previous experiment is now understood and can be suppressed with the laser switching method, we plan to perform a test experiment similar to the measurement using saturation spectroscopy in the near future. Probably, this can also help to manifest the origin of the slight laser intensity dependence of the Lamb dip frequency in the saturation spectroscopy.

5.5.1 Reanalysis of the experiment by Grieser et al.

In the experiment of [Grieser et al., 1994b] Λ-spectroscopy has been employed to test time dilation. For this purpose the absolute transition frequencies of the two legs of the Λ have to be known. Both frequencies were calculated from the absolute frequency of the $^3S_1$(F=5/2)$\rightarrow{}^3P_2$(F=7/2) transition using the hyperfine

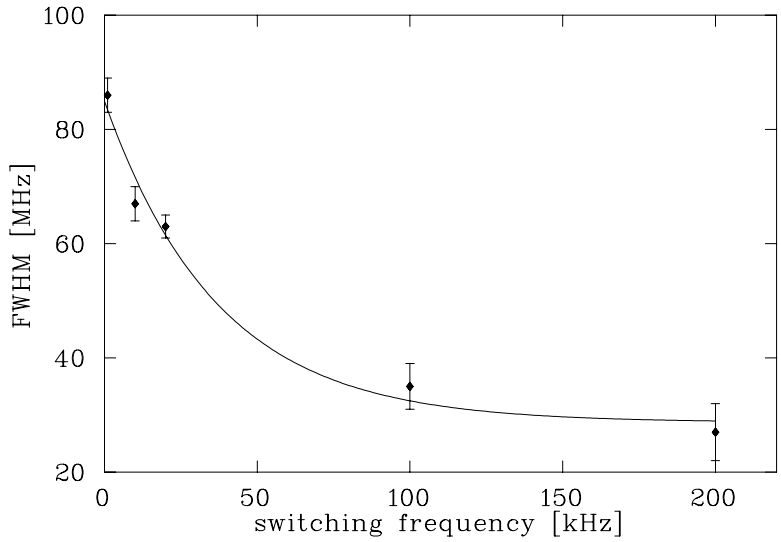

Figure 5.30: *Widths of the Λ-resonance as a function of the switching frequency. This measurement is performed with a coasting beam (without bunching). The width decreases exponentially and approaches a value of about 26 MHz, which is expected from saturation broadening.*

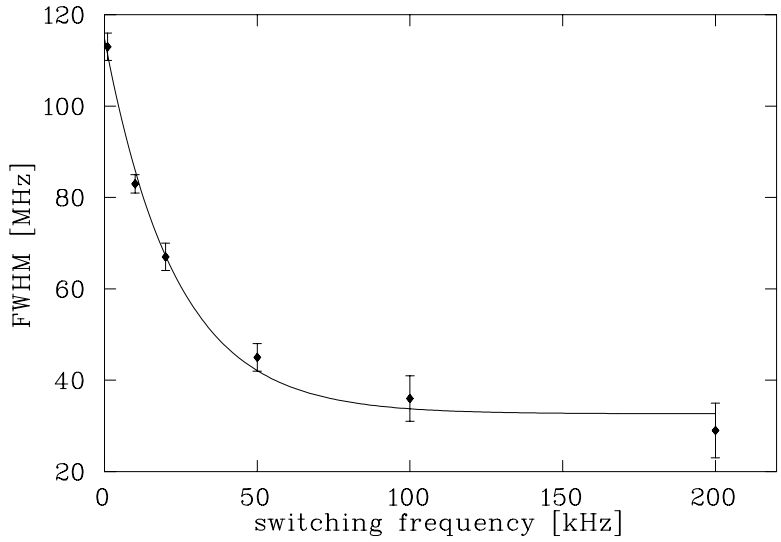

Figure 5.31: *Width of the Λ-resonance as a function of the laser switching frequency for a measurement with a bunched beam. For high switching frequencies the width approaches the same value as for the coasting beam. For low switching frequencies the resonances are broader than in the measurement on the coasting beam. This can be explained by the additional velocity changes caused by the bunching.*

structure splittings $^3S_1$(F=3/2)→ (F=5/2) and $^3P_2$(F=5/2)→ (F=7/2), which where then taken from [Kowalski et al., 1983] (see table 2.3). The result for the two frequencies was

$$\begin{aligned} \nu_{3/2\to5/2} &= 546\,474\,960.66(45)\ \mathrm{MHz} \\ \nu_{5/2\to5/2} &= 546\,455\,142.99(45)\ \mathrm{MHz} \end{aligned}$$

The comparison of the measured Λ-resonance frequency

$$\nu_{\mathrm{Exp}} = 512\,667\,592.4(3.1)\ \mathrm{MHz}$$

with the theoretical value calculated from the frequencies $\nu_{3/2\to5/2}$ and $\nu_{5/2\to5/2}$ assuming Special Relativity

$$\nu_{\mathrm{SR}} = 512\,667\,588.2(0.6)\ \mathrm{MHz}$$

resulted in

$$\delta = 4.3(3.2)\ \mathrm{MHz}.$$

However, the hyperfine transition frequency $^3P_2$(F=5/2)→(F=7/2) measured by [Kowalski et al., 1983] deviated significantly from the theoretical value ([Riis et al., 1994]). A remeasurement of this transition has been done by [Clarke and van Wijngaarden, 2002] recently. Their value lies nearer to the theoretical one (see table 2.3). Using this result we obtain for the two legs of the Λ

$$\begin{aligned} \nu_{3/2\to5/2} &= 546\,474\,962.42(5)\ \mathrm{MHz} \\ \nu_{5/2\to5/2} &= 546\,455\,144.75(5)\ \mathrm{MHz} \end{aligned}$$

and the corresponding SR prediction for the Λ-resonance is

$$\nu_{\mathrm{SR}} = 512\,667\,591.5(0.6)\ \mathrm{MHz}.$$

Comparison with the experimental result yields

$$\delta = 0.9(3.2)\ \mathrm{MHz}.$$

Thus, the discrepancy between theory and experiment is well within 1 σ in this analysis.

Chapter 6

Conclusions and Outlook

6.1 Conclusion

The core of the present work is a test of relativistic time dilation by laser spectroscopy on a fast $^7Li^+$-beam in the Heidelberg heavy ion storage ring TSR. To this end, the systematics of Λ-spectroscopy, which has already been applied in the preceding test experiment at TSR, as well as saturation spectroscopy have been investigated. A detailed measurement using saturation spectroscopy has led to an improved upper limit for deviations from time dilation. The main results of the work are summarized in the following:

- In order to decrease systematic errors in the spectroscopy several measures have been taken concerning the control of the ion beam properties as well as the laser beam profile and the alignment between the lasers and the ion beam.

  The stability and fine-adjustment of the ion velocity has been improved by applying ion beam bunching.

  A new method to control the overlap between the ion beam and the laser beams has been developed using motorized translation stages in order to move the laser beams transversally to the ion beam. By taking the fluorescence of the ions' two-level system resonant with the respective laser by three photomultipliers at different positions along the beam as a function of the transverse displacement the angle between laser and ion beam can be deduced and, if necassary, corrected. The laser-ion beam overlap can be guaranteed to be better than 70 μrad with this method leading to a corresponding uncertainty of only 10 kHz.

  In addition, the laser beam diameters at the three positions are obtained by this method, which allows to determine the parameters of the Gaussian

beam shape of the lasers. This makes the estimate of frequency shifts due to curvature effects possible. For future experiments these frequency shifts can be largely suppressed by properly adjusting the laser beam profiles.

Both laser beams applied on the ion beam have been sent through acousto-optic modulators, which were used to shift the frequency of the respective beams with respect to the beams sent into the iodine spectroscopies accomplishing the frequency calibration. This has been necessary especially for the saturation spectroscopy, since the Lamb dip turned out to lie 66 MHz away from the nearest iodine hyperfine structure line. To obtain a sufficiently accurate frequency calibration, this line was shifted into the vicinity of the Lamb dip. The second purpose of the acousto-optic modulators was to switch the laser beams on and off with frequencies up to 200 kHz by means of rf-switches. This switching allowed to divide a spectroscopic scan into different time windows with both lasers on simultaneously and separately, respectively, and to isolate the Doppler-free spectroscopic feature in both the saturation spectroscopy and the Λ-spectroscopy as described below.

- Chronologically, we started with Λ-spectroscopy, which has already been applied by [Grieser et al., 1994b] for a time dilation test experiment. The large line broadening, that was observed in this experiment limiting the frequency uncertainty, has been identified to be caused by velocity-changing processes of ions during several to many roundtrips in the storage ring. By the laser switching method it was possible to measure, separately, that part of the fluorescence signal, which was caused by the velocity-changes leading to frequency shifts as well as broadening so that it could be subtracted from the total fluorescence signal. In this way, line widths were achieved, that can mainly be explained by saturation broadening. Therefore, this improved Λ-type spectroscopy promises an alternative way for a new time dilation test experiment, which is planned in the near future.

- In the present work, we concentrated on saturation spectroscopy on a two-level system to do a new test of time dilation, as the saturation spectroscopy turned out to be largely insensitive to the velocity-changing processes mentioned above. The usage of the laser-switching method allowed to measure the Doppler-background separately leaving the mere Lamb dip after subtraction. Together with the improvement of systematic errors the Doppler-shifted transition frequency could be determined with an accuracy of 270 kHz. The comparison with the corresponding rest frame frequency taken from literature led to an improved upper limit for deviations from relativistic time dilation as expressed in terms of the Mansouri-Sexl test pa-

rameter α of

$$\alpha < 1.8 \times 10^{-7}. \tag{6.1}$$

6.2 Possible improvements of the saturation spectroscopy

The main problem of the saturation spectroscopy is the intensity-dependent frequency shift of the Lamb dip. As the reason for this shift is unknown, there is a systematic uncertainty in the extrapolation to zero intensity. However, in the present experiment this uncertainty has been estimated to be still smaller than the uncertainty imposed by the insufficient knowledge of the rest frame frequency. Nevertheless, in order to further improve the accuracy, this frequency shift is to be investigated in more detail. In a first step the measurement of the Lamb dip for different laser intensities will be repeated with a considerably higher switching frequency. If the frequency shift is caused by distortions of the resonance due to local changes in the ion velocity distribution caused by laser forces, which affect the ions during one time window, an increased switching frequency and the corresponding decreased duration of one time window should lead to a significant decrease of the shift. Additional recreation periods between the time windows can be inserted, where all lasers are switched off letting the ion velocity distribution approach their electron-cooled and bunched state again.

Since the large laser forces present in saturation spectroscopy are a consequence of the high photon scattering rate due to the Doppler background, the intensity-dependent frequency measurement is to be repeated using Λ-spectroscopy. No frequency shift should occur because the laser forces are significantly smaller in this case.

Another improvement of the Lamb dip spectroscopy can easily be done by performing the spectroscopy far outside the Rayleigh range of the lasers thus suppressing laser profile curvature effects.

6.3 Measurement with slow ions at TSR

In the experiment described in this thesis the Doppler-shifted frequency ν_{a} according to the ${}^3\mathrm{S}_1(F = 5/2) \rightarrow {}^3\mathrm{P}_2(F = 7/2)$ transition is measured at the highest ion velocity possible at TSR ($\beta_{\mathrm{high}} = 0.064$). An upper limit for deviations from the the time dilation factor γ_{SR} given by the theory of Special Relativity was deduced by comparison of ν_{a} with the value $\nu_{\mathrm{a}}^{\mathrm{SR}}$ predicted by Special Relativity from the

rest frame frequency ν_0 and the argon ion laser frequency standard ν_p:

$$\nu_\mathrm{a}^\mathrm{SR} = \frac{\nu_0^2}{\nu_\mathrm{p}} \tag{6.2}$$

with an uncertainty

$$\Delta\nu_\mathrm{a}^\mathrm{SR} = \nu_\mathrm{a}^\mathrm{SR} \sqrt{\frac{(2\Delta\nu_0)^2}{\nu_0^2} + \frac{\Delta\nu_\mathrm{p}^2}{\nu_\mathrm{p}^2}}, \tag{6.3}$$

which is dominated by the uncertainty $\Delta\nu_0 = 400$ kHz of the rest frame frequency contributing to $\Delta\nu_\mathrm{a}^\mathrm{SR}$ twice, because of the appearence of the square of ν_0 in equation 6.2. Since the uncertainty $\Delta\nu_\mathrm{a}^\mathrm{SR}$ significantly exceeds the error of our measurement, the determination of the test parameter α is limited by the insufficient knowledge of the rest frame frequency. However, as an improved measurement of ν_0 using the old slow-beam methods appears to be difficult, we plan to circumvent this problem by replacing ν_0 by a measurement of a Doppler-shifted frequency ν'_a at the lowest ion velocity possible at TSR. As will be discussed below, this experiment promises to be possible with the same accuracy as the measurement at high β. Furthermore, in this scheme, one would obtain a test of time dilation by the comparison of two frequencies measured with the same method. This would remove problems inherent in the determination of the rest frame frequency, which are indicated by the strongly deviating results reported for ν_0.

For the slow ion velocity measurement the resonance condition within the Mansouri-Sexl test theory reads

$$\nu'_\mathrm{a}\nu'_\mathrm{p} = \nu_0^2(1 + 2\alpha\beta_\mathrm{low}^2). \tag{6.4}$$

The primed frequencies denote the Doppler-shifted frequencies for β_low measured in the laboratory reference frame. Together with the same relation for the measurement at high ion velocity β_high

$$\nu_\mathrm{a}\nu_\mathrm{p} = \nu_0^2(1 + 2\alpha\beta_\mathrm{high}^2) \tag{6.5}$$

the rest frame frequency ν_0 can be eliminated:

$$\frac{\nu_\mathrm{a}\nu_\mathrm{p}}{\nu'_\mathrm{a}\nu'_\mathrm{p}} = \frac{1 + 2\alpha\beta_\mathrm{high}^2}{1 + 2\alpha\beta_\mathrm{low}^2} \approx 1 + 2\alpha(\beta_\mathrm{high}^2 - \beta_\mathrm{low}^2). \tag{6.6}$$

Thus, the sensitivity of a comparison of two experiments at different ion velocities is proportional to the difference of the squared velocities.

In a first beamtime we explored the feasibility of an experiment at $\beta_\mathrm{low} = 0.03$, which has been chosen such, that the parallel excitation of the ions can be accomplished by a fixed-frequency frequency-doubled Nd:YAG laser at 532 nm. This

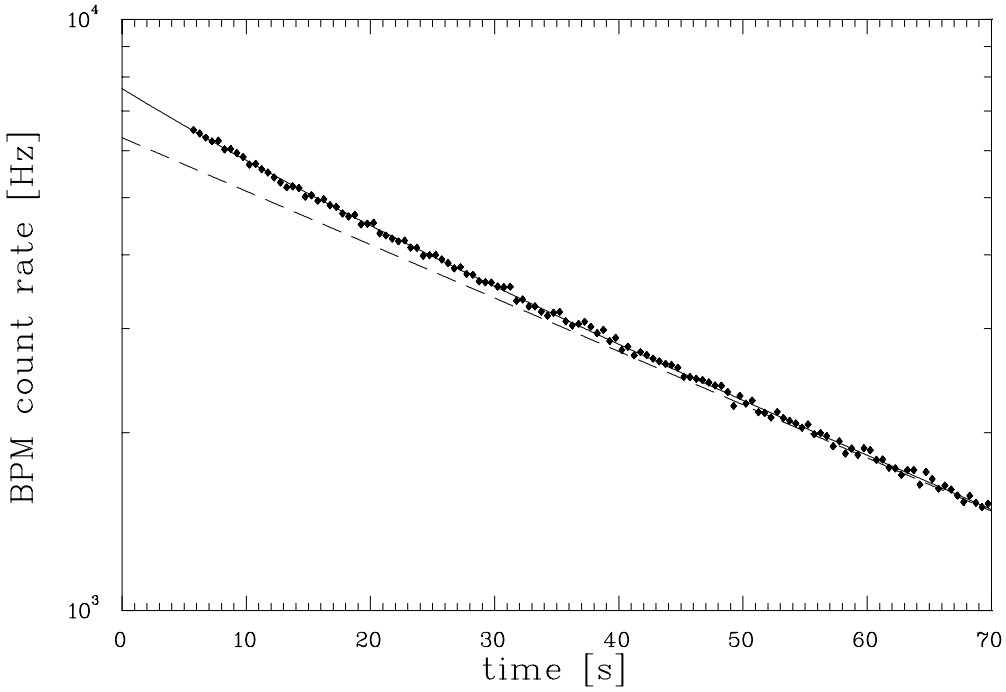

Figure 6.1: *Logarithmic plot of the count rate of ion number versus time for an ion beam stored in TSR at a velocity of $\beta = 0.03$. The decrease can be described by a double-exponential decay, the short-lived component of which are the metastable ions.*

laser can be locked to a calibrated iodine hfs line providing a highly accurate frequency standard as recommended by [CIPM, 1997] (see table 3.1). The antiparallel light again has to be generated by a tunable dye laser at 565 nm, which is well within the gain profile of rhodamine 6G. Nevertheless, no frequency standard is available at this wavelength up to now making an absolute frequency calibration of a suitable iodine line necessary.

Figure 6.1 shows a logarithmic plot of the count rate of the beam profile monitor, which reflects the total ion number, versus time. A double exponential function can well be fitted to the data proving the existence of metastable ions in the ion beam. The fit yields the fraction of metastable ions in the beam as well as the lifetimes of the ground state ions and the metastables to be in the same order of magnitude as in the experiment with $\beta = 0.064$.

In addition, electron cooling proved to be sufficiently fast, so that the ion beam properties allow for the planned experiment.

Since all systematic errors such as angle misalignment or wavefront curvature effects decrease with decreasing ion velocity, an accuracy of the same order of magnitude as in the present experiment or even better can be expected.

From equation 6.6 we have with the definition $\delta\nu = \nu_\mathrm{a} - \nu_\mathrm{a}^\mathrm{SR}$ and $\nu_\mathrm{a}^\mathrm{SR} = \nu'_\mathrm{p}\nu'_\mathrm{a}/\nu_\mathrm{p}$:

$$\alpha = \frac{1}{2\beta_\mathrm{high}^2(1-\frac{\beta_\mathrm{low}^2}{\beta_\mathrm{high}^2})}\frac{\delta\nu}{\nu_\mathrm{a}^\mathrm{SR}}. \tag{6.7}$$

The factor $(1-\beta_\mathrm{low}^2/\beta_\mathrm{high}^2)$, which is 0.78 for the velocities considered here, describes the sensitivity of the experiment to the test parameter α compared to the original experiment using $\beta_\mathrm{high} = 0.064$ and $\beta = 0$. Assuming the frequency uncertainties to be $\Delta\nu_\mathrm{a}^\mathrm{SR} = 200$ kHz for the experiment at β_low and $\Delta\nu_\mathrm{a} = 200$ kHz from that at β_high we expect $\Delta(\delta\nu) = 283$ kHz and for the test parameter

$$\alpha < 8.5 \times 10^{-8}, \tag{6.8}$$

which is about a factor of two better than the present limit. In addition, a more precise determination of ν_0 is possible.

6.4 Measurement at high ion velocity at ESR

The results of the TSR experiment have revealed the storage ring version of the Ives-Stilwell experiment to be a unique method to test the relativistic time dilation. Storage rings equipped with electron coolers provide high speed ion beams of superb quality especially with regard to a high spatial stability, which is necessary to provide the accurate overlap of the ion beam with the lasers, as well as the low transverse temperatures, which are necessary to minimize frequency shifts

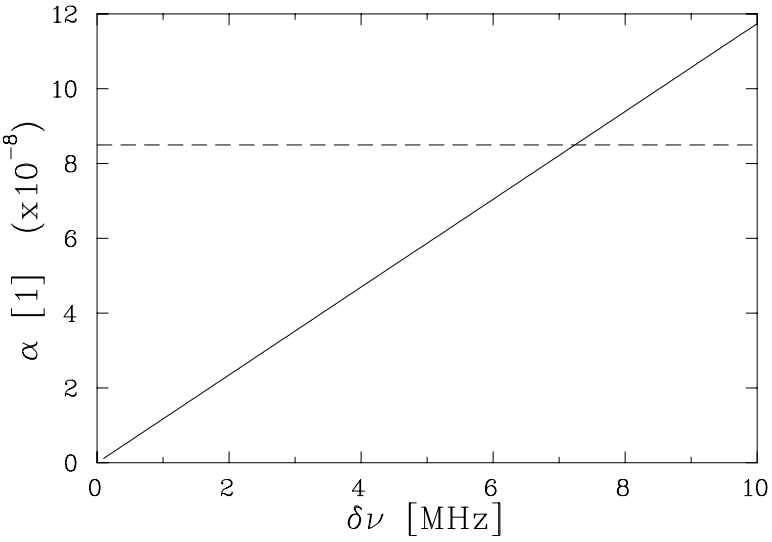

Figure 6.2: *Expected upper limit for the test parameter α for an experiment on $^7Li^+$ at β=1/3 in ESR as a function of the achieved frequency uncertainty in the experiment. The dashed line indicates the expected upper limit from an experiment at low ion velocity at TSR.*

due to dispersion. Another crucial point is the stability and fine control of the longitudinal ion velocity in order to minimize AC-Stark shifts. The stability achieved by electron cooling can be significantly increased by ion beam bunching.

The experiments at TSR will soon be limited by the achievable frequency uncertainties. In order to further constrain the limit for the test parameter α a measurement at higher ion velocities has to be performed. To this end, an experiment at a storage ring with a considerably higher magnetic rigidity must be performed. The Experimental Storage Ring (ESR) at the Gesellschaft für Schwerionenforschung in Darmstadt provides a magnetic rigidity of 10 Tm and, therefore, allows the storage of a $^7\mathrm{Li}^+$ beam at velocities of up to about $\beta = 0.4$.

It has been proposed earlier [Huber et al., 1987][Schmidt, 1994] to use only one frequency standard for both lasers at the frequency $\nu_\mathrm{a}^\mathrm{ESR}$ needed for antiparallel excitation of the resonance. The parallel light is then generated by frequency-doubling one of the lasers leading to the condition

$$\nu_\mathrm{p}^\mathrm{ESR} = 2\nu_\mathrm{a}^\mathrm{ESR}. \tag{6.9}$$

Together with $\nu_\mathrm{p}^\mathrm{ESR}\nu_\mathrm{a}^\mathrm{ESR} = \nu_0^2$ this leads to the frequencies

$$\nu_\mathrm{a}^\mathrm{ESR} = \nu_0/\sqrt{2} = 386.410.463.971 \text{ kHz} \tag{6.10}$$

$$\nu_\mathrm{p}^\mathrm{ESR} = \nu_0 \cdot \sqrt{2} = 722.820.927.941 \text{ kHz}. \tag{6.11}$$

The corresponding wavelengths are $\lambda_{\mathrm{a}} = 775.83$ nm and $\lambda_{\mathrm{p}} = 387.93$ nm. From the Doppler-formula we obtain the required ion velocity

$$\beta = \frac{1 - (\nu_0/\nu_{\mathrm{p}})}{1 + (\nu_0/\nu_{\mathrm{p}})}, \tag{6.12}$$

to be exactly $\beta^{\mathrm{ESR}} = 1/3$.

With the definitions $\delta\nu = \nu_{\mathrm{a}} - \nu_{\mathrm{a}}^{\mathrm{SR}}$ and $\nu_{\mathrm{a}}^{\mathrm{SR}} = \nu_{\mathrm{p}}'\nu_{\mathrm{a}}'/\nu_{\mathrm{p}}^{\mathrm{ESR}}$, where the primed frequencies are from the low beta experiment, we get an estimate for the expected accuracy according to equation 6.7. From a comparison of a possible ESR-experiment at $\beta_{\mathrm{high}} = 1/3$ with the low velocity TSR experiment at $\beta_{\mathrm{low}} = 0.03$ assuming uncertainties of $\Delta\nu_{\mathrm{a}}^{\mathrm{SR}} = 500$ kHz for the frequency $\nu_{\mathrm{a}}^{\mathrm{SR}}$ calculated from the slow-beam experiment at TSR and $\Delta\nu_{\mathrm{a}}^{\mathrm{ESR}} = 1$ MHz we expect

$$\alpha < 1.2 \times 10^{-8}, \tag{6.13}$$

which is an improvement by a factor of 15 compared to the present value. Figure 6.2 shows the upper limit for α, that one would obtain from a given experimental uncertainty in the frequency determination.

Appendix A

Absolute frequencies of the $^{127}I_2$ reference lines

This appendix summarizes all hyperfine structure lines of $^{127}I_2$, which are relevant for this work as reference standards. All lines belong to the $B^3\Pi^+_{Ou} \rightarrow X^1\Sigma^+_g$ electronic transition.

- $P(13)43 - 0$ (a_3-component). This reference line for the argon ion laser at 514.5 nm is recommended as a frequency standard by [CIPM, 1997]. The absolute frequency of the argon ion laser stabilized to this line at a temperature of the iodine cell of $-5 \pm$ °C is

$$\nu_{a_3} = (582\,490\,603\,370 \pm 130)\text{kHz}$$

- $R(99)15 - 1$ (i-component). This transition serves as the reference for the measurement of the Λ-resonance. It has been determined by comparison of the frequency of a dye laser, stabilized to this line at a temperature of the iodine cell of 6°C, with the He-Ne laser, stabilized to the R(127)11-5 transition in $^{127}I_2$ at 15°C, which is recommended as a frequency standard by [CIPM, 1997] using the Michelson interferometer of the Physikalisch-Technische Bundesanstalt (PTB) in Braunschweig [Grieser et al., 1994a]:

$$\nu_i = (512\,667\,622\,777 \pm 67)\text{kHz}.$$

  Furthermore, in the course of this work the separation of the h-component as well as the j-component from the i-component have been determined [Reinhardt, 2003] in order to provide a relative frequency calibration of the dye laser frequency for future Λ-resonance measurements. The result is:

$$\Delta_{j-i} = -23771 \pm 28\ \text{kHz}$$

$$\Delta_{i-h} = 24564 \pm 48\ \text{kHz}.$$

- $R(85)26-0$ (w-component). This reference line for the determination of the rest frame frequency of the $^3S_1(F=5/2) \rightarrow^3 P_2(F'=7/2)$ transition in $^7Li^+$ has also been measured in [Grieser et al., 1994a]. At an iodine cell temperature of $6°C$ one gets

$$\nu_{\mathrm{w}} = (546\ 462\ 926\ 790 \pm 71)\mathrm{kHz}.$$

- $P(10)14-1$ (a-component)

  As the Lamb dip in saturation spectroscopy on the $5/2 \rightarrow 7/2$ transition is about 3.4 GHz apart from the calibrated i-component of the $R(99)15-1$ transition, this line cannot directly be used as the frequency reference. However, another iodine line, the a-component of the $P(10)14-1$ transition lies only 66 MHz apart from the Lamb dip and is therefore chosen for the absolute frequency calibration. Because of the moderate distance between these two iodine lines it was possible to calibrate the a-component by comparison with the calibrated i-component with sufficient accuracy in our laboratory using rf-techniques. To this end, the dye laser beam is split into two by a beamsplitter. One of these beams is frequency-shifted by means of acousto-optic modulators. Both beams are send into an iodine cell and saturation spectroscopy is performed simultaneously. The laser frequency is chosen such that one laser scans across the i-component and the other one across the a-component[1]. From a fit one obtains the residual frequency offset between the two lines. Together with the soundwave frequencies applied to the AOMs, which are known to about 1 kHz, one obtains the offset of the a-component from the i-component. Using the absolute frequency of the i-component, the absolute frequency of the a-component can be derived:

$$\nu_{\mathrm{a}} = (512\ 671\ 028\ 023 \pm 152)\mathrm{kHz}.$$

- $R(56)32-0$ (a_{10}-component)

  According to the Doppler effect, for the planned TSR experiment at low ion velocity the wavelength of the parallel laser light amounts to 532 nm. This light can be provided by a frequency-doubled Nd:YAG laser. The a_{10}-component of the R(56)32-0 ttransition in molecular iodine is reocmmended as a frequency standard [CIPM, 1997]. The frequency for a temperature of the iodine cell between -10 °C and -20 °C is

$$\nu_{\mathrm{a_{10}}} = (563\ 260\ 223\ 480 \pm 40)\mathrm{kHz}.$$

[1] Actually the measurement had to be performed in two steps, because our frequency shifters only allow for shifts of up to 1800 MHz. Therefore, the i-component as well as the a-component are compared to an intermediate iodine line somewhere in between.

Transition	Frequency offset from a_{10}-component [kHz]
R(57)32-0, a_1	-50 946 880.4
P(54)32-0, a_1	-47 588 892.5
P(119)35-0, a_1	-36 840 161.5
R(86)33-0, a_1	-32 190 404.0
R(106)34-0, a_1	-30 434 761.5
R(134)36-0, a_1	-17 173 680.4
P(83)33-0, a_{21}	-15 682 074.1
R(56)32-0, a_{10}	0
P(53)32-0, a_1	+ 2 599 708.0

Table A.1: *Optical frequency standards for the frequency-doubled Nd:YAG laser at 532 nm as recommended by the CIPM [CIPM, 1997].*

However, for the antiparallel light with wavelength 565 nm there is no calibrated iodine line available, yet. A suitable line still has to be chosen. As in this wavelength region gaps of typically 5 GHz between fine structure lines can occur, the choice of the ion velocity to reach a suitable iodine line can lead to a deviation of the laser frequency required for the parallel light from the iodine line given above. Fortunately, in [CIPM, 1997] there are several different hyperfine structure lines recommended, lying in the vicinity of the a_{10}-component. Their frequencies are given relative to the absolute frequency of the a_{10}-component. Table A.1 comprises these lines.

Bibliography

[Albrecht et al., 1996] Albrecht, F., Beutelspacher, M., Grieser, M., von Hahn, R., Knoll, L., Repnow, R., Schwalm, D., Tetzlaff, K., and Wester, R. (1996). Slow Extraction at the Heidelberg Heavy Ion Storage Ring TSR. *5$^{\text{th}}$ Eur. Part. Acc. Conf.* **3**, 2459.

[Bayer-Helms and Helmcke, 1977] Bayer-Helms, F. and Helmcke, J. (1977). Modulation Broadening of Spectral Profiles. *PTB Report*.

[Beutelspacher, 2000] Beutelspacher, M. (2000). *Systematische Untersuchungen zur Elektronenkühlung am Heidelberger Schwerionenspeicherring TSR*. Dissertation Universität Heidelberg.

[Bjorkholm and Liao, 1975] Bjorkholm, J. E. and Liao, P. F. (1975). Optically induced atomic energy level shifts and two-photon spectroscopy. In: Haroche, S., Pebay-Peyroula, J. C., Hänsch, T. W., and Harris, S. E. (Eds.), *Laser Spectroscopy* , pp. 176–185. Second International Conference on Laser Spectroscopy.

[Boussard, 1985] Boussard, D. (1985). In: *Advanced Accelerator Physics*. CERN Accelerator School.

[Budker, 1967] Budker, G. I. (1967). *Atomnaya Energiya* **22**, 346.

[Budker et al., 1976] Budker, G. I., Dikansky, N., Kudelainen, V. I., Meshkov, I., Parchomchuk, V. V., Pestrikov, D., Skrinsky, A. N., and Sukhina, B. N. (1976). Experimental studies of electron cooling. *Part. Accel.* **7**.

[Champeney et al., 1963] Champeney, D. C., Isaac, G. R., and Kahn, A. M. (1963). An 'Aether Drift' Experiment Based on the Mössbauer Effect. *Phys. Lett.* **7**, 241.

[CIPM, 1997] CIPM, E. n. (1997). Documents concerning the new definition of the metre. *Metrologia* **30**, 523.

[Clarke and van Wijngaarden, 2002] Clarke, J. J. and van Wijngaarden, W. A. (2002). Precision Hyperfine and Fine Structure Measurements of $^{6,7}Li^{+}$ 1s2s ^{3}S and 1s2p ^{3}P States. *to be published*.

[Demtröder, 1998] Demtröder, W. (1998). *Laser Spectroscopy, Basic concepts and instrumentation*. Springer.

[Einstein, 1905] Einstein, A. (1905). Zur Elektrodynamik bewegter Körper. *Ann. D. Phys.* **17**, 891.

[Eisenbarth, 2001] Eisenbarth, U. (2001). *Laser Cooling of fast stored ion beams to extreme phase-space densities*. Dissertation Universität Heidelberg.

[Eisenbarth, 2002] Eisenbarth, U. (2002). *to be published*.

[Gerstenkorn and Luc, 1978] Gerstenkorn, S. and Luc, P. (1978). Ed. du Centre National de la Recherche Scientifique.

[Goncharov et al., 1991] Goncharov, A. N., Gateva-Kosteva, S. V., Skvortsov, M. N., and Chebotayev, V. P. (1991). Direct Observation of the Anomalous Zeeman Effect at the $X \rightarrow B$ Transition of Molecular Iodine by the Method of Nonlinear Laser Spectroscopy. *Appl. Phys. B* **52**, 311.

[Goncharov et al., 1996] Goncharov, A. N., Nevsky, A. Y., and Skvortsov, M. N. (1996). Second-order Zeeman effect of the $X \rightarrow B$ transition in molecular iodine. *Appl. Phys. B* **62**, 427.

[Grieser, 1994] Grieser, R. (1994). *Test der lokalen Lorentz-Invarianz am Heidelberger Testspeicherring*. Dissertation Universität Mainz.

[Grieser et al., 1994a] Grieser, R., Bönsch, G., Dickopf, S., Huber, G., Klein, R., Merz, P., Nicolaus, A., and Schnatz, H. (1994a). Precision measurement of two iodine lines at 585 nm and 549 nm. *Z. f. Phys. A* **348**, 147.

[Grieser et al., 1994b] Grieser, R., Klein, R., Huber, G., Dickopf, S., Klaft, I., Knobloch, P., Merz, P., Albrecht, F., Grieser, M., Habs, D., Schwalm, D., and Kühl, T. (1994b). A test of special relativity with stored lithium ions. *Appl. Phys. B* **59**, 127.

[Grosser, 1983] Grosser, J. (1983). *Einführung in die Teilchenoptik*. Teubner.

[Hangst et al., 1991] Hangst, J., Kristensen, M., Nielsen, J., Poulsen, O., Schiffer, O., and Shi, P. (1991). Laser Cooling of a fast Stored Ion Beam to 1 mK. *Phys. Rev. Lett.* **67**, 1238.

[Hochadel, 1994] Hochadel, B. (1994). Residual-gas ionization beam profile monitor for the Heidelberg test storage ring TSR. *Nucl. Inst. Meth. A* **343**, 401.

[Huber et al., 1987] Huber, G., Schmidt, N., Schröder, S., Wendt, K., Dutta, M., Kühl, T., Marx, D., and Orth, H. (1987). Proposal no. 111 for an experiment at the ESR: Laser Spectroscopy with stored relativistic $^7Li^+$ ions. Proposal no. 111 GSI Darmstadt.

[Isaak, 1970] Isaak, G. R. (1970). *Phys. Bull.* **21**, 255.

[Ives and Stilwell, 1938] Ives, H. E. and Stilwell, G. R. (1938). An Experimental Study of the Rate of a Moving Atomic Clock. *J. Opt. Soc. Am.* **7**, 215.

[Kaivola et al., 1985] Kaivola, M., Poulsen, O., and Riis, E. (1985). Measurement of the relativistic Doppler Shift in Neon. *Phys. Rev. Lett.* **54**, 255.

[Kennedy and Thorndike, 1932] Kennedy, R. J. and Thorndike, E. M. (1932). Experimental Establishment of the Relativity of Time. *Phys. Rev.* **42**, 400.

[Klaft et al., 1994] Klaft, I., Borneis, S., Engel, T., Fricke, B., Grieser, R., Huber, G., Khl, T., Marx, D., Neumann, R., Schrder, S., Seelig, P., and Vlker, L. (1994). Precision Laser Spectroscopy of the Ground State Hyperfine Structure Splittin of Hydrogenlike $^{209}Bi^{82+}$. *Phys. Rev. Lett.* **73**, 2425.

[Klein, 1991] Klein, R. M. (1991). *Präzisionsspektroskopie an gekühlten Li^+ Ionen im Schwerionenspeicherring als experimenteller Test der speziellen Relativitätstheorie*. Dissertation Universität Mainz.

[Kowalski et al., 1983] Kowalski, J., Neumann, R., Noethe, S., Suhr, H., zu Putlitz, G., and Herman, R. (1983). Triplet-Singlet Interaction in the $1s2s^3S_1$ Hyperfine Splitting of He-Like Li^+. *Z. Phys. A* **313**, 147.

[Kretzschmar, 1992] Kretzschmar, M. (1992). Doppler spectroscopy on relativistic particle beams in the light of a test theory of special relativity. *Z. Phys. A* **342**, 463.

[Kuhn, 1962] Kuhn, T. S. (1962). *The Structure of Scientific Revolutions*. University of Chicago Press.

[Lauer et al., 1998] Lauer, I., Eisenbarth, U., Grieser, M., Grimm, R., Lenisa, P., Luger, V., Schätz, T., Schramm, U., Schwalm, D., and Weidemüller, M. (1998). Transverse laser cooling of a fast stored ion beam through dispersive cooling. *Phys. Rev. Lett.* **81**, 2052.

[MacArthur, 1986] MacArthur, D. W. (1986). Special relativity: Understanding experiomental tests and formulations. *Phys. Rev. A* **33**, 1.

[MacArthur et al., 1986] MacArthur, D. W., Butterfield, K. B., Clark, D. A., Donahue, J. B., and Gram, P. A. M. (1986). Test of the Special-Relativistic Doppler Formula at $\beta = 0.84$. *Phys. Rev. Lett.* **56**, 282.

[Mansouri and Sexl, 1977] Mansouri, R. and Sexl, R. U. (1977). A Test Theory of Special Relativity: I.-III. *Gen. Rel. Grav.* **8**, 497,515,809.

[Merz, 1991] Merz, P. (1991). Frequenzstabilisierung eines Argonionenlasers auf $^{127}I_2$ Hyperfeinstrukturlinien. *Diploma-Thesis, Universität Mainz.*

[Michelson and Morley, 1887] Michelson, A. A. and Morley, E. H. (1887). On the Relative Motion of the Earth and the Luminiferous Ether. *A. J. Sci.* **34**, 333.

[Miesner et al., 1996] Miesner, H.-J., Grimm, R., Habs, D., Schwalm, D., Wanner, B., and Wolf, A. (1996). Efficient, Indirect Transverse Laser Cooling of a fast Ion Beam. *Phys. Rev. Lett.* **77**, 623.

[Penzias and Wilson, 1965] Penzias, A. A. and Wilson, R. H. (1965). *Astrophys. J.* **142**, 419.

[Reinhardt, 2003] Reinhardt, S. (2003). Dipoma thesis, in preparation.

[Riis et al., 1988] Riis, E., Anderson, L.-U. A., Bjerre, N., and Poulsen, O. (1988). Test of the Isotropy of the Speed of Light Using Fast-Beam Laser Spectroscopy. *Phys. Rev. Lett.* **60**, 81.

[Riis et al., 1994] Riis, E., Sinclair, A. G., Poulsen, O., Drake, G. W. F., Rowley, W. R. C., and Levick, A. P. (1994). Lamb shifts and hyperfine structure in $^6Li^+$ and $^7Li^+$: Theory and experiment. *Physical Review A* **49**, 207.

[Rindler, 1977] Rindler, W. (1977). *Essential Relativity*. Springer.

[Robertson, 1949] Robertson, H. P. (1949). Postulate versus Observation in the Special Theory of Relativity. *Rev. Mod. Phys.* **21**, 378.

[Rong et al., 1998] Rong, H., Grafström, S., Kowalski, J., Neumann, R., and zu Putlitz, G. (1998). A new precise value of the absolute 2^3S_1, F=5/2-2^3P_2, F=7/2 transition frequency in $^7Li^+$. *Eur. Phys. J. D* **3**, 217.

[Rong et al., 1993] Rong, H., Grafström, S., Kowalski, J., zu Putlitz, G., Jastrzebski, W., and Neumann, R. (1993). Heterodyne laser spectroscopy of lithium ions: 2^3P fine and hyperfine structure of $^7Li^+$. *Z. Phys D* **25**, 337.

[Rostohar et al., 2001] Rostohar, D., Derkatch, A., Hartman, H., Johansson, S., Lundberg, H., Mannervik, S., Norlin, L.-O., Royen, P., and Schmitt, A. (2001). Lifetime measurements of metastable states in Fe^+. *Phys. Rev. Let.* **86**, 1466.

[Saghiri, 1999] Saghiri, A. A. (1999). *Hochauflösende Messung zur dielektronischen Rekombination von metastabilen und Grundzustands-Li^+-Ionen*. Dissertation Universität Heidelberg.

[Schmidt, 1994] Schmidt, M. (1994). Aufbau eines Diodenlaserspektrometers für Testexperimente zur speziellen Relativitätstheorie. *Diploma-Thesis, Universität Mainz*.

[Schmitt, 1999] Schmitt, M. (1999). *Erzeugung energiescharfer Elektronenstrahlen*. Dissertation Universität Heidelberg.

[Schröder et al., 1990] Schröder, S., Klein, R., Boos, N., Gerhard, M., Grieser, R., Huber, G., Karafillidis, A., Krieg, M., Schmidt, N., Kühl, T., Neumann, R., Balykin, V., Grieser, M., Habs, D., Jaeschke, E., Krämer, D., Kristensen, M., Music, M., Petrich, W., Schwalm, D., Sigray, P., Steck, M., Wanner, B., and Wolf, A. (1990). First Laser Cooling of Relativistic Ions in a Storage Ring. *Phys. Rev. Lett.* **64**, 2901.

[Seelig et al., 1998] Seelig, P., Borneis, S., Dax, A., Engel, T., Faber, S., Gerlach, M., Holbrow, C., Huber, G., Khl, T., Marx, D., Meier, K., Merz, P., Quint, W., Schmitt, F., Tomaselli, M., Vlker, L., Winter, H., Wrtz, M., Beckert, K., Franzke, B., Nolden, F., Reich, H., Steck, M., , and Winkler, T. (1998). Ground State Hyperfine Splitting of Hydrogenlike $^{207}Pb^{81+}$ by Laser Excitation of a Bunched Ion Beam in the GSI Experimental Storage Ring. *Phys. Rev. Lett.* **81**, 4824.

[Siegman, 1986] Siegman, A. E. (1986). *Lasers*. University Science Books.

[Sörensen, 1987] Sörensen, A. H. (1987). Introduction to Intrabeam Scattering. In: Turner, S. (Ed.), *CERN Accelerator School*.

[Spieweck, 1980] Spieweck, F. (1980). *IEEE Trans. Intrum. Meas.* **4**, 361.

[Träbert, 2000] Träbert, E. (2000). Atomic lifetime measurements with ion traps of many sizes. *Physica Scripta* **61**, 257.

[Vessot et al., 1980] Vessot, R. F. C., Levine, M. W., Mattison, E. M., Blomberg, E. L., Hoffmann, T. E., Nystrom, G. U., Farrel, B. F., Decher, R., Eby, P. B., Baugher, C. R., Watts, J. W., Teuber, D. L., and Wills, F. D. (1980). *Phys. Rev. Lett.* **45**, 2081.

[Wanner et al., 1998] Wanner, B., Grimm, R., Gruber, A., Habs, D., Miesner, H.-J., Nielsen, J. S., and Schwalm, D. (1998). Rapid adiabatic passage in laser cooling of fast stored ion beams. *Phys. Rev. A* **58**, 2242.

[Will, 1986] Will, C. (1986). In: *Accuracy of Time Transfer in Satelliete Systems*.

[Will, 1992] Will, C. M. (1992). Clock sychronization and isotropy of the one-way speed of light. *Phys. Rev. D* **45**, 403.

[Wille, 1996] Wille, K. (1996). *Physik der Teilchenbeschleuniger und Synchrotronstrahlungsquellen. Eine Einfhrung.* Teubner.

[Yariv and Yeh, 1983] Yariv, A. and Yeh, P. (1983). *Optical Waves in Crystals : Propagation and Control of Laser Radiation*. John Wiley & Sons.

Danksagung

Das Zustandekommen der vorliegenden Arbeit baut auf einer breiten Unterstützung durch viele Personen sowie auf einer sehr angenehmen Arbeitsatmoshäre auf, wofür ich mich an dieser Stelle sehr herzlich bedanken möchte.

Zunächst möchte ich mich bei Herrn Prof. Dr. Dirk Schwalm und Herrn Prof. Dr. Andreas Wolf für die Möglichkeit, in ihrer Arbeitsgruppe an einem so interessanten Thema arbeiten zu dürfen sowie für die Betreuung bedanken. Das Gelingen der Arbeit ist vor allem ihrer Geduld und langanhaltenden Unterstützung zu verdanken. Ich schätze besonders den großen Freiraum, mit dem ich während der letzten Jahre arbeiten konnte.

Mein ganz besonderer Dank aber gilt Herrn Dr. Gerald Gwinner für seine exzellente Betreuung. Sein breites Wissen, seine Erfahrung und seine Kreativität in experimentellen Methoden wie in allgemeinen physikalischen Fragen haben nicht nur den Fortschritt des Experiments wesentlich bestimmt. Auch habe ich bei der gemeinsamen Arbeit ungeheuer viel gelernt.

Herrn Prof. Dr. H.-Jürgen Kluge danke ich für die Übernahme des Zweitgutachtens.

Das Experiment wurde in Zusammenarbeit mit der Arbeitsgruppe von Herrn Prof. Dr. Gerhard Huber vom Institut für Physik der Universität Mainz durchgeführt. Hier haben wir von den Erfahrungen Prof. Hubers aus früheren Experimenten an $^7Li^+$ und seiner Erfahrung in Laserspektroskopie im allgemeinen ganz wesentlich profitiert. Mein ganz besonderer Dank gebührt Herrn Dr. Sergej Karpuk, der an dem Experiment ganz wesentlich beteiligt ist. Sein großes experimentelles Geschick insbesondere im Umgang mit Lasern und sein unermüdlicher Einsatz bei den vielen, teilweise leicht nervenaufreibenden Strahlzeiten und deren Vorbereitung, waren eine unabdingbare Voraussetzung für das Vorankommen des Experiment. Herr Dr. Karpuk war von Anfang an dem Experiment beteiligt und erlangte sehr schnell einen teifen Einblick in alle das Experiment betreffenden Gebiete. Dadurch wurde er zu einem unverzichtbaren Mitglied der “Kernmannschaft”, der das Vorankommen des Experiments entscheidend mitbestimmt hat. Dafür bin ich ihm zu großem Dank verpflichtet.

Die verbesserte Messung der Zeitdilatation basiert auf der Frequenzkalib-

rierung einer Hyperfeinstruktur-Linie im molekularen Iod, die als Frequenzstandard verwendet wurde. Diese wurde von Herrn cand. phys. Sascha Reinhardt in seiner Diplomarbeit, die in Kürze beendet sein wird, mit großer Kompetenz und Sorgfalt durchgeführt. Dafür sowie für seine Mitarbeit bei Strahlzeiten bedanke ich mich sehr herzlich.

Die Durchführung der Strahlzeiten wäre nicht möglich gewesen ohne die tatkräftige Unterstützung durch Mitarbeiter in der Heidelberger Arbeitsgruppe. Hier sind in erster Linie Dr. Udo Eisenbarth und Dr. Sven Krohn zu nennen, die immer bereit waren zu helfen und ihre Erfahrungen insbesondere den Speicherring betreffend einzubringen. Hierfür möchte ich mich bei ihnen recht herzlich bedanken. Ebenfalls bedanken möchte ich mich bei Frau MSc Raquel Muñoz-Horta für ihre Hilfe bei einigen Strahlzeiten, deren Vorbereitung und Auswertung. Desweiteren bedanke ich mich bei Dipl.-Phys. Sandro Hannemann, Dipl.-Phys. Ines Hoog, Dr. Peter Merz und Dr. Jens Lassen, die in Engpässen bei Strahlzeiten mitgeholfen haben.

Die hohe Verläßlichkeit des Speicherringbetriebs, die für unsere Messungen sehr wichtig waren, wurden durch Dr. Manfred Grieser und Herrn Kurt Horn sichergestellt. Hierfür und für die schnelle Hilfe bei Problemen möchte ich mich herzlich bedanken.

Bedanken möchte ich mich auch bei Frau Helga Krieger, die immer mit Rat und Tat zur Verfügung stand und mich besonders bei der “Zähmung” des Farbstofflasers unterstützt hat.

Zum Schluß gilt mein besonderer Dank meinen Eltern, die mir das Physik-Studium ermöglicht haben und mich immer nach Kräften unterstützt haben.